A SEARCH FOR NON-$q\bar{q}$ MESONS IN CENTRAL PRODUCTION

Andrew Kirk

Thesis submitted for the degree
of Doctor of Philosophy.

School of Physics and
Space Research,
Faculty of Science and Engineering,
The University of Birmingham.

September 1989

Synopsis

This thesis presents a search for non-$q\bar{q}$ mesons produced in the central region in the reaction $pp \rightarrow p_f (X^0) p_s$ at 300 GeV/c, where the subscripts f and s indicate the fastest and slowest particles in the laboratory respectively and X^0 represents the central system that is presumed to be produced by double exchange processes. Results are presented of an analysis of the decay of X^0 to $K^0_S K^{\pm}\pi^{\mp}$, $K^+K^-K^+K^-$ and $\pi^+\pi^-\pi^+\pi^-$.

In the $K^0_S K^{\pm}\pi^{\mp}$ channel clear $f_1(1285)$ and $f_1(1420)$ signals are seen. A spin parity analysis shows that both are consistent with being 1^{++} states. The $f_1(1420)$ is found to decay only to $K^*\bar{K}$ and no 0^{-+} wave is required to describe the data. The production of the $f_1(1285)$ as a function of energy is not the same as that for the $f_1(1420)$ whose cross section is found to be constant with energy.

In the $K^+K^-K^+K^-$ channel $\phi\phi$ production has been observed and the ratio $\sigma(\phi K^+K^-)/\sigma(\phi\phi)$ is 1.0 ± 0.3. The cross-section for central production of $\phi\phi$ is found to be the same at 300 GeV/c and 85 GeV/c. An angular analysis of the $\phi\phi$ system favours $J^P = 2^+$ over 0^-.

The $\pi^+\pi^-\pi^+\pi^-$ mass spectrum shows evidence for the $f_1(1285)$ with a mass of 1281 ± 1 MeV and a width of 31 ± 5 MeV. In addition there is evidence for two new enhancements at masses of 1449 ± 4 and 1901 ± 13 MeV with widths of 78 ± 18 and 312 ± 61 MeV respectively. An analysis of the state at 1.45 GeV indicates that it is not a $\pi^+\pi^-\pi^+\pi^-$ decay mode of the $f_1(1420)$ or $\iota/\eta(1440)$.

Acknowledgements

I would like to thank the SERC and the Department of Physics for the financial support that I have received during my time at Birmingham University. I am indebted to Professor Derek Colley for allowing me to work in the High Energy Physics group and to Dr John Kinson for allowing me to be a member of the Omega group and more especially for all his help and support. I would also like to thank my supervisor Dr Ian Bloodworth for his advice and friendliness during my studies.

Many people have had an influence on the work presented in this thesis. In particular I would like to thank Professor Antimo Palano without whose help and incredible enthusiasm this thesis would not have been possible. I am very grateful to Drs Orlando Villalobos Baillie, Bernard French and Emanuele Quercigh for the tremendous amount of support and advice they gave me with my analysis.

I would also like to thank the Omega Collaboration, especially Drs Noel Carney and Frank Votruba, for putting up with me for the last three years and making my time in WA76 so pleasurable.

On the social scene I would like to thank all of those people who I have known in particular Nav Bains, Dave Charlton, Mark Dinsdale, Dave Evans, Jonathan Gregory, Andy Halley, Steve Haywood, Steve Hillier, Roger Jones, Rob Krawiec, Ian Print, Dave Rees, Tim Smith, Mary Trainor, Kev Varvell, and Nigel Watson. I would also like to thank my friends in Birmingham Cath Hipwood, Adam Kowalski, Rob Rowlingson and Sarah and Keith Wallis who tried their hardest to keep me sane. Finally I would like to thank my mother and my brothers and sisters Chris, John, Ron and Sue for all the support and help they have given me.

To you all

Thank you

To

Kathleen and John William Kirk

my mother and father

CONTENTS

TABLES

FIGURES

1. AN INTRODUCTION TO GLUONIC STATES

1.1 Introduction

In the early 1960's Gell-Mann [1] and Zweig [2] proposed that the particles that undergo the strong interaction, called hadrons, like the proton, neutron or π meson could be regarded as composites of more basic spin $1/2\hbar$ objects called "quarks". At that time these quarks were regarded as little more than a convenient mathematical device with which to model the properties of hadrons. However, when experiments designed to probe the structure of the proton began at Stanford in the late 1960's it was revealed that protons do indeed contain point-like constituent quarks.

It was proposed that just two types of quark combinations were required to account for the observed hadrons,

$$\text{baryons} = qqq \quad \text{and}$$

$$\text{mesons} = q\bar{q}.$$

This description was found to be very successful in grouping the particles into multiplets of a given spin-parity.

In analogy to Quantum ElectroDynamics (QED), which is the theory describing the electromagnetic interaction between two charged particles by the exchange of a spin 1 virtual photon, the strong interaction that binds the quarks into hadrons is mediated by the exchange of a spin 1 particle called a gluon. In order to describe this interaction a strong "colour" charge has to be introduced, analogous to electric charge, which is carried by both the quarks and gluons. The experimental evidence for gluons comes from experiments on deep inelastic scattering and jet studies [3].

The main difference between Quantum Chromodynamics (QCD), the quantum field theory of strong interactions, and QED is that the quanta of QCD, the gluons, carry the charge of the field and therefore can self-interact. A field of this type, in which the quanta themselves act as a source of the field is said to be non-Abelian. QED, on the other hand, involves uncharged photons and is Abelian.

In the last few years, one of the basic motivations of experimental high energy physics has been the testing of the predictions of QCD. This non-Abelian field theory not only describes how quarks and antiquarks interact, but also predicts that the gluons which are the quanta of the field will themselves interact to form mesons. If the object formed is composed entirely of valence gluons the meson is called a glueball, however if it is composed of a mixture of valence quarks, antiquarks and gluons (i.e. $q\bar{q}g$) it is called a hybrid. These states are said to have a gluonic degree of freedom and QCD predicts that the observed hadrons are not just those states which consist of three quarks or a quark and antiquark but there also exists a set of states that contain one or more valence gluons.

The search for these states has been carried out by studying several production mechanisms such as prompt production at high P_T [4], J/ψ radiative and hadronic decays [5] [6], $p\bar{p}$ annihilations and central production [7] [8] [9].

This thesis describes results from experiment WA76 which is designed to study exclusive final states formed in the reaction

$$pp \rightarrow p_f (X^0) p_s$$

where the subscripts f and s indicate the fastest and slowest particles in the laboratory respectively and X^0 represents the central system that is presumed to be produced by double exchange processes. At high centre-of-mass energies these double exchange processes are believed to be dominated by Double Pomeron Exchange (DPE), where the Pomeron is thought to have a large gluonic content, leading to the conclusion that Pomeron-Pomeron scattering could be a source of gluonic states.

The characteristics of DPE will be described in chapter 4. The remainder of this chapter will discuss the characteristics of gluonic states, possible ways of distinguishing a gluonic state from a quarkonium state and the methods that have been used to try to isolate gluonic states.

1.2 Allowed angular momentum states of glueballs

Initially there was considerable confusion over which glueball states were allowed. However, since about 1985 a consensus of opinion has been reached amongst theorists as to what are the allowed angular momentum states of glueballs. The main dispute was whether or not the valence gluons which form a glueball are massless or not. If the gluons are massless then there are only two helicity states possible (see appendix A), and hence certain spin-parities are not allowed for glueballs made of two massless gluons which are allowed for a glueball made of two massive gluons.

It is commonly accepted that the up and down flavours of quarks are approximately massless and yet act as if they carry a mass of 350 MeV/c^2, the so called constituent mass. This gives rise to meson ground states of typically 700 MeV/c^2 from quark and antiquark or 1 GeV/c^2 groundstates of three quarks. This constituent mass can be regarded as an energy of confinement as in the bag model, or as the effect of the quark being surrounded by a cloud of virtual quarks, antiquarks and gluons [10]. Analogous considerations can be made for gluons. The gluon mass is indeed exactly zero, as this is required by local gauge invariance (see appendix A), but when the gluons are confined inside a small region of space they gain a constituent mass analogous to that arising for quarks. Therefore although gluons inside a glueball have a constituent mass, the gluons that couple together to produce the glueball must be considered to be massless.

There is very little written about the formulation of the selection rules for these states. Therefore appendix B contains an experimentalist's attempt to derive the glueball states that have now become accepted as standard. The method consists of using Bose symmetry and gauge invariance and predicts that the lowest lying allowed states for the two gluon system are those shown in table 1.

A similar procedure can be used for three gluon states and the allowed states are shown in table 2. It should be noted that with three gluons both $C = +$ and $C = -$ states can be formed [11].

Table 1: Allowed angular momentum states for two gluons

Modes	J^{PC}
$(TE)^2$	$0^{++}, 2^{++}$
$(TE)(TM)$	$0^{-+}, 2^{-+}$
$(TM)^2$	$0^{++}, 2^{++}$

Table 2: Allowed angular momentum states for three gluons

Mode	J^{PC}
$(TE)^3$	$0^{++}, 1^{+-}, 3^{+-}$
$(TE)^2(TM)$, $(TE)(TM)^2$	$0^{-+}, 1^{-+}, 2^{-+}, 3^{-+}$
$(TM)^3$	$1^{--}, 2^{--}, 3^{--}$

Table 3: Allowed angular momenta for ground state hybrids

Mode	J^{PC}
$q\bar{q}g_{TE}$	$1^{--}, 0^{-+}, 1^{-+}, 2^{-+}$
$q\bar{q}g_{TM}$	$1^{+-}, 0^{++}, 1^{++}, 2^{++}$

1.3 Allowed angular momentum states of hybrids

In hybrid states, the colour octet component of the quark-antiquark pair is neutralised by a constituent gluon. As is discussed in appendix B, in the bag model the valence gluons can either be transverse electric (TE, $J^P = 1^+$) or transverse magnetic (TM, $J^P = 1^-$). The ground state hybrids are formed as follows (as shown in table 3),

$$|q\bar{q}g_{TE}> : \quad 0^{-+} \times g_{TE} = 1^{--}$$
$$1^{--} \times g_{TE} = 0^{-+}, 1^{-+}, 2^{-+}$$

$$|q\bar{q}g_{TM}> : \quad 0^{-+} \times g_{TM} = 1^{+-}$$
$$1^{--} \times g_{TM} = 0^{++}, 1^{++}, 2^{++}$$

where $g_{TE}(g_{TM})$ is a Transverse Electric (Transverse Magnetic) gluon and the J^{PC} values give the spin configuration of the $q\bar{q}$ pair.

1.4 Mass calculations

Several calculations have been made based on the bag model [12] in an attempt to calculate the glueball mass spectrum but the agreement between the different predictions is only fair. However most of the models converge in assigning quite low masses to these new states some of which should have masses in the 0.5 to 2.0 GeV/c^2 region. A summary of the predictions are shown in fig. 1 [13]. However, more recently predictions have been made using lattice gauge theory [14] and flux tube models [15] which indicate that the lowest states could be higher in mass.

The masses of the lowest lying two gluon glueballs have been calculated using lattice gauge theory. Recent predictions [16] show that

$$m(2^{++})/m(0^{++}) = 1.5$$

and using a string constant of $\sqrt{k}$ = 400 MeV that

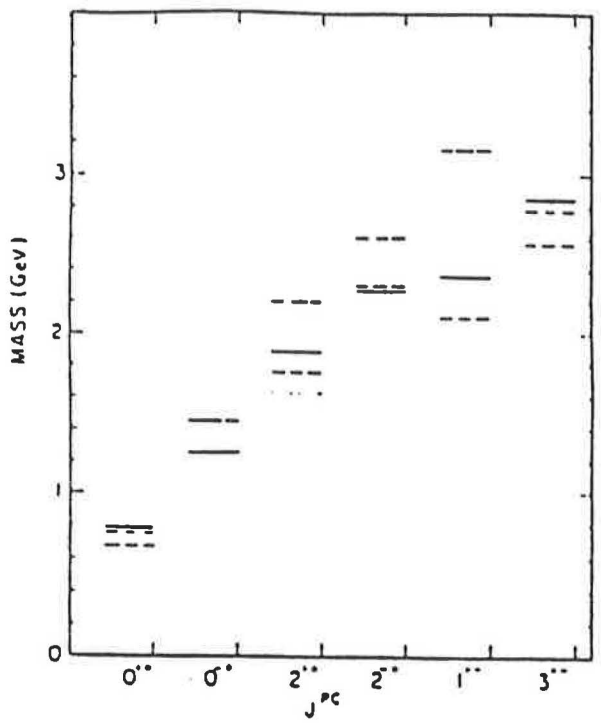

Figure 1: Prediction, for each J^{PC}, for the low lying glueball masses coming from four different models.

$$m(0^{++}) = (1240-1600)\ \mathrm{MeV/c^2}.$$

The flux tube model has been used to calculate the masses of the lowest lying hybrid states and recent predictions [17] are that

$$m(1^{--},0^{-+},1^{-+},2^{-+}) \approx 1900\ \mathrm{MeV/c^2}.$$

1.5 Characteristics of gluonic states

Mesons composed of quarks and anti-quarks are grouped into nonets with the same J^{PC}. A summary of the established multiplets is shown in table 4 together with a list of new 'unclassified' objects. However, as will be discussed in the next chapter, in the 1^{++} nonet for example, the D'(1525)

Table 4: Meson multiplets (old and new names)

J^{PC}					Unclassified
0^{-+}	K	π	η	η'	ι
$^1S_0$ ↑↓	K(494)	π(140)	η(549)	η'(958)	$\rho\rho$, $\omega\omega$
1^{--}	K^*	ρ	ω	ϕ	
$^3S_1$ ↑↓	K^*(892)	ρ(770)	ω(783)	ϕ(1020)	
1^{+-}	Q_2	B	H		
$^1P_1$ ↑↓	K_1(1400)	b_1(1235)	h_1(1190)		
0^{++}	κ	δ	ϵ	S^*	S_1(993)
$^3P_0$ ↑↓	K^*_0(1350)	a_0(980)	f_0(1300)	f_0(975)	G(1590)
1^{++}	Q_1	A_1	D	E	D'(1525)
$^3P_1$ ↑↓	K_1(1280)	a_1(1270)	f_1(1285)	f_1(1420)	
2^{++}	K^*(1430)	A_2	f	f'	θ
$^3P_2$ ↑↓	K^*_2(1430)	a_2(1320)	f_2(1270)	f'_2(1525)	g_1

may in fact be the member of the nonet and not the $f_1(1420)$. Hence, searches for gluonic states are hampered by our poor understanding of normal quarkonium states.

Glueballs, being singlet states in $SU(3)_{colour}$ and $SU(3)_{flavour}$, can neither carry isospin, nor charge, nor flavour. Naively, the decay of glueballs should reflect their singlet nature of $SU(3)_{flavour}$ and thus show a flavour symmetric pattern of decay. However, several authors [18] have argued that an SU(3) symmetric decay pattern on the quark/gluon level need not be maintained at the hadron level. Firstly, calculations carried out using the bag model [12] have shown that although TE mode gluons couple in a flavour independent way to $q\bar{q}$, TM mode gluons couple preferentially to kaons. Also, form factor effects [19] and mixing with ordinary quark states [20] have been invoked to explain a suppression of the $\pi\pi$ decay mode of glueballs.

For hybrid states the fact that the bag model predicts that TM mode gluons decay in a flavour dependent way means that the decay of a $q\bar{q}g_{TM}$ hybrid will decay preferentially to final states including strange particles. For example, a 1^{++} hybrid state composed of a non-strange $q\bar{q}$ pair and a TM mode gluon will decay preferentially to a $K^*\bar{K}$ pair ($K\bar{K}$ is forbidden due to parity conservation).

For the purpose of guiding searches it is best to rely on the following general properties of gluonic states,

1. To look for "oddballs", states with J^{PC} quantum numbers not allowed for normal $q\bar{q}$ states. For example $J^{PC} = 1^{-+}$.

2. To look for extra states, that is states that have quantum numbers of an already completed nonet and that have a mass which is sufficiently low that it is unlikely to be a member of the radially excited nonet and hence it can not be described as being a pure $q\bar{q}$ state.

3. To look for states preferentially produced in gluon rich processes. These processes are described in the following section.

1.6 The experimental search for gluonic states

Fig. 2 summarises several dynamical configurations which have been suggested as possible sources of gluonium and where experiments have been performed.

1. The J/ψ decay is believed to be a highly glue rich channel either via the hadronic decay shown in fig. 2a, or via the radiative decay shown in fig. 2c.

2. Pomeron – Pomeron scattering is shown in fig. 2b. The Pomeron is an object that is thought to be a multi – gluon state, which is thought to be responsible for the large cross sections of diffractive reactions. Double Pomeron Exchange (DPE) is considered to be a possible source of glueballs.

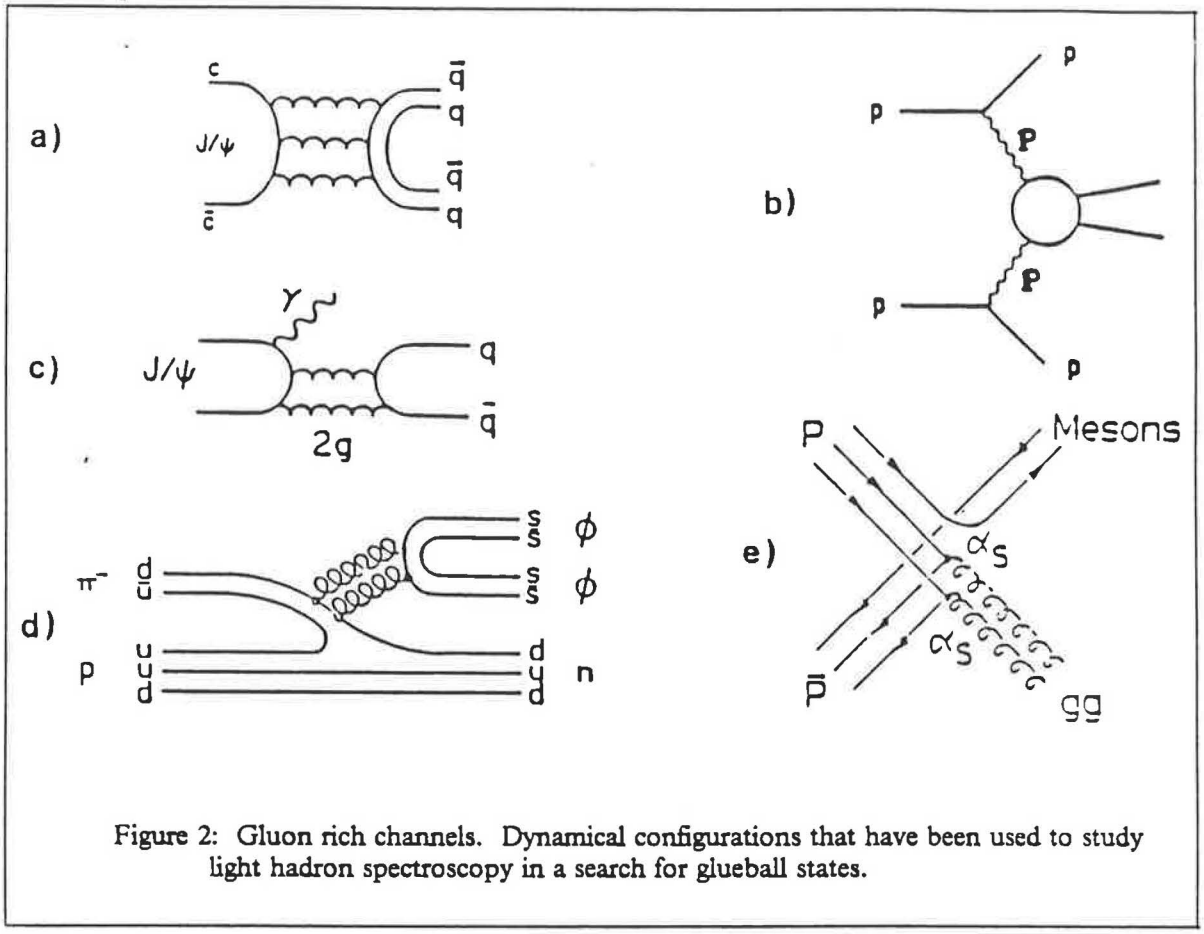

Figure 2: Gluon rich channels. Dynamical configurations that have been used to study light hadron spectroscopy in a search for glueball states.

3. Special hadronic reactions, an example of which is shown in fig. 2d where the $\phi\phi$ system is thought to be produced via an intermediate state containing gluons. Reactions of this kind which have disconnected quark lines are said to be OZI violating [21].

4. Fig. 2e shows proton antiproton annihilation; the annihilation region of quarks and antiquarks is a source of gluons where glueballs and hybrids could be produced.

A summary of candidate states that have appeared through the study of these production processes is given in the next chapter.

1.7 Four-quark states.

Before leaving this introductory chapter, in order to complete the picture of non $q\bar{q}$ mesons something must be said about four-quark states.

The fact that most meson resonances can be accommodated in the simple $q\bar{q}$ classification is quite remarkable, since the light mesons constitute relativistic systems. If $qqq\bar{q}$,$qqqq\bar{q}q$, etc. wave functions were important for meson spectroscopy it would have been much harder to establish the quark model and QCD.

In principle, evidence for four-quark states could easily be found by searching for exotic quantum numbers, e.g. states with charge or strangeness 2. However, no tell-tale candidates for $qqq\bar{q}$ states have yet been found.

Bag model calculations [22] predict that

1. the lowest lying $qqq\bar{q}$ states do not carry exotic quantum numbers and form nonets carrying the same quantum numbers as $q\bar{q}$ nonets, and

2. most $qqq\bar{q}$ states can fall apart into two colour singlet mesons and thus have a decay width of the order of their mass, too wide to be detected as resonances.

The only four-quark states that may be observable are those whose nominal mass is below threshold for their principal fall-apart decay mode. It has been argued [22] that $f_0(975)$ and $a_0(980)$ are candidates for the $I=0$ $s\bar{s}(u\bar{u} + d\bar{d})$ and $I=1$ $s\bar{s}d\bar{u}$ states of the lowest lying scalar four-quark nonet. Because of their quark content these states will couple strongly to $K\bar{K}$. However, being below the $K\bar{K}$ threshold these decays are strongly suppressed by phase-space. For the $f_0(975)$ the remaining dominant channel is $\pi\pi$ which requires an OZI violation to annihilate the $s\bar{s}$ pair.

There is a similar possibility that $qqq\bar{q}$ states can also be observed near $K^*\bar{K}$ threshold. This point will be discussed in the next chapter.

2. THE STATUS OF SEARCHES FOR GLUONIC STATES

2.1 Introduction

The standard theory of colour forces (QCD) suggests that in addition to the familiar hadrons made of quarks, there should exist new states where coloured gluons play an essential dynamical role. The experimental status of gluonium spectroscopy is still confused and up to now no particle has been established as a gluonic state. However, there are several very promising candidates which will be outlined in the following sections with special emphasis being given to those studied by experiment WA76. A list of recent review articles is given in reference [23].

2.2 The E/ι Puzzle

At present there is some uncertainty as to the number of states present in the $(K\bar{K}\pi)^0$ mass spectrum around 1.4 GeV/c^2. Some experiments observe a $J^{PC} = 0^{-+}$ state, called the $\iota/\eta(1440)$, while others observe a $J^{PC} = 1^{++}$ state, called the $E/f_1(1420)$. The interest in this region is that one of these states could be a glueball or hybrid [24]. This situation has become known as the E/ι puzzle and the latest results are discussed in the following sections.

2.2.1 The 0^{-+} states

For J = 0 there are ground states and radial excitations, but no orbital excitations. The 0^- ground state (1S) nonet is one of the best established $q\bar{q}$ multiplets and its first radial excitation (2S) is also relatively well known. The isotriplet $\pi(1300)$, the strange quartet K(1460) and the $\eta(1275)$ are all established states and can be assigned as eight of the nine members of this nonet. The most plausible candidate for the ninth member is the $\eta(1400)$ observed in the reaction

$$\pi^- p \rightarrow \eta\pi\pi n$$

at KEK [25] and in the reaction

$$\pi^- p \rightarrow K\bar{K}\pi n$$

at BNL [26].

In 1980 an analysis of the decay of $J/\psi \to \gamma K\bar{K}\pi$ by the Mark II collaboration [27] found evidence for a state with $J^{PC} = 0^{-+}$, a mass of 1460 MeV/c^2 and a width of 80 MeV/c^2. This state was later confirmed by the Crystal Ball collaboration [28] using the same reaction but with higher statistics. It decays predominantly to $a_0(980)\pi$ and is called the $\iota/\eta(1440)$. Based on the fact that it constitutes a large fraction ($\approx$ 5-10 %)[1] of the radiative J/ψ width it is considered to be a good glueball candidate. However, as shown in fig. 3a), a fit with a single Breit-Wigner does not describe the $\iota/\eta(1440)$ structure very well (χ^2 probability = 1.4×10^{-3}).

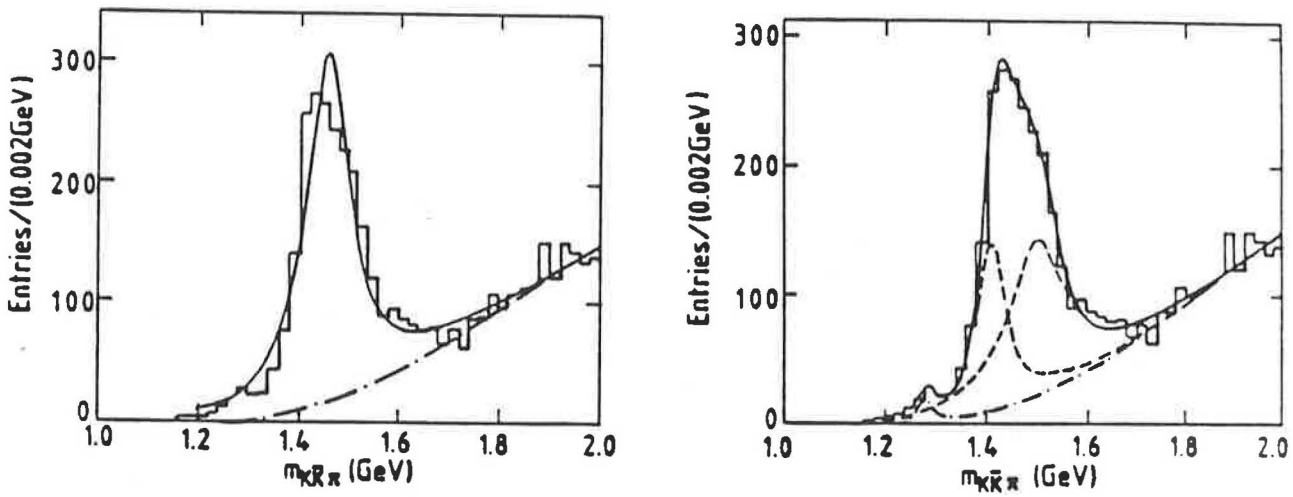

Figure 3: The $K^0_S K^{\pm}\pi^{\mp}$ mass spectrum from radiative J/ψ decays. The fits are described in the text.

[1] Depending on the number of decay channels considered.

A recent study by Mark III [29] has revealed that the $\iota/\eta(1440)$ structure may in fact be more than just one resonance and may have a substantial $K^*\overline{K}$ decay mode. In fig. 3b the data have been fit by two interfering Breit-Wigner amplitudes and gives a χ^2 probability of 58 %. This fit requires two 0^{-+} states with

$$m_{low} = (1409 \pm 5)\ MeV/c^2 \qquad \Gamma_{low} = (69 \pm 11)\ MeV/c^2$$
$$m_{high} = (1499 \pm 9)\ MeV/c^2 \qquad \Gamma_{high} = (138 \pm 25)\ MeV/c^2$$

The low mass state is compatible with the $\eta(1400)$, while the gluonic nature of the higher mass state still requires testing.

2.2.2 The 1^{++} states

In 1980 an experiment studying the reaction

$$\pi^- p \rightarrow K^0_S K^{\pm}\pi^{\mp} n$$

at 3.95 GeV/c [30], in the CERN 2m bubble chamber, reported the observation of a state with a mass of 1425 MeV/c^2 with a width of 60 MeV/c^2 decaying to $K^*\overline{K}$ with $J^{PC} = 1^{++}$, called the E/f_1(1420).

The $K^0_S K^{\pm}\pi^{\mp}$ mass spectrum observed by experiment WA76 at 85 GeV/c [31] is shown in fig. 4. A Dalitz plot analysis shows that both structures have $J^{PC} = 1^{++}$ and they were identified as being the $f_1(1285)$) and E/f_1(1420) mesons. The results from the 300 GeV/c data are presented in a later chapter.

The E/f_1(1420) was thought to be the $s\bar{s}$ isoscalar member of the ground state 1^{++} nonet, the other members being the $a_1(1260)$ triplet, the $K_1(1270)$ and the $f_1(1285)$. However, it is not seen in K^- incident experiments where $s\bar{s}$ objects should be preferentially produced. Instead in the reaction [32]

$$K^- p \rightarrow K^0_S K^{\pm}\pi^{\mp}\Lambda$$

a state is observed with a mass of 1527 ± 5 MeV/c^2 and a width of 106 ± 14 MeV/c^2, called the D′/f_1(1530). A partial wave analysis shows that it has $J^{PC} = 1^{++}$ and that it decays to $K^*\overline{K}$. It has

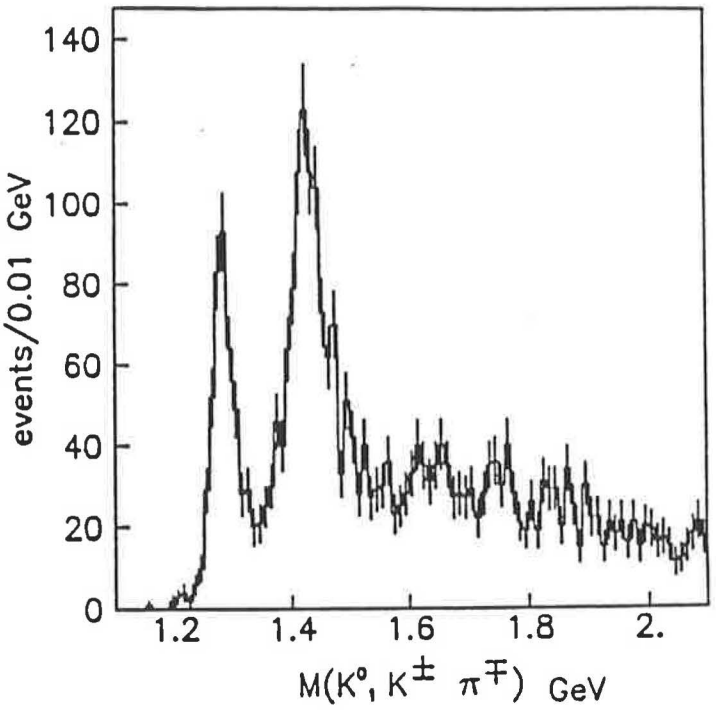

Figure 4: The $K^0_S K^{\pm}\pi^{\mp}$ mass spectrum observed by experiment WA76 at 85 GeV/c.

been suggested that this state is a better candidate for the $s\bar{s}$ member of the 1^{++} nonet, if so, then the $E/f_1(1420)$ is left as an extra state.

Further information comes from experiments studying $\gamma\gamma$ collisions [33] where a state is observed in the $K^0_S K^{\pm}\pi^{\mp}$ mass spectrum having a mass and width consistent with the $E/f_1(1420)$. This state is only seen when one of the two γ's is off mass shell (fig. 5b) and not when both γ's are real (fig. 5a) which via Yang's theorem [34] indicates a spin 1 state. A spin-parity test [35] shows that it is consistent with having $J^{PC} = 1^{++}$.

The $\gamma\gamma^*$ width for the $E/f_1(1420)$ meson is found to be

$$\Gamma(E) = 4 \pm 1 \pm 1 \text{ KeV/c}^2$$

but the $\gamma\gamma^*$ width has been calculated to be $\Gamma(E) = 0.1$ KeV/c^2 assuming the $E/f_1(1420)$ to be a $s\bar{s}$ state [36]. This therefore suggests that the $E/f_1(1420)$ has a large light quark content. However the

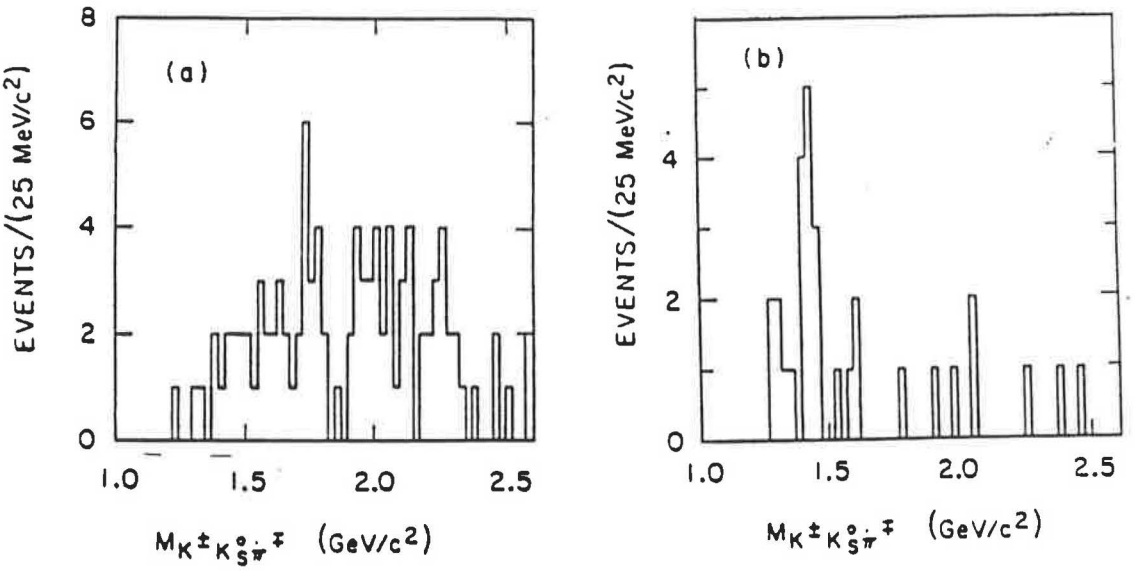

Figure 5: The $K^0_S K^\pm \pi^\mp$ mass spectrum for a) $\gamma\gamma$ and b) $\gamma\gamma^*$ collisions.

$f_1(1285)$ is the undisputed light quark member of the ground state 1^{++} nonet, so that if the $E/f_1(1420)$ is a $q\bar{q}$ state it would have to be a member of an excited nonet.

S. Godfrey and N. Isgur [37] have produced a relativistic quarkonium model with QCD in which all $q\bar{q}$ mesons from pions to upsilons are described in a unified framework (GI model). Their predicted mass spectra not only fit most known meson states but also their decay modes involving hadrons and photons [38]. According to this model the lowest mass excited 1^{++} state should have a mass of 1820 MeV/c².

Therefore it would appear that the $E/f_1(1420)$ cannot be explained as a conventional $q\bar{q}$ state. As a 1^{++} state its mass is too low to be a glueball or hybrid state, and a possible explanation is that it is a four quark [39] or $K^*\bar{K}$ molecule [40].

2.2.2.1 The 1^{++} nonet mixing angle

In order to compare the suitability of the $E/f_1(1420)$ and the $D'/f_1(1530)$ as the $s\bar{s}$ isoscalar member of the 1^{++} nonet the nonet mixing angle (θ_A) has been calculated for the two candidates. Firstly using the SU(3) mass formula [41]

$$\cos^2\theta_A = \frac{4<K_A|K_A> - <a_1|a_1> - 3<D|D>}{3(<X|X> - <D|D>)}$$

where θ_A is the octet-singlet mixing angle,. $<\alpha|\alpha>$ is the matrix element between the Hamiltonian and is set equal to the $(mass)^2$ of the state α, X represents either $E/f_1(1420)$ or $D'/f_1(1530)$ depending on the hypothesis and K_A refers to the pure 1^{++} SU(3) strange state.

The observed $J^P = 1^+$ strangeness states, the $K_1(1270)$ and $K_1(1400)$, which belong to the 1^{++} and 1^{+-} nonets respectively, are mixtures of the pure quark states K_A and K_B. The mixing occurs because the strange states do not have a definite C-parity and hence have identical quantum numbers. The state K_A is given by

$$<K_A|K_A> = (1/2)(<K_1|K_1> + <K_2|K_2> + (<K_1|K_1> - <K_2|K_2>)\cos 2\theta_Q)$$

where θ_Q is the $1^{++} - 1^{+-}$ mixing angle and K_1 and K_2 are defined in table 5.

A second method of calculating the nonet mixing angle is to use the SU(3) coupling formula [41]

$$\Gamma(X \to K^*\bar{K}) = \frac{<q_{K^*}>}{M^2_X} g^2_A \cos^2\theta_A$$

where q_{K^*} is the K^* momentum in the decay rest frame, g_A is the SU(3) coupling constant for the 1^{++} nonet and θ_A is the 1^{++} nonet mixing angle.

Values of g_A and θ_Q come from a fit to the partial decay widths of $K_1(1270)$ and $K_1(1400)$ [41], and the masses and widths for the resonances are given in table 5 [42]. These data yield the following mixing angles

Table 5: The 1^{++} nonet mixing angle

θ_Q		$(41 \pm 4)^0$
g_A		1670 ± 180 MeV/c^2
a_1	$a_1(1260)$	1260 ± 30 MeV/c^2
K_1	$K_1(1270)$	1270 ± 10 MeV/c^2
K_2	$K_1(1400)$	1401 ± 10 MeV/c^2
D	$f_1(1285)$	1283 ± 5 MeV/c^2
E	$f_1(1420)$	1422 ± 10 MeV/c^2
D′	$f_1(1530)$	1527 ± 5 MeV/c^2
$\Gamma(E \to K^* \bar{K})$		55 ± 3 MeV/c^2
$\Gamma(D' \to K^* \bar{K})$		106 ± 14 MeV/c^2

	Mass Formula	Coupling Formula
$E/f_1(1420)$	$(47 \pm 8)^0$	$(72 \pm 2)^0$
$D'/f_1(1530)$	$(60 \pm 7)^0$	$(63 \pm 1)^0$

The two angles are more consistent for the $D'/f_1(1530)$ than for the $E/f_1(1420)$ and hence it would appear that the $D'/f_1(1530)$ is a better candidate for being the $s\bar{s}$ member of the 1^{++} nonet than the $E/f_1(1420)$.

It is interesting to note that if the $D'/f_1(1530)$ is the member then the 1^{++} mixing angle is far from the ideally mixed value of $\theta_A = 35^0$ [43] and would require the $f_1(1285)$ to have a strange quark content. However this is not inconsistent with observations of the $f_1(1285)$ in hadronic J/ψ decays where it is seen recoiling against both the ϕ and ω [44].

2.3 The 2^{++} candidates

Although the ground state 2^{++} $q\bar{q}$ nonet is well established ($a_2(1320)$, $K^*_2(1430)$, $f_2(1270)$, $f_2'(1525)$), orbital as well as radial excitations have to be considered and both of these nonets are far from being fully established. However, there are gluonic candidates with $J^{PC} = 2^{++}$ which are discussed below.

2.3.1 The $\theta/f_2(1720)$

The most promising 2^{++} glueball candidate is the $\theta/f_2(1720)$, the first evidence for which came from the study of the radiative J/ψ decay to $\eta\eta$ by the Crystal Ball Collaboration [45]. This new state was confirmed by two different experiments in the K^+K^- and $K^0\bar{K}^0$ channels [46] [47]. The $\theta/f_2(1720)$ has a mass of 1721 ± 4 MeV/c^2 and a width of 138 ± 11 MeV/c^2. A spin parity analysis by Mark III finds that 2^{++} is preferred over 0^{++} with 99 % probability [47]. However, DM2 finds equal likelihood for spin 2 and spin 0 [46]. The $\theta/f_2(1720)$ was observed for the first time in hadronic experiments by experiment WA76 at 300 GeV/c in both K^+K^- and $K^0_SK^0_S$ decay modes (see fig. 6a,b.). A spin parity analysis of the K^+K^- system shows that the θ has $J^{PC} = 2^{++}$ [48].

Since the $\theta/f_2(1720)$ is confirmed to have $J^{PC} = 2^{++}$ and the ground state nonet is complete and well established, if the $\theta/f_2(1720)$ is a $q\bar{q}$ state it would have to be a member of an excited nonet. The lowest lying such multiplet is the (2P) radially excited nonet for which candidate states already exist (the $f_2(1810)$ [49] and the $f_2(1410)$ [50]). The next excited nonet is predicted by the GI model [37] to have isoscalar states with masses greater than 2.0 GeV/c^2.

Evidence for the gluonic nature of the $\theta/f_2(1720)$ comes from the fact that it is not observed in $\gamma\gamma$ collisions where on the other hand the $f_2(1270)$ and $f_2(1525)$ are produced [51], and that it is not produced in peripheral production [52]. However, it is observed in reactions which are believed to be gluon rich i.e. radiative J/ψ decay and central production.

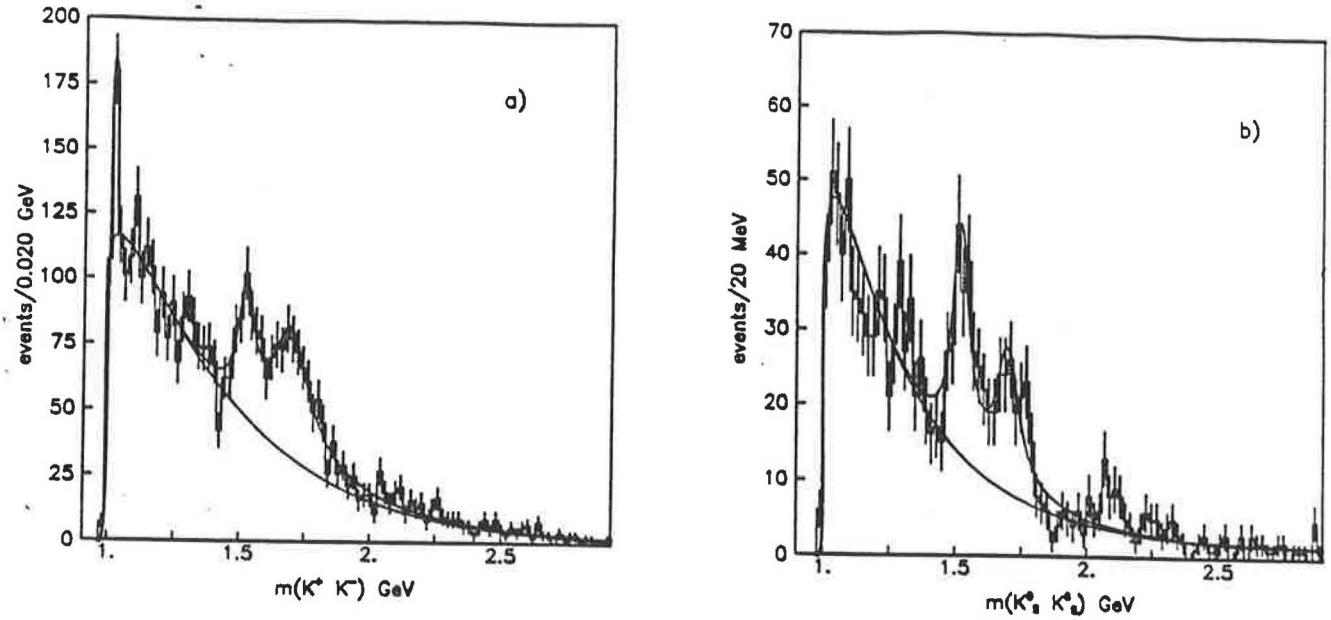

Figure 6: a) The K^+K^- and b) the $K0_SK^0_S$ mass spectra from experiment WA76 at 300 GeV/c.

Therefore the fact that there is an extra 2^{++} state which has only been observed in reactions which are believed to be gluon rich has led to the $\theta/f_2(1720)$ being considered to be a very good glueball candidate.

2.3.2 The $\phi\phi$ channel

Studies of the OZI [53] forbidden reaction

$$\pi^- p \rightarrow \phi\phi n \qquad (1)$$

at 22 GeV/c [54], and 16 GeV/c [55] have shown that it is only suppressed by a factor[2] of ≈ 5 relative to the OZI allowed reaction

$$\pi^- p \rightarrow \phi K^+ K^- n.$$

[2] Throughout this thesis a correction has been made for the unseen decay modes of the ϕ. The ratio of ≈ 10 quoted in [54] was for $\phi \rightarrow K^+K^-$ only.

This has been interpreted as a breakdown of the OZI rule due to the production of gluonic intermediate states [56].

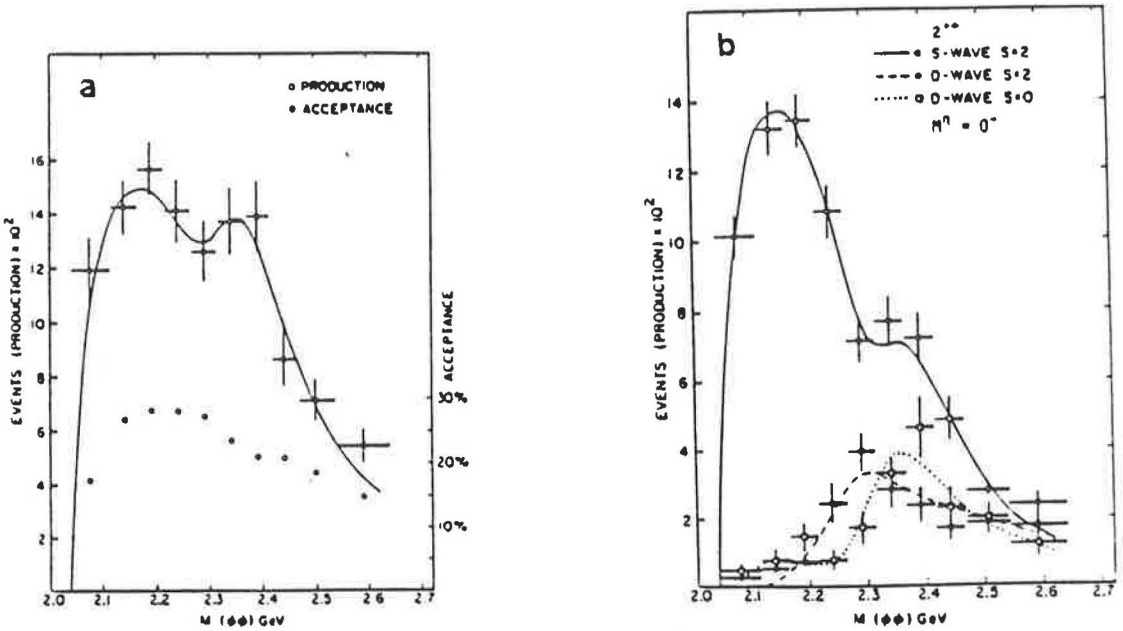

Figure 7: a) The $\phi\phi$ mass spectrum and b) partial waves from the BNL/CCY Collaboration.

A spin parity analysis of the $\phi\phi$ system observed by the BNL/CCY Collaboration [57] gives evidence for three $J^{PC}=2^{++}$ states (called the g_T's), which constitute most of the $\phi\phi$ cross section (see fig. 7), having masses and widths of (in MeV/c^2),

$$M_1 = 2011 \pm 70 \qquad \Gamma_1 = 202 \pm 65$$

$$M_2 = 2297 \pm 28 \qquad \Gamma_2 = 149 \pm 41$$

$$M_3 = 2339 \pm 55 \qquad \Gamma_3 = 319 \pm 80.$$

Two of these states could be accounted for in the orbitally excited (1F) nonet which would leave one extra state.

The same reaction has been studied, inclusively, at the CERN Ω Spectrometer by the WA67 Collaboration using a π^- beam on a Be target at 85 GeV/c [55]. A fit to the $\phi\phi$ mass spectrum using a smooth background and two resonances gives (in MeV/c^2),

$$M_1 = 2231 \pm 10 \qquad \Gamma_1 = 133 \pm 50$$
$$M_2 = 2392 \pm 10 \qquad \Gamma_2 = 195 \pm 50.$$

Due to the large errors quoted by the BNL/CCY analysis, it is difficult to establish a real compatibility in these results.

The problems with interpreting one of the g_T states as being a glueball are

1. The OZI rule is an empirical law and its limits of validity are not clear [58].

2. The states are only revealed using a partial wave analysis.

3. The states have not been observed in $J/\psi \rightarrow \gamma\phi\phi$ which is found to be dominated by $J^{PC} = 0^{-+}$ [59].

In conclusion, the g_T states require confirmation preferably in a gluon rich channel that does not rely on the OZI rule. Results on the $\phi\phi$ production observed in experiment WA76 are presented in chapter 7.

2.4 The 0^{++} glueball candidates

Although the 0^{++} glueball is predicted to have the lowest mass, experimentally it is the most difficult to find. Naive calculations of the mass of the lightest glueball, using the bag model, suggested

that the mass for such a state should be around 1 GeV/c^2 [60]. However, more recent calculations based on lattice gauge theory and flux tube models predict a mass in the region of 1.5 GeV/c^2 [16] [17].

Peaks and structures with $J^{PC} = 0^{++}$ have been reported, mainly in hadronic production, and the best candidates are discussed below.

2.4.1 In the 1 GeV/c^2 region

Au, Morgan and Pennington [61] have analysed data on central dimeson production from the Axial Field Spectrometer (AFS) at the ISR. In a coupled channel analysis of the I = 0 S-wave $\pi\pi$ and $K\bar{K}$ final states they find three resonances around 1 GeV/c^2 – $S_1(991)$, $S_2(988)$ and $\epsilon(900)$ – where the GI model [37] only predicts two states.

They assign the $\epsilon(900)$ and the $S_2(988)$ to the $(u\bar{u} + d\bar{d})$ and $s\bar{s}$ isoscalar members of the 0^{++} nonet. They then argue that the extra state, the $S_1(991)$, which is equally coupled to $\pi\pi$ and $K\bar{K}$ is a possible scalar gluonium candidate.

2.4.2 In the 1.5 GeV/c^2 region

The GAMS Collaboration have carried out a high statistics study of the reaction

$$\pi^- p \rightarrow (N\gamma)n$$

and have observed the decay of a $J^{PC} = 0^{++}$ state, with a mass of 1587 ± 11 MeV/c^2 and a width of 175 ± 19 MeV/c^2, to $\eta\eta$ [62], $\eta\eta'$ [63] and $4\pi^0$'s [64], which has been called the $G/f_0(1590)$. The fact that its decay into $\eta\eta'$ is approximately three times larger than its $\eta\eta$ decay and that no measurable decay into $\pi\pi$ or $K\bar{K}$ has been seen suggests [65] that the $G/f_0(1590)$ is not a $q\bar{q}$ state.

However, the $G/f_0(1590)$ is not widely accepted as a glueball candidate since the signals are not entirely convincing and it has not been observed by another experiment.

2.5 "Oddball" candidates

An "oddball" is a state which has quantum numbers not allowed for a $q\bar{q}$ state. As was discussed in chapter 1 the lowest lying such state is predicted to have $J^{PC} = 1^{-+}$. The GAMS Collaboration [66] have claimed the observation of such a state in the analysis of the reaction

$$\pi^- p \rightarrow \eta\pi^0 n.$$

The $\eta\pi$ mass spectrum is dominated by the $a_2(1320)$. A plot of the forward-backward asymmetry of the π^0 (relative to the incident π^- beam), evaluated in the Gottfried-Jackson frame, shows a significant structure in the $a_2(1320)$ region. The simplest way to explain such an asymmetry is through an interference effect of a P-wave with the D-wave $a_2(1320)$ signal. A partial wave analysis gives evidence for a structure with a mass of 1406 ± 20 MeV/c^2 and a width of 180 ± 30 MeV/c^2. A P-wave $\eta\pi$ state has $J^{PC} = 1^{-+}$ and $I = 1$.

If this state is confirmed then it is the first clear signal for a state beyond $q\bar{q}$. It could either be a hybrid ($q\bar{q}g$) or multi-quark state.

2.6 Conclusions

The most obvious conclusion is that there is no unambiguous sign of a gluonic hadron. Indeed the main problem in being sure that states are beyond a $q\bar{q}$ interpretation is that $q\bar{q}$ spectroscopy, in particular the dynamics of radial excitations, is not fully understood. There are in fact some theoretically contentious issues as to whether hybrid states are independent or in some sense dual to radial and orbital excitations [18].

Despite these problems there are several interesting states which at present seem hard to explain in terms of being standard $q\bar{q}$ objects.

1. The 0^{-+} nonet and its radial excitation appear to be complete. The original $\iota/\eta(1440)$ seems to be composed of two states, the lower mass one being a 0^{-+} multiplet member while the higher mass one appears to be an extra state, which may have a gluonic composition.

2. The 1^{++} nonet also has an extra state which is the $E/f_1(1420)$. Since glueballs and hybrids are not generally expected to have these quantum numbers in this mass range the E is a good candidate to be a four quark state or a $K^*\overline{K}$ molecule.

3. The $\theta/f_2(1720)$ is probably the best glueball candidate since it is only observed in reactions which are believed to be glue rich.

4. The $\phi\phi$ system is interesting and it highlights the problem in understanding production mechanisms. The three states are only revealed by a complex partial wave analysis and await confirmation preferably by another production mechanism.

5. The 0^{++} groundstate nonet is not well established. There are two 0^{++} candidate gluonic states, the $S_1(991)$ and the $G/f_0(1590)$ both require confirmation.

6. The oddball state claimed by the GAMS Collaboration, if confirmed, would be the first direct evidence for states beyond the $q\overline{q}$ model.

In summary, meson spectroscopy is continually finding new states. There seems to be an underlying trend that the simple SU(3) picture of meson nonets is no longer sufficient and that gluonic and multiquark states are required to complete the picture.

3. WA76′ EXPERIMENTAL DETAILS

3.1 Introduction

The aim of experiment WA76′ [67] is to study exclusive final states formed in the reaction

$$pp \rightarrow p_f (X^0) p_s \qquad (1)$$

at 300 GeV/c, where the subscripts f and s denote the fastest and slowest particles in the laboratory and X^0 represents the centrally produced system which decays into charged and neutral final states.

The experiment was performed using the CERN Ω Spectrometer [68], using the H1 beam line [69] and follows the success of the original WA76 experiment which was carried out in 1982 with a 85 GeV/c beam consisting of 47 % positive pions and 45 % protons.

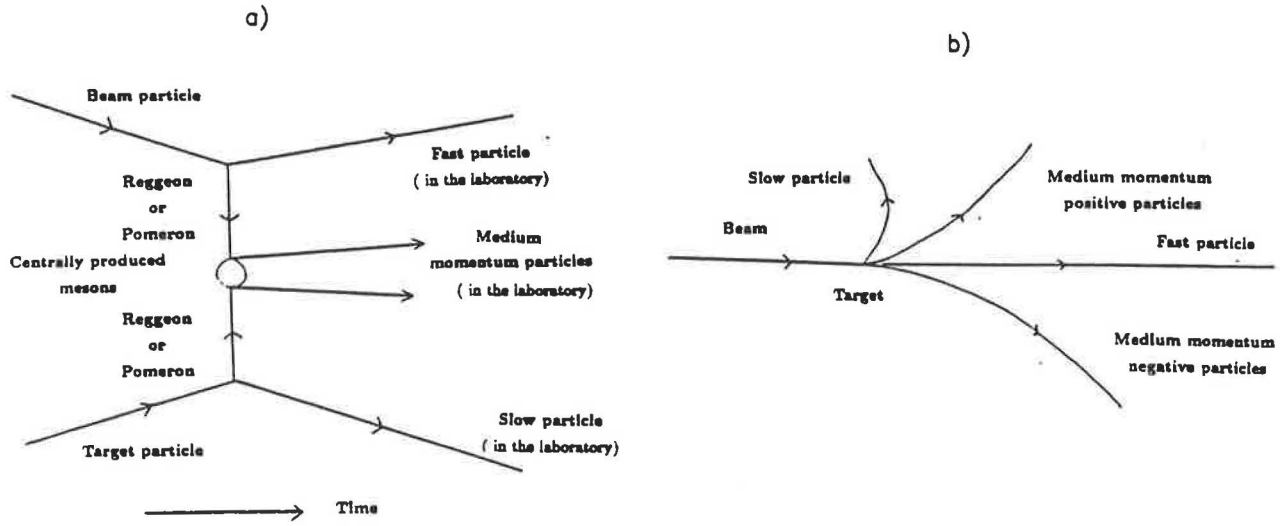

Figure 8: Central production as viewed from a) the centre of mass and b) the laboratory frame.

Fig. 8a shows an example of central production, as viewed in the centre-of-mass, where the central system is produced by a double exchange process. In the laboratory the reaction is as shown in fig. 8b. Reaction (1) at 300 GeV/c was selected by requiring

1. The detection of a fast particle, which had a momentum in the range 200-300 GeV/c.

2. The detection of a slow particle and its identification as being a proton.

3. The requirement of transverse and longitudinal momentum balance between the incident proton and the outgoing particles.

In addition to the above in order to select central production a veto was required on the competing reactions of beam diffraction (fig. 9a) and target diffraction (fig. 9b).

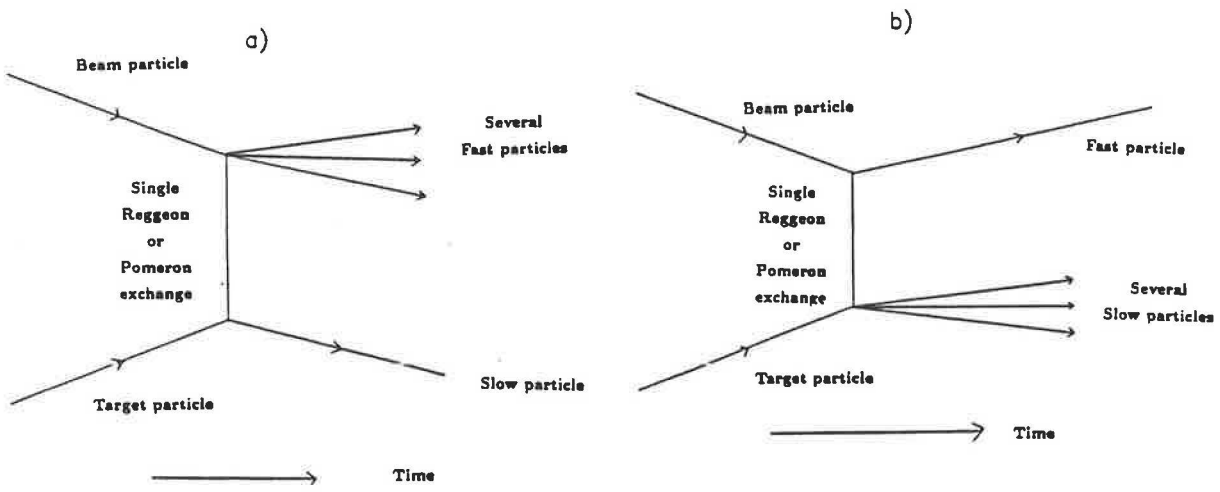

Figure 9: a) Beam diffraction and b) target diffraction.

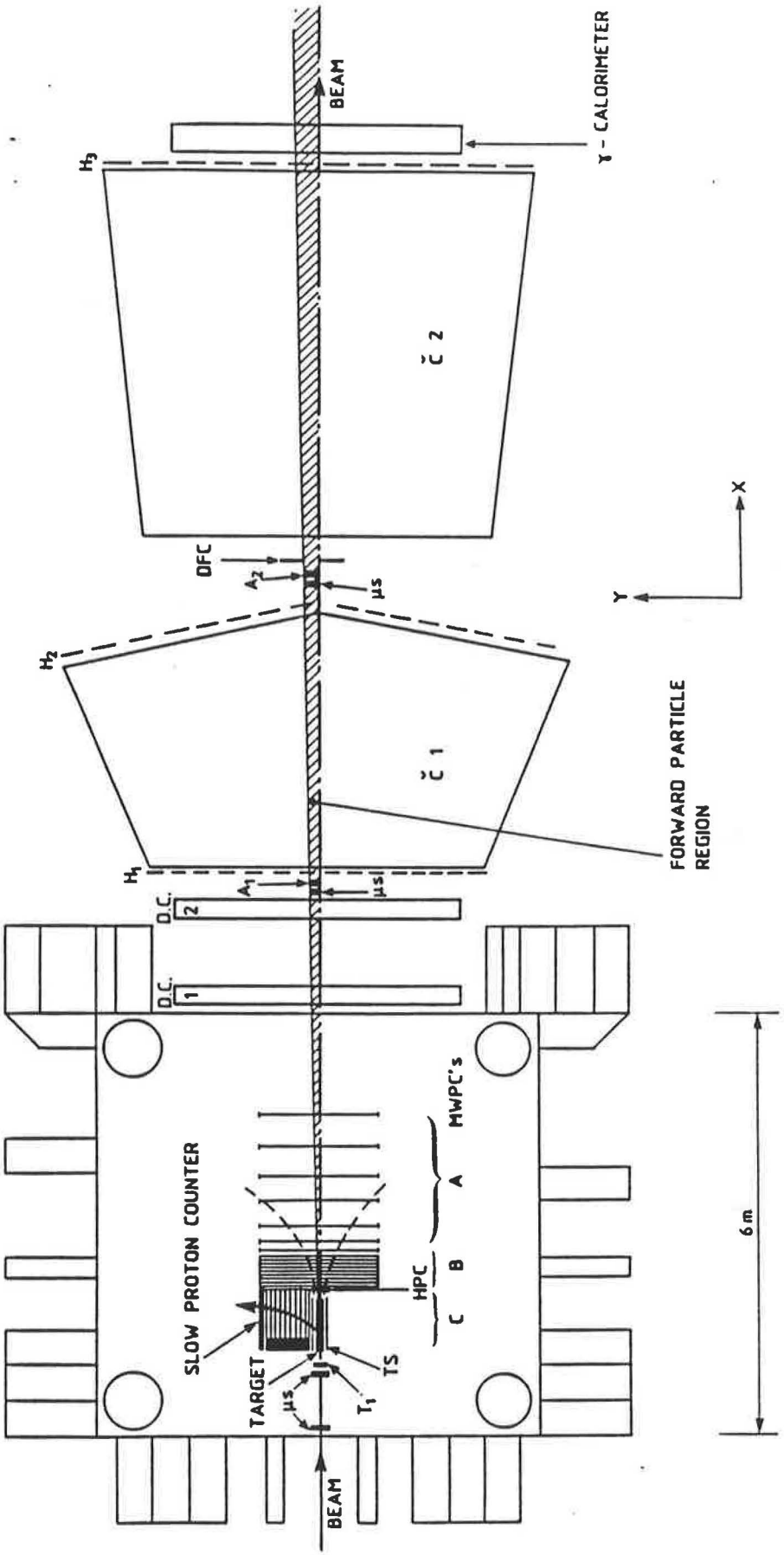

Figure 10: Layout of the Ω′ spectrometer for WA76′.

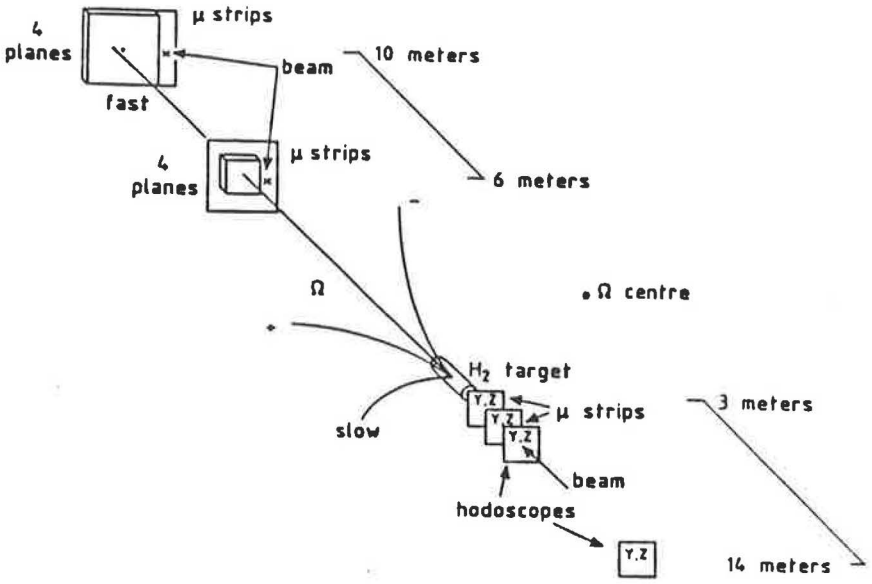

Figure 11: Layout of the μ − strips and scintillators used to measure the beam and the fast particle.

The layout of the Omega Spectrometer and the trigger used to isolate reaction (1) are described in the following sections.

3.2 Experimental layout

The Ω Spectrometer is a multi−user detector designed for measuring interactions with many final state particles. It consists of a pair of superconducting Helmholtz coils that are capable of producing a central field of up to 1.8 T. In WA76 and WA76′ the field used was 1.35 T. The layout of the Ω spectrometer used in experiment WA76′ is shown in fig. 10 and comprises:

1. A set of detectors to perform an accurate measurement of the incident beam direction. This was achieved by using four scintillator hodoscopes (2y and 2z planes) having a 1 mm width and partially overlapped to produce 1/3 mm logical slabs; four 50μm pitch μ−strip detectors (2y and 2z planes) [70] four MWPC's (2y and 2z planes) with 1 mm spacing used essentially to backup the hodoscopes and μ−strip system in case of inefficiency. The beam momentum was 300 GeV/c with a momentum bite of 0.25%.

2. A 60 cm long hydrogen target and a system of scintillator hodoscopes for the definition of the slow proton trigger (as described below).

3. The standard Ω set−up which consists of 16 proportional chambers (A and B) and two large drift chambers (DC). This layout was used to measure the medium momentum tracks leaving the interaction region. In addition 8 MWPC's (C) were used to measure the slow proton trajectory. The A chambers consist of seven modules, each module containing three planes of wires (Y,U,V) where Y planes are inclined vertically in the Omega system, and U,V are inclined at $\pm 10.14^0$ to the vertical. The B and C chambers consist of eight modules, each module consisting of two planes (Y,U or V). The wire spacing in the A, B and C chambers is 2 mm and the gas filling is a mixture of iso−butane and alcohol. The quality of these chambers is such that they run perfectly well without Freon being added to the gas filling. Freon is used in many MWPC's to prevent breakdown occurring. The two high precision drift chambers modules (DC1 and 2), consist of 4 planes (Y,U,Y,V), each plane having a 2.5 cm spacing between the sense and field wires. The drift time is $\approx$5 cm/μs.

4. A system of 8 μ − strip detectors (see fig. 11) placed downstream of the two drift chambers in two sets of 4 planes placed at ≈6 m and ≈10 m from the Ω centre in order to measure the fast track direction. The 6 m planes (2.5× 2.5 cm) had a sequence (y,z,y,v) and the 10 m planes (5× 5 cm) a sequence (u,z,y,y). The first y plane at 6 m was larger (5× 5 cm) than the others and the last y plane at 10 m was shifted by 1 cm with respect to the other planes so they both intersected the beam line for calibration purposes. A small MWPC (one z plane, 1 mm spacing) (TOM) was placed at 6 m to backup inefficiencies in the pattern recognition.

5. A forward identification system consisting of scintillator hodoscopes (H1, H2 and H3) and Cerenkov counters (C1 and C2) for charged particle identification (as described below), and a large electromagnetic calorimeter [71] for the measurement of γ's.

Each strip of the μ − strip detectors is read out individually; after a hybrid charge preamplifier that shapes the pulse to a Gaussian with a width of 50 nsec FWHM, each signal above a selectable threshold is stored into the same encoding system used for the read out of the Ω proportional chambers [72]. The data are finally read out through Romulus interfaces into a VAX 780 computer.

The Cerenkov's C1 and C2 were filled with Freon and CO_2 respectively, which gave π/K/p thresholds of 3.0/10.6/19.5 GeV/c for C1 and 5.0/17.7/33.6 GeV/c for C2. This allowed particle identification as shown in table 6 .

3.3 Experimental trigger

The trigger of the experiment required:

1. A fast particle crossing the downstream μ − strip telescope. This requirement was fulfilled by asking for a coincidence between two scintillation counters (called A_1 and A_2) placed close to each set of downstream μ − strip detectors and designed to cover their acceptance.

Table 6: Momentum ranges for particle identification

Particle separation	Momentum Range (GeV/c)
none	0.0 to 3.0
π from K/p	3.0 to 10.6
π from K from p	10.6 to 19.5
π/K from p	19.5 to 33.6
none	above 33.6

2. A slow particle defined by demanding a hit on any of the fourteen horizontal slabs of the slow proton counter (see fig. 10) (56 × 88 cm^2), a hit in the box TS counter and $\geq$ 1 hit on a single plane of the MWPC's situated on one side of the target.

3. In order to reduce target diffraction the events were required to have no hits in the other three sides of the box TS counter which was left open at its front end to allow particles produced centrally to escape downstream.

4. To reduce the forward diffraction or excitation the events were required to have no hits in two counters (DFC) of dimensions (32 × 30 cm^2) which were placed on either side of the beam and just downstream of Cerenkov C1.

The forward $\mu-$strips and scintillation counters at 6 and 10 m were placed (see fig. 11) in such a way that beam particles were not crossing the $\mu-$strips but passed as close to them as possible. The beam crossed the two extended planes, mentioned above, so as to act as a constant monitor of the $\mu-$strip positions. This layout, with the fast track accepted on the same side as the slow proton automatically excluded elastic scatters.

The data taking was performed in two periods of 17 days; the beam flux was held at 4×10^6 particles on a 4×7 mm^2 (FWHM) spot over a spill of 2.8 seconds and a total of 12 million triggers were recorded. The beam intensity was mostly limited by the capability of the $\mu-$strip detectors to handle high intensity fluxes over periods of several weeks without a major increase in reverse currents.

3.4 The beam

The H1 beam [69] is a secondary beam that is formed when protons that have been accelerated to 450 GeV/c in the SPS are extracted and interact with five beryllium targets (called the T1 target). The resulting beam extracted and focussed using dipole and quadrupole magnets is a high energy, high resolution general purpose beam. Fig. 12 shows the predicted H1 intensities of different hadrons as a function of the outgoing beam momentum for 10^{12} protons of 450 GeV/c incident on one of the 400 mm beryllium targets. As can be seen, at 300 GeV/c protons are the dominant particle by two orders of magnitude.

3.5 The target

The target consisted of a 60 cm long cylinder of liquid hydrogen in a mylar and aluminium container, this represented 15 % of an interaction length. A hydrogen target was used so that the interactions are as clean (i.e. pp) as possible without introducing any nuclear effects that a beryllium target would produce. Beryllium targets are often used so that a similar interaction length can be achieved in a shorter physical space which is advantageous when the reconstruction of the interaction vertex is required. However, in this experiment the vertex position is given to a high degree of precision by the intersection point of the well measured beam and slow proton, so a long target may be used.

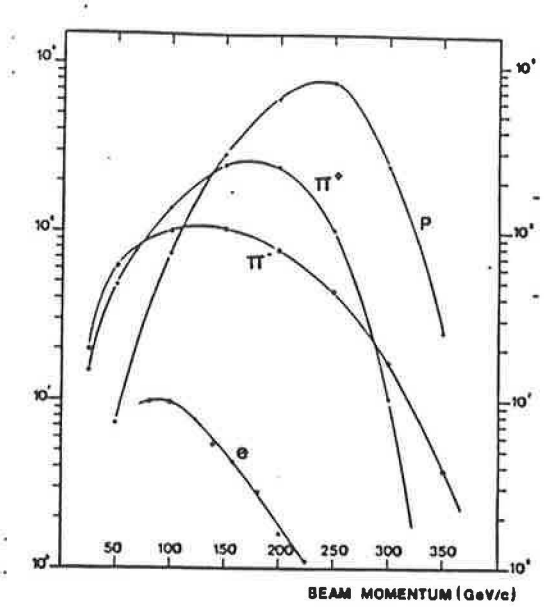

Figure 12: Intensity of hadrons as a function of outgoing beam momentum.

3.6 Event reconstruction and data processing

The event reconstruction has been performed by using a version of the pattern recognition and geometrical reconstruction program TRIDENT [73] modified for the purposes of the present experiment.

The beam reconstruction has been performed by finding straight lines in the (x,z) and (x,y) projections after subtracting the bending due to the magnetic field. The overall reconstruction efficiency for finding the beam track in both projections was 98%. The main vertex has been found by extrapolating the beam to its intersection with the slow proton track.

The fast track pattern recognition has been performed by using the eight $\mu-$strip forward planes with the help of the TOM chamber. The algorithm involves iterating several times along the (x,y) and

(x,z) projections in order to use the information from the inclined strips. The resulting efficiency for finding the track in both projections was ≈96%.

The fast track momentum has then been computed by using the spline fit method [74] with three points only, i.e. the main vertex and the intersections with the 6 and 10 m planes of the forward $\mu-$strips.

For the medium momentum tracks three dimensional space points are found by combining wire hits in several planes at different inclinations. Several planes are necessary, firstly to increase the number of constraints in order to eliminate wrong combinations and secondly, to tackle possible chamber inefficiencies.

The track recognition is based on a three dimensional track following technique. It is initiated in the drift chambers were the tracks are usually well separated by the magnetic bending. Tracks found in the drift chambers are extrapolated back to the A and B chambers where a fit is made to the space points to produce the best track hypothesis. The tracks can either converge to a main vertex or two tracks can converge to form a V^0 vertex. Any tracks not fitting to a vertex are left as extra tracks. TRIDENT allows for two possible geometry hypotheses if an ambiguous event is found.

The output produced by TRIDENT was then run through a V^0 reconstruction program (VZERO) to find V^0's missed by TRIDENT and through a gamma calorimeter analysis program (PHOENIX) that produces a neutral particle data bank.

3.7 Calibration of ADC pulse heights for the side detectors

The side detector consists of three elements. Nearest the target is TS element 1 (TS_1) a 0.5 cm thick scintillator. Then comes sixteen MWPC planes consisting of 8 y−planes and 4 each of u and v−planes. Finally there are the fourteen slabs of the Slow Proton Counter (SPC). Fig. 13 shows the layout of these detectors.

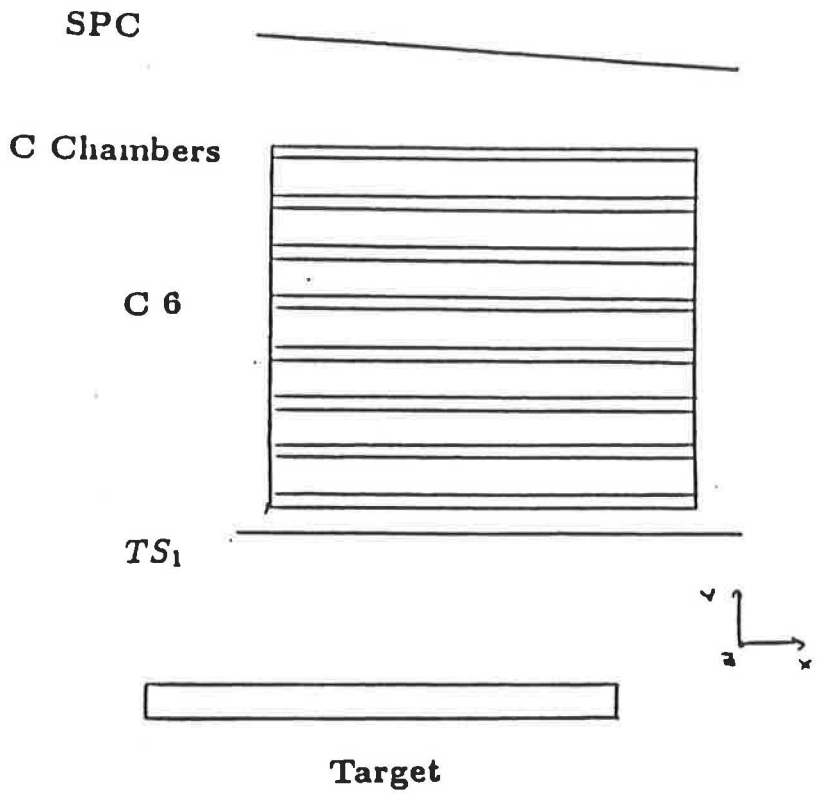

Figure 13: Layout of the side detector.

The Slow Proton Counter (SPC) is composed of 14 slabs of scintillator each of which is 2 cm thick, 6.3 cm high and 56 cm long. The signal produced by a charged particle passing through each scintillator slab is detected by a PhotoMultiplier (PM). The BOX is composed of 8 slabs of scintillator, however only TS_1 is used in the side detector. TS_1 is 0.5 cm thick, 60 cm long and 28 cm high.

The signal produced in these scintillators can be used to discriminate between pions, kaons and protons at a fixed momentum, for momenta in the range $0.3 \leq P \leq 2.0$ GeV/c. Firstly, the signals coming from the 14 slabs of the SPC are normalised and then added together. The resulting spectrum is shown in fig. 14. A clear band corresponding to slow protons can be seen. The maximum pulse height occurs when protons just stop in the scintillator. The line superimposed on fig. 14 shows the cut used to select protons from pions or kaons. Fig. 15 shows the log pulse height versus momentum

for TS_1 and the cut used to select protons. Both of these cuts are used to select events having a slow proton.

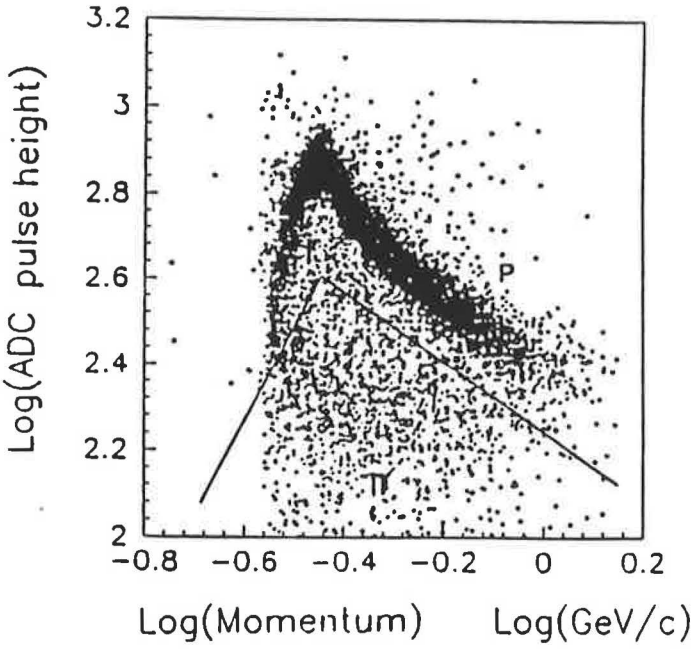

Figure 14: Log(ADC) vs Log(momentum) for the SPC.

3.8 Side detector efficiencies

In calculating any cross sections, correction factors have to be applied to allow for inefficiencies in the trigger. One of these factors is the slow proton trigger and the determination of this efficiency will be described in this section.

The side detector was described in the previous section and it's layout is shown in fig. 13. The slow proton trigger requires a hit in TS_1, a hit in plane C6Y of the MWPC and one or two slabs recording a hit in the SPC. In order to determine the efficiencies runs with special trigger conditions were used in which one of the elements of the detector was omitted from the trigger. In order to be sure that only good tracks were used in the calculation of the efficiencies the tracks were also required

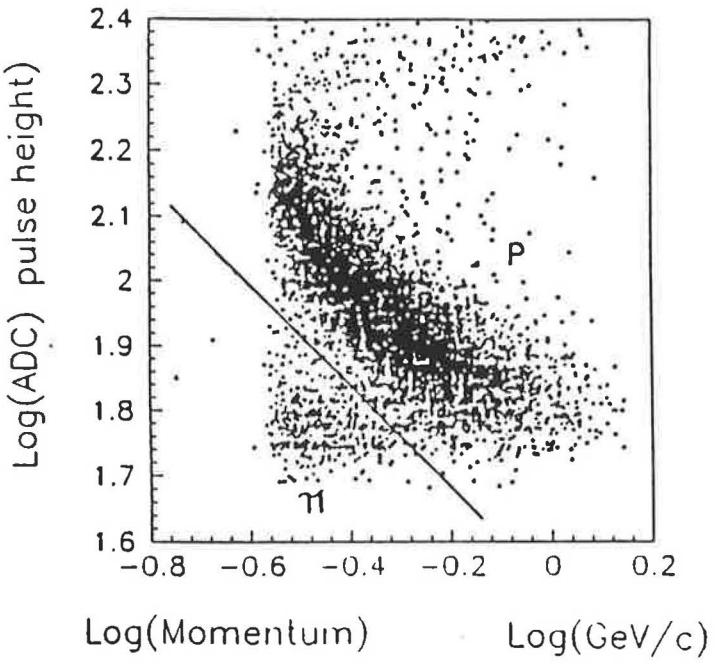

Figure 15: Log(ADC) vs Log(Momentum) for TS_1.

to have positive charge, have ≥ 6 space points per track and have originated from the primary vertex. These tracks were then traced through the magnetic field map using a Runge Kutta routine [75].

If the track was traced successfully to the detector omitted from the trigger the electronic information was checked to see whether a hit had been recorded. For each track the efficiency of each detector was set equal to 1 if the electronic information satisfied the trigger requirement for that detector i.e. for the SPC the efficiency was set to 1 if the slab that had been traced to or either of the adjacent slabs went off. The efficiency of each detector is then given as the number of tracks with efficiency equal to 1 for that detector divided by the total number of tracks.

The efficiency of the individual elements was determined to be

TS_1	=	95.6 ± 0.3 %
C6Y	=	99.3 ± 0.1 %
SPC	=	96.8 ± 0.3 %

and the efficiency of the side detector to detect slow particles is

$$TS_1.C6Y.SPC = 91.9 \pm 0.4\ \%$$

Using the cuts described in the last section the efficiencies for the elements of the side chamber were recalculated this time only considering slow proton tracks. The tracks used were required to have $\geq$ 6 space points, originate from the main vertex, have positive charge and be identified as a proton by one of the other two detectors in the trigger. The tracks were traced to the SPC and were required to give an electronic hit in either of the adjacent slabs. The efficiency of the individual elements was determined to be

TS_1	=	$97.8 \pm 0.2\ \%$
C6Y	=	$99.5 \pm 0.1\ \%$
SPC	=	$96.9 \pm 0.3\ \%$

Therefore the efficiency to detect a slow proton in the side detector is

$$TS_1.C6Y.SPC = 94.3 \pm 0.4\ \%.$$

4. REGGE THEORY RELEVANT TO CENTRAL PRODUCTION

4.1 Introduction

The nuclear force which, for example, binds protons and neutrons into nuclei, is the residual colour polarisation force between the colourless hadrons. This force involves the exchange of coloured quarks and gluons. By the uncertainty principle the range of an exchanged particle of mass m is given by $r = \hbar/mc$ and so the longest range part of the p-n force is provided by the exchange of the lightest colourless composite object which is made up of quarks and gluons. This idea was first suggested by Yukawa [76] in 1935 and was followed by the subsequent discovery of the pion.

Of course heavier states such as the ρ and a_2 can be exchanged but these result in a shorter range. However in high energy hadron scattering because of the small distances involved the exchange of all of these particles has to be considered. A way of doing this was developed by Regge [77] in 1959. This chapter gives a brief overview of Regge theory and its application to double exchange processes.

4.2 Regge theory

If the observed mesons are regarded as $q\bar{q}$ bound states produced by an effective gluon exchange potential, V(r), then the radial Schrodinger equation contains the effective potential

$$V_{eff}(r) = V(r) + \ell(\ell+1)/r^2$$

where the second term is a repulsive centrifugal barrier term. Solving the Schrodinger equation gives

$$\ell = \alpha(m^2)$$

Therefore the mesons are predicted to lie on a straight line trajectory in a plot of ℓ versus m^2 which is found to be the case as is shown in fig. 16.

The particle exchanged in the s-channel process $AB \rightarrow CD$ (fig. 17a) becomes the particle produced in the "dual" t-channel process $A\bar{C} \rightarrow \bar{B}D$ (fig. 17b). The principle of crossing symmetry states that these s and t channels have the same scattering amplitude [77]. Therefore just as the formation of resonances in the t-channel process lie on a linear trajectory so too will the exchanged particles.

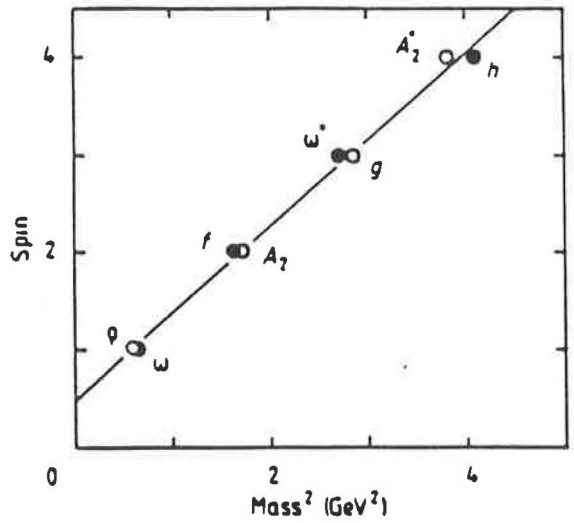

Figure 16: Observed meson trajectories.

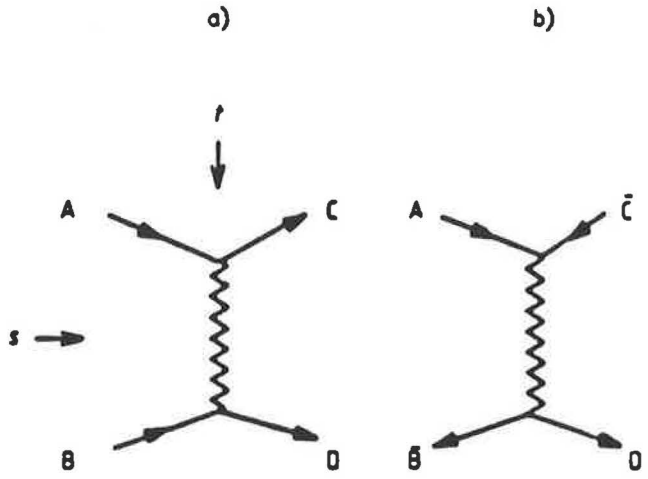

Figure 17: The a) s and b) "dual" t-channel processes.

A general way of parameterising this exchange was suggested by Sommerfeld [78]. The particles are considered to lie on a single linear trajectory

$$\alpha(t) = \alpha_0 + \alpha' t$$

so that $\alpha(t)$ passes through integer values of ℓ at $t = m_\ell^2$ ($\ell = 0,1,2...$). The pole in the lth partial wave is then

$$A_\ell(t) = \beta(t)/(\ell - \alpha(t))$$

hence there is a "Regge pole" in the partial wave at $\ell = \alpha(t)$.

The differential cross section is then [3]

$$\frac{d\sigma}{dt} \approx \frac{F(t)}{(s_0)} \; s^{2\alpha(t)-2} \qquad (1)$$

where $\alpha(t)$ is the leading Regge trajectory which can be exchanged. The trajectory $\alpha(t)$ is determined by plotting $\log(d\sigma/dt)$ as a function of t at different values of s. Table 7 shows some of these trajectories.

Table 7: Leading Regge trajectories

Trajectory	$\alpha(t)$
π	$-0.013 + 0.67t$
ρ or a_2	$0.46 + 0.89t$
ω or $f_2(1270)$	$0.39 + 0.99t$
ϕ or $f_2(1520)$	$0.18 + 0.79t$

Experimentally [3] the high energy forward elastic cross section is found to remain approximately constant with s. If Regge pole exchange is the dominant mechanism then from (1) it must have $\alpha(0)=1$. However as can be seen from table 7 the known quark trajectories have $\alpha(0)\approx 0.5$. Also, elastic cross sections at high s are found to be independent of the flavour of the hadrons, and hence it is generally believed that the trajectory with $\alpha(0)=1$, called the Pomeron, represents gluon exchange [79]. Since no net colour can be transferred the minimum contribution is two gluon exchange.

Although there has been progress in a fundamental understanding of hadron interactions in terms of quarks and gluons in the formulation of QCD, the solutions found thus far are only in the perturbative region of the theory e.g. in deep inelastic scattering. Efforts at developing a non-perturbative QCD theory are nowhere near producing a meaningful phenomenology. Instead the only phenomenological approach available is through the use of Regge theory.

4.3 Double Pomeron Exchange

A fundamental fact of high energy experiments is that elastic scattering and other processes which do not involve the exchange of quantum numbers are characterised by approximately constant cross sections at high energies. These processes may be accommodated in the framework of Regge theory by introducing the concept of the Pomeron, which is thought to be a multi-gluon state.

Regardless of its gluonic content it can be shown that the Pomeron must have isotopic spin zero and positive G parity [80]. Therefore the Pomeron is said to have the quantum numbers of the vacuum. However this is misleading as it could indicate that the Pomeron has spin zero which is not a necessary condition [81].

There has been extensive experimental work done on single particle inclusive cross sections of the type $A+B\rightarrow A+X$ (fig. 18) where the outgoing particle A has Feynman x close to 1 [82]. This process exhibits a large peak in the inclusive cross section for low masses of the system X. The dependence of the cross section, corresponding to this peak, on the centre-of-mass energy $\sqrt{s}$ and the momentum transfer $\sqrt{(|t|)}$ is well described in Regge theory by the exchange of a Pomeron [83].

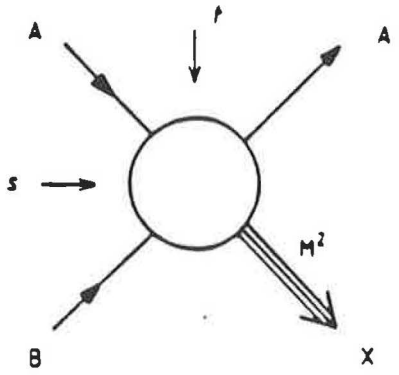

Figure 18: The inclusive process $A+B \rightarrow A+X$.

A possible way of selecting the Double Pomeron Exchange (DPE) process (see appendix C) is to observe the reaction

$$AB \rightarrow AB+X\,,$$

where the outgoing hadrons A and B have $|x_F| \geq 0.9$. From appendix C it can be seen that by using these cuts the mass of the central system (M) is restricted to be

$$M \leq 0.1\sqrt{s},$$

where $\sqrt{s}$ is the centre-of-mass energy. Therefore at low $\sqrt{s}$ a cut on the Feynman x of the two hadrons produces a very restricted mass range.

A more useful method of enhancing the DPE signal is to place a cut on the four-momentum transfer (t) at each vertex. From appendix C,

$$\frac{\sigma(\mathrm{DPE})}{\sigma(\mathrm{BGND})} = (1-x)^{-1.6-0.5|t|}\, e^{-3.3|t|}$$

and hence the DPE signal is enhanced at low |t|.

These predictions will be investigated in the next section where cuts will be used in an attempt to select the DPE and non-DPE (BGND) regions of the WA76 data.

4.4 Double Pomeron Exchange in WA76

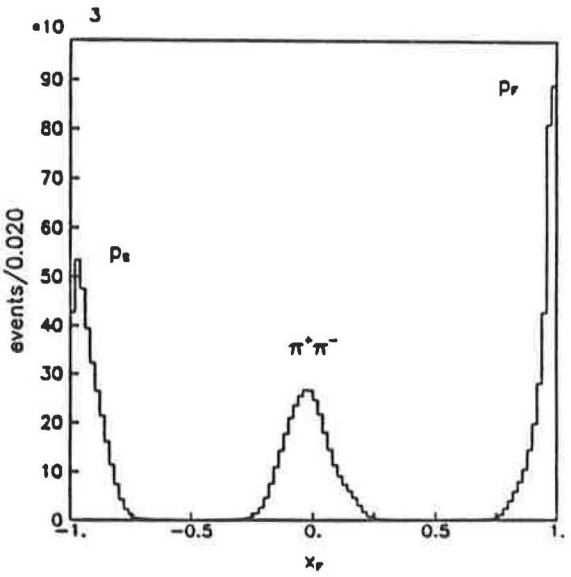

Figure 19: The Feynman x distribution for the $p_f(\pi^+\pi^-)p_s$ system.

In order to investigate the DPE signal in the WA76 data the selection criteria described in the last section will be used on the $\pi^+\pi^-$ channel. The selection of the reaction

$$pp \rightarrow p_f\,(\pi^+\pi^-)\,p_s$$

is described in reference [84] for the 85 GeV/c data and in reference [85] for the 300 GeV/c data. Fig. 19 shows the Feynman x_F distribution for the slow proton, the $\pi^+\pi^-$ system and the fast proton respectively, for the 300 GeV/c data. The majority of the events have the $\pi^+\pi^-$ system concentrated in the region of $|x_F| < 0.2$.

The $\pi^+\pi^-$ channel is of interest because of the presence of the I = 1 $\rho(770)$ meson which can not be formed in DPE and can only be formed in the exchange of at least one Reggeon. Fig. 20a and b show the $\pi^+\pi^-$ spectra at 85 and 300 GeV/c respectively. The $\rho(770)$ signal is clearly suppressed in the 300 GeV/c data. This is consistent with the idea that Reggeon exchange should be suppressed at higher centre-of-mass energies.

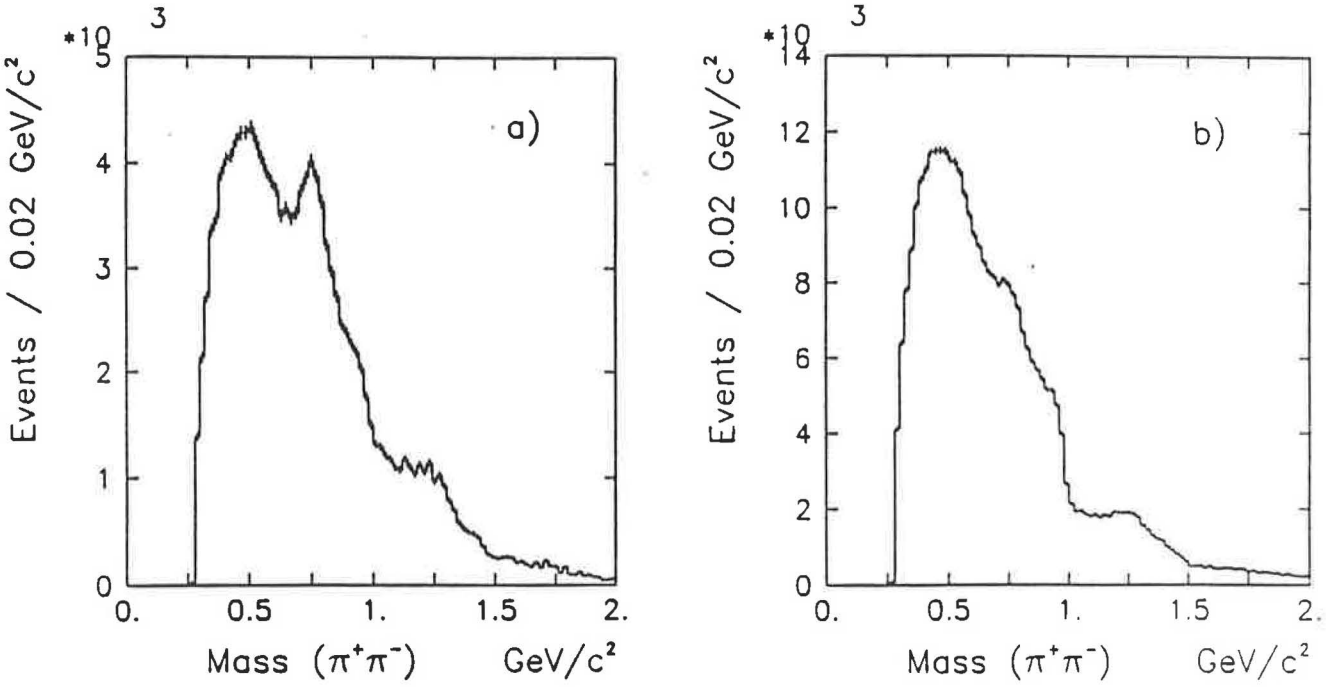

Figure 20: The $\pi^+\pi^-$ mass spectrum for a) the 85 and b) the 300 GeV/c data.

The increase in DPE events with energy can be seen by plotting the variables Z_1 versus Z_2, as defined in appendix C, for the two energies as shown in fig. 21a and b for the 85 and 300 GeV/c data

respectively. As can be seen more of the events lie in the DPE region for the 300 GeV/c data than for the 85 GeV/c data.

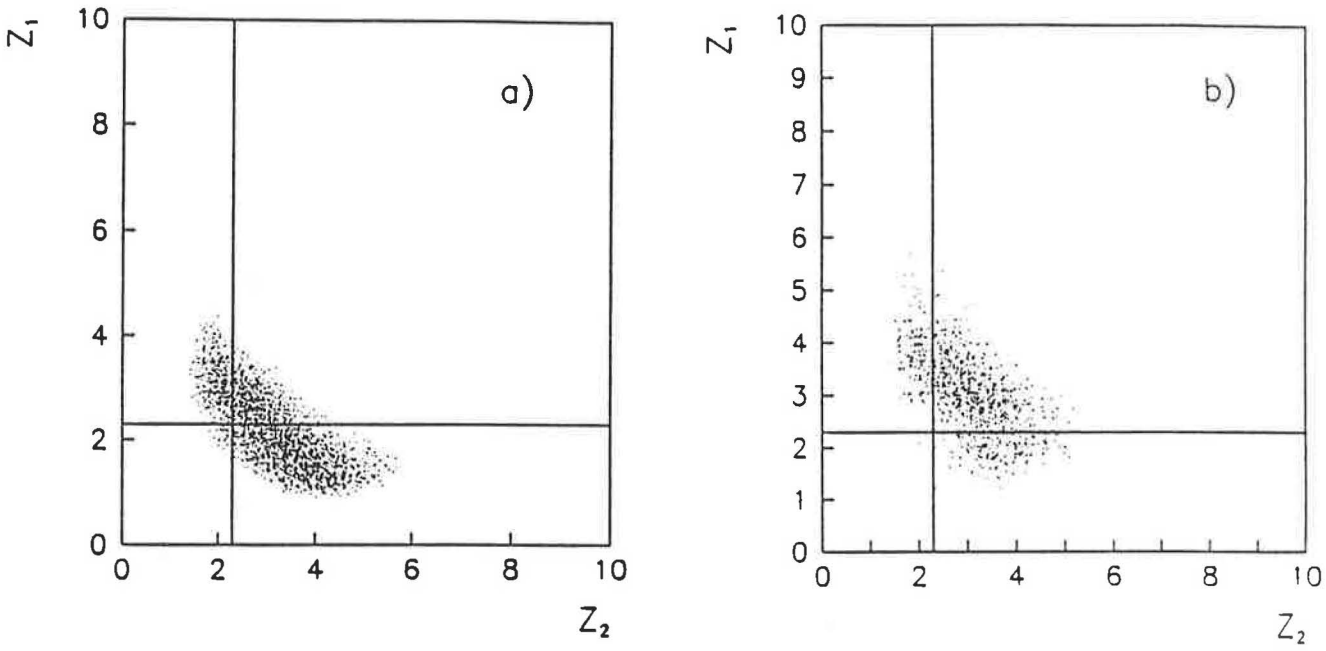

Figure 21: Z_1 vs Z_2 for the $\pi^+\pi^-$ channel at a) 85 and b) 300 GeV/c. The lines correspond to $x_F = 0.9$.

If a cut is placed on the Feynman x of the two outgoing protons in the 300 GeV/c data of $|x_F| \geq 0.9$, so as to define the DPE region then the resulting $\pi^+\pi^-$ spectrum is shown in fig. 22a. Fig. 22b shows the spectra when one of the protons has $|x_F| \leq 0.9$ which represents BGND events. Clearly the $\rho(770)$ is produced dominantly in the BGND region.

Due to the fact that

$$M^2 = s(1-|x_B|)(1-|x_A|)$$

a cut of $|x_F| \geq 0.9$ on the 85 GeV/c data is not very useful as the maximum $\pi^+\pi^-$ mass then is only ≈ 1.2 GeV/c^2 and hence the spectra look distorted.

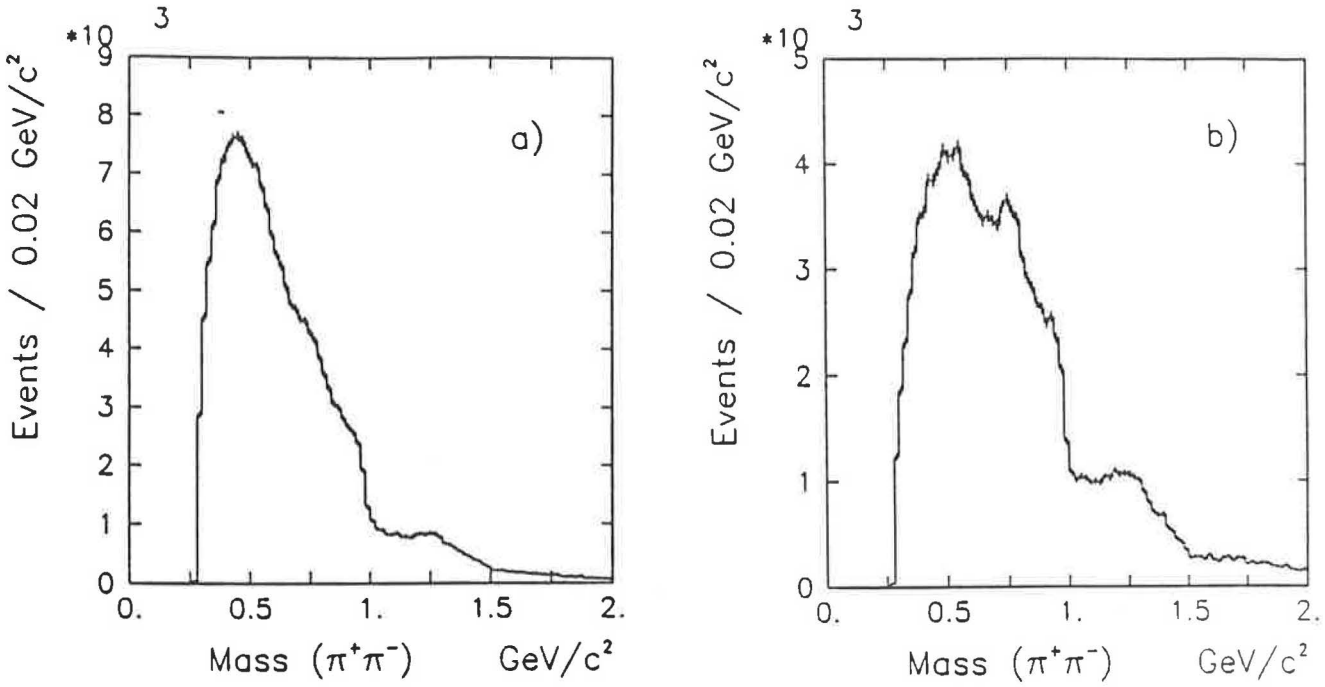

Figure 22: The $\pi^+\pi^-$ mass spectrum at 300 GeV/c for a) the DPE and b) the BGND regions.

The models for DPE also predict a dependence on the four-momentum transferred (t). Fig. 23a shows the $\pi^+\pi^-$ spectra for the case where both the slow and fast vertices have $|t| \leq 0.15$ and fig. 23b when both have $|t| > 0.15$ (GeV)^2. The $\rho(770)$ is produced predominantly at high $|t|$ which is consistent with the prediction that DPE should be dominant at low $|t|$.

4.5 Conclusions

In conclusion, Regge theory predicts that DPE should be dominant

1. at high centre-of-mass energies,

2. when the outgoing protons in the reaction $pp \rightarrow pp + X$ have Feynman x near to 1 and

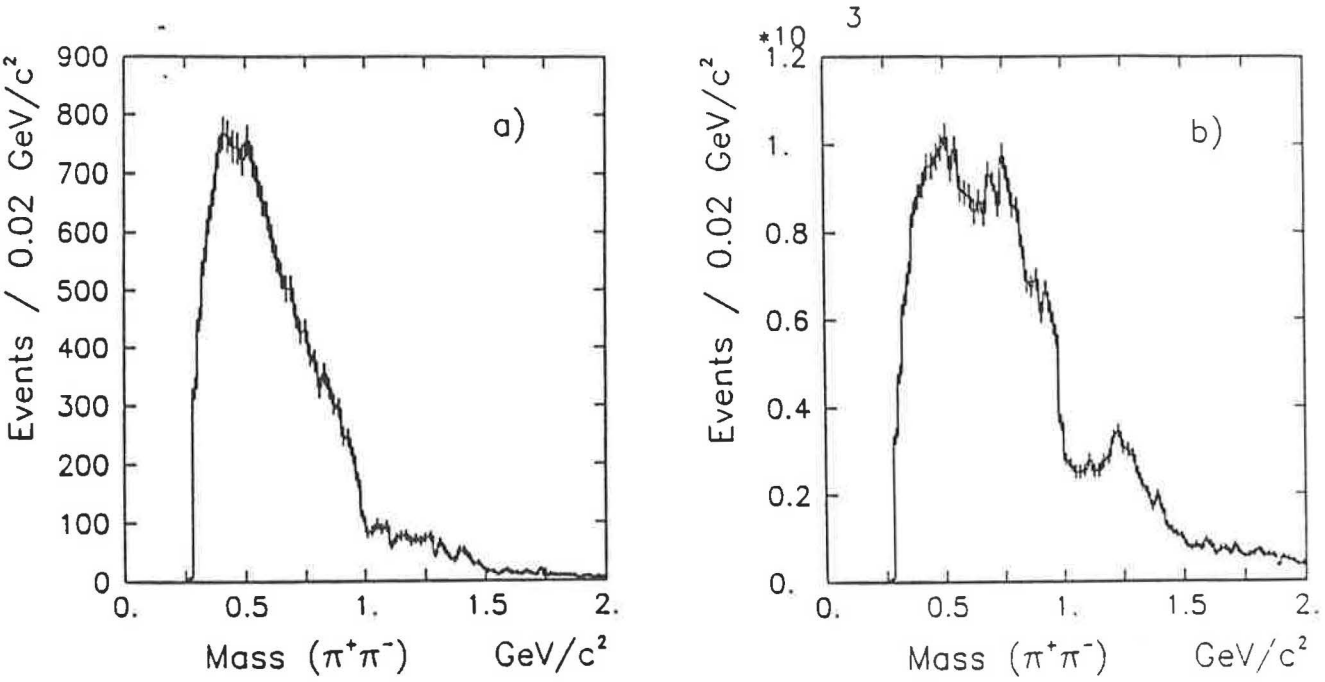

Figure 23: The $\pi^+\pi^-$ mass spectrum for the case where both the fast and slow vertices have a) $|t| < 0.15$ GeV^2 and b) $|t| > 0.15$ GeV^2.

3. when the four-momentum transferred at the exchange vertices is small.

By studying the $\pi^+\pi^-$ spectrum in WA76 and by using the presence of the ρ as a measure of the amount of non-DPE type events it would seem that the WA76 data has a large DPE content and by suitable cuts the DPE signal to background can be increased.

5. THE $K^0_S K^{\pm}\pi^{\mp}$ CHANNEL IN WA76'

5.1 Introduction

As was discussed in chapter 2, there is some uncertainty as to the number of states present in the $(K\bar{K}\pi)^0$ mass spectrum around 1.4 GeV/c^2. The interest in this region is that one of these states could be a glueball or hybrid [24]. A state is observed in radiative J/ψ decays with a mass of 1.46 GeV/c^2 and a spin parity analysis favours $J^{PC} = 0^{-+}$ [28]. A spin 1 object is observed in two photon physics with a mass of 1.42 GeV/c^2 [33]. In hadronic experiments both a 0^{-+} state [26], and a 1^{++} state [30] [31] have been observed with a mass of 1.42 GeV/c^2. The 1^{++} state, the E/$f_1(1420)$, was thought to be the $s\bar{s}$ isoscalar member of the 1^{++} nonet. However, it is not seen in K^- incident experiments where instead an object with $J^{PC} = 1^{++}$ is observed at 1.526 GeV/c^2 [32]. It has been suggested that this last state, the D'(1530), is the $s\bar{s}$ member of the 1^{++} nonet. If so, then a possible explanation of the state at 1.42 GeV/c^2 is that it is a gluonic or four quark state [39].

The following two chapters describe an analysis of the $K^0_S K^{\pm}\pi^{\mp}$ channel from experiment WA76 at 300 GeV/c.

5.2 Selection of the channel $K^0_S K^{\pm}\pi^{\mp}$

The reaction

$$pp \rightarrow p_f (K^0_S K^{\pm}\pi^{\mp}) p_s,$$

has been isolated from the sample of events having four outgoing tracks plus a reconstructed V^0 by first imposing the following cuts on the components of missing momentum,

$$|\text{missing } P_x| < 20.0 \text{ GeV/c.}$$

$$|\text{missing } P_y| < 0.16 \text{ GeV/c.}$$

$$|\text{missing } P_z| < 0.08 \text{ GeV/c.}$$

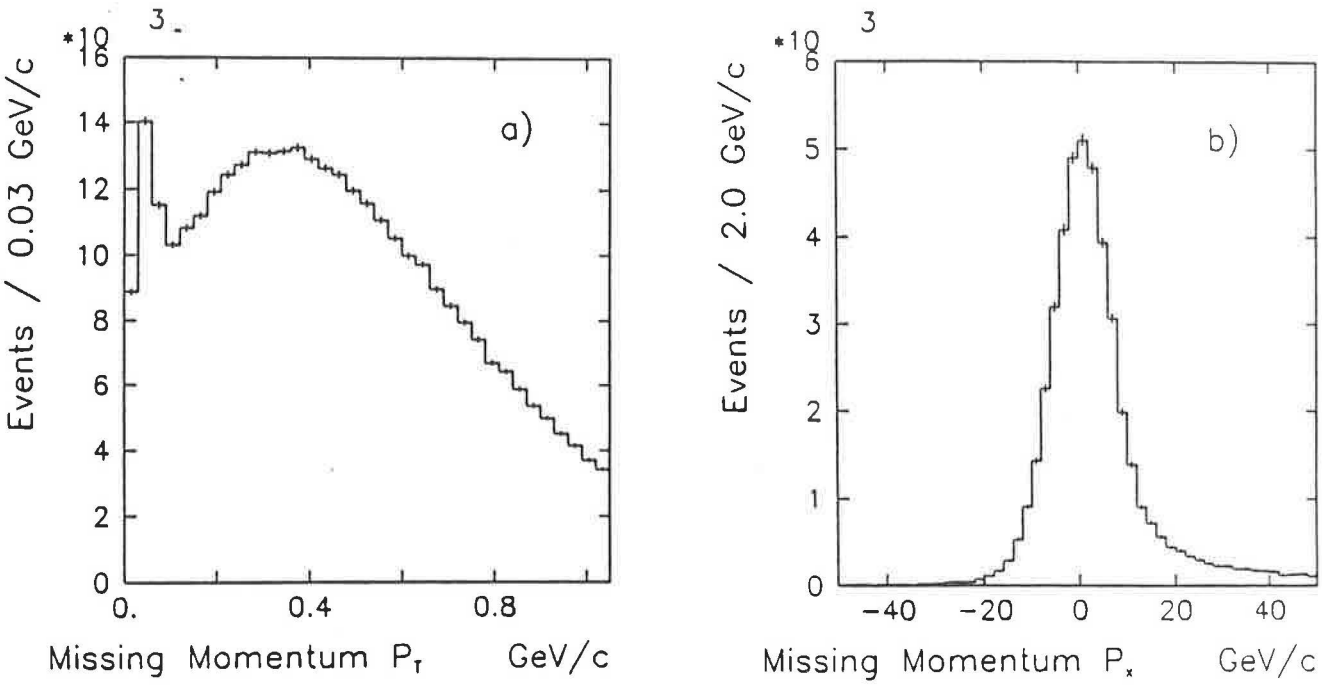

Figure 24: Missing momentum distributions for the four prong plus V^0 events.
a) Missing transverse momentum distribution
b) Missing longitudinal momentum distribution after a cut on the missing P_T

Fig. 24a shows the total missing P_T where a clear signal of candidate 4C events can be seen. Fig. 24b shows the resulting longitudinal missing momentum after placing a cut on the missing P_T, a clear peak can be seen which is centred at zero and there is very little background.

The momentum imbalance that results from these cuts is due mainly to the fast track. Therefore the fast track's momentum is recalculated to produce a completely momentum balanced system. The slow particle is identified as a slow proton by applying a cut to the pulse heights in the SPC and the TS as a function of momentum as described in chapter 3.

For this sample of 4C events the effective mass of the V^0 is calculated assuming that the two decay particles are pions. Fig. 25a shows the resulting mass spectrum for the V^0's from TRIDENT and fig. 25b for the V^0's from the VZERO program. The signal to background ratio S/B in the mass

region $0.47 < m(\pi^+\pi^-) < 0.52$ GeV/c². is 2.7 for the TRIDENT data and 0.5 for the VZERO data. The K^0's from the VZERO program have a much worse signal to background because as well as rescuing some of the V^0's missed by TRIDENT it also produces a lot of false V^0's.

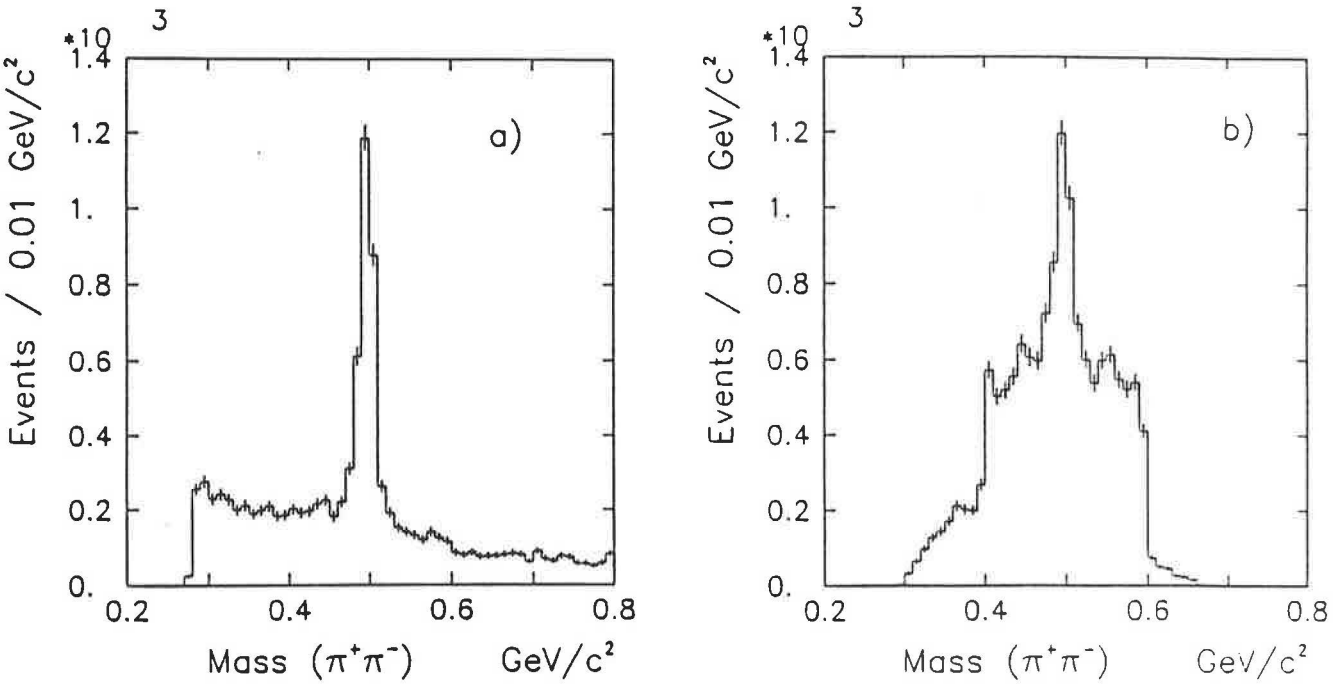

Figure 25: Effective mass spectrum for the V^0's, assuming two pions for, a) TRIDENT and b) VZERO data.

The following cuts have been applied to the V^0's from the VZERO program in order to remove the false V^0's and hence improve the signal to background in the K^0 region, while retaining as much of the K^0 signal as possible.

1. Reject all those VZERO events that have decay distances less than 5 cm.

2. Reject all the remaining VZERO data if the momentum angle, which is the angle between the vector defining the main vertex to the secondary vertex and the V^0 momentum vector, is greater than 1^0.

Although these cuts reduce the signal by a factor of 2 the signal to background is much improved. Fig. 26 shows the total $\pi^+\pi^-$ mass distribution after the cuts on the VZERO data. A good K^0 signal is seen. A fit to the mass spectrum (not shown) using a Gaussian and a linear background gives σ = 7 MeV/c^2. The K^0 is selected by requiring $0.475 < m(\pi^+\pi^-) < 0.52$ GeV/c^2.

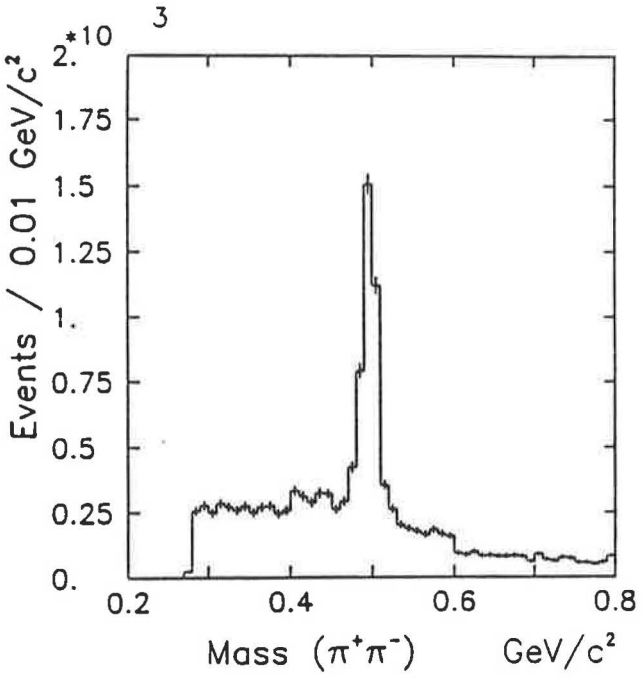

Figure 26: Effective mass distribution of the $\pi^+\pi^-$ pairs.

The reaction

$$pp \rightarrow p_f\,(K^0_S K^{\pm}\pi^{\mp})\,p_s$$

was then selected from those events that balance momentum and have a K^0 by using energy conservation. A cut was placed on the Δ function which is defined to be :−

$$\begin{aligned}\Delta &= MM^2(P_f P_s) - M^2(K\bar{K}\pi) \\ &= (E_{beam} + E_{target} - E_{slow} - E_{fast})^2 \\ &\quad - (P_{beam} + P_{target} - P_{slow} - P_{fast})^2 \\ &\quad - (E_{K^0} + E_+ - E_-)^2 \\ &\quad + (P_{K^0} + P_+ - P_-)^2\end{aligned}$$

of $|\Delta| \leq 1.6\ (GeV/c^2)^2$.

The Δ function was calculated twice for each event for the two hypotheses i.e. $K^+\pi^-$ and $K^-\pi^+$. The cut on the Δ function could give three possible results,

1. Neither combination passed the cut in which case the event was rejected.

2. Only one combination passed the cut in which case the Cerenkov information, if any, was required to be compatible with this combination.

3. Both combinations passed the cut in which case the Cerenkov information, if any was used to give the particles an unambiguous mass assignment.

The remaining events (28.8% of the total) had an ambiguous mass assignment.

In order to reduce the number of ambiguous events the Ehrlich mass [86] has been calculated for the V^0 and one of the charged particles assuming the other to be a pion. The mass is given by

$$m^2_{\pm} = \frac{(B^2 - (2P_{V^0}P_{\pm})^2)}{4(P_{V^0}{}^2 + P_{\pm}{}^2 + B)}$$

where

$$B = (E_{target} + E_{beam} - E_{fast} - E_{slow} - E_{\mp})^2 - (P_{V^0}{}^2 + P_{\pm}{}^2)\,.$$

The mass is calculated twice for each ambiguous event and is shown in fig. 27. A clear peak can be seen at the kaon mass squared which is the signature of the $K^0K^{\pm}$ channel. A cut was placed on the Ehrlich mass to define each combination as $K^0K^{\pm}$ or $K^0\pi^{\pm}$. An unambiguous mass assignment was given to those events which had only one mass combination in the kaon mass squared region. If both combinations had a mass squared less than 0.1 $(GeV/c^2)^2$, the events was assumed to be a 4π

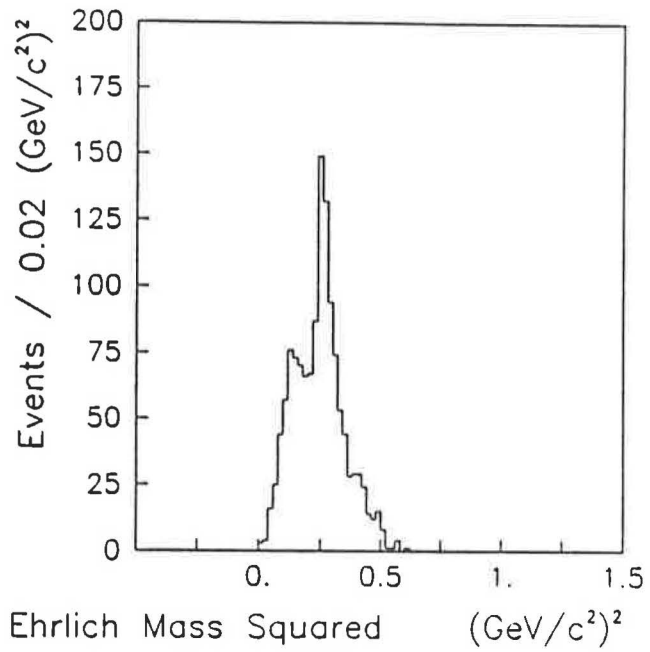

Figure 27: The Ehrlich mass squared for $V^0a^{\pm}$ with $b^{\mp}$ having the mass of a π.

event where 2π's had been misidentified as coming from a V^0 and the event was rejected. If both mass combinations fell in the $K^0K^{\pm}$ region (6.8 % of the total) both combinations were used in the following analysis.

5.3 The $K^0_SK^{\pm}\pi^{\mp}$ mass spectrum

Fig. 28 shows the $K^0_SK^{\pm}\pi^{\mp}$ effective mass spectrum (3808 events) where the events that have an ambiguous $K^{\pm}\pi^{\mp}$ mass assignment are plotted twice (6.8 % of the events). A fit to this spectrum using two Breit-Wigners and a background of the form $a(m-m_{th})^b\exp(-cm-dm^2)$ (where m is the $K^0_SK^{\pm}\pi^{\mp}$ mass, m_{th} is the $K^0_SK^{\pm}\pi^{\mp}$ threshold mass and a,b,c,d are fit parameters), yields masses

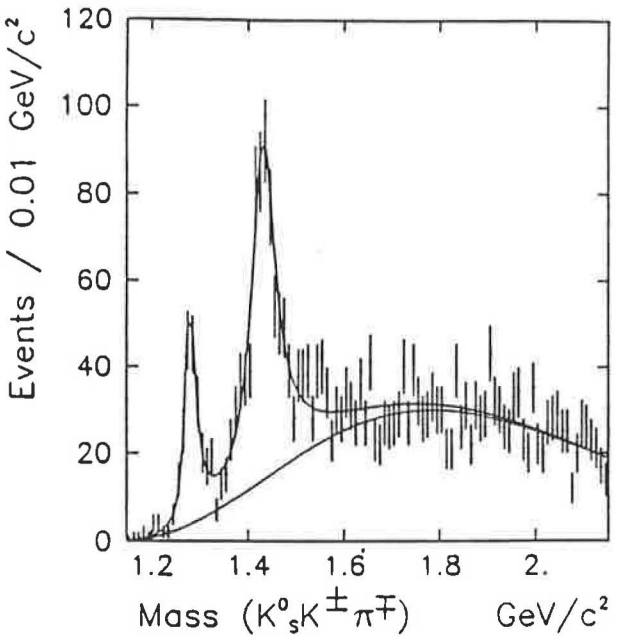

Figure 28: $K^0_S K^{\pm}\pi^{\mp}$ mass spectrum. The superimposed curve is the result of the fit described in the text.

and widths of[3]

$$M_1 = 1278 \pm 2 \text{ MeV/c}^2 \quad \Gamma_1 = 25 \pm 4 \text{ MeV/c}^2$$

$$M_2 = 1429 \pm 3 \text{ MeV/c}^2 \quad \Gamma_2 = 58 \pm 8 \text{ MeV/c}^2$$

In the 85 GeV/c data [31] a similar fit to the $K^0_S K^{\pm}\pi^{\mp}$ mass spectrum yielded :–

$$M_1 = 1279 \pm 2 \text{ MeV/c}^2 \quad \Gamma_1 = 32 \pm 3 \text{ MeV/c}^2$$

$$M_2 = 1425 \pm 2 \text{ MeV/c}^2 \quad \Gamma_2 = 62 \pm 5 \text{ MeV/c}^2,$$

and a spin–parity analysis of these resonances led them to be identified as the $f_1(1285)$ and the $f_1(1420)$.

---

[3] The errors on masses, widths and number of events in this thesis have been calculated using the "EQ" method which is described in appendix D.

5.4 Geometrical acceptance for the $K^0_S K^{\pm}\pi^{\mp}$ channel

In order to study the geometrical acceptance of the apparatus 20000 events consisting of a fast, a slow, two positive and two negative tracks have been generated using event mixing of real events coming from the 4π channel. Initially the four central particles were assumed to be π's. The effective mass of the $\pi^+\pi^-$ pairs was calculated and the event was only accepted if one pair had an effective mass compatible with being a K^0 i.e. $0.45 < m(\pi^+\pi^-) < 0.55$ GeV/c^2. For these events the two π's were combined to form a K^0, which was allowed to decay exponentially with its proper lifetime. The remaining two tracks were assigned the kaon mass and pion mass so as to form $K^0_S K^+\pi^-$ and $K^0_S K^-\pi^+$ systems.

Each event was rotated around the x axis (ϕ) and translated in the target, to produce for each event ten different values of ϕ and vertex position. Each track was traced through the apparatus and the trigger conditions were applied to the event to see whether or not it would have been accepted.

The acceptance as a function of the $K^0_S K^{\pm}\pi^{\mp}$ effective mass has been calculated and shows a smooth decrease with increasing mass. The acceptance has been fitted using a third order polynomial and is shown in fig. 29. The equivalent curve for the 85 GeV/c data is shown in fig. 30.

The geometrical acceptance of the apparatus has also been evaluated over the Dalitz plot of the $K^0_S K^{\pm}\pi^{\mp}$ system in the $f_1(1285)$ (1.25 to 1.32 GeV/c^2) and the $f_1(1420)$ (1.37 to 1.49 GeV/c^2) regions and is found to be flat in the two regions. Therefore there is no need to apply weights to the data when fitting the Dalitz plot in either the $f_1(1285)$ or $f_1(1420)$ regions.

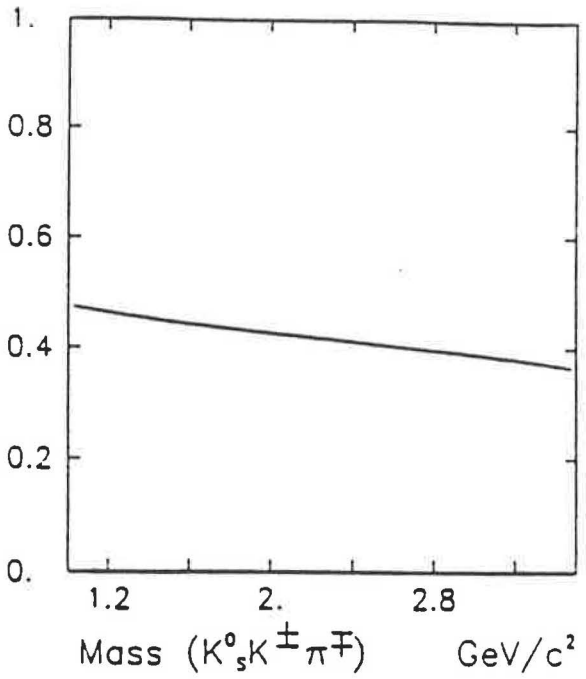

Figure 29: Geometrical acceptance as a function of $K\bar{K}\pi$ effective mass.

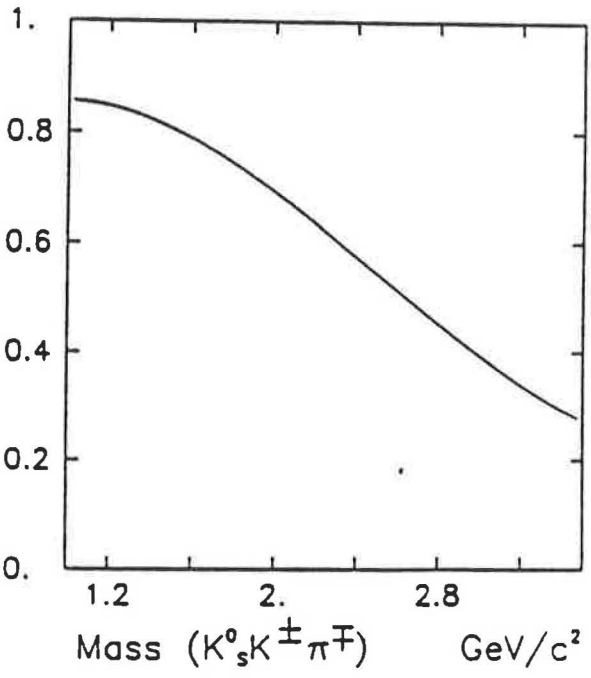

Figure 30: Geometrical acceptance as a function of $K\bar{K}\pi$ effective mass for the 85 GeV/c data.

6. SPIN PARITY ANALYSIS

6.1 Introduction

A full partial wave analysis of the central system that is formed in a two particle exchange process and has a three body decay has never been successfully done. The problem arises due to the unknown nature of the two exchanged particles. There have been several attempts where assumptions have been made about the spin of the exchanged particles but due to these assumptions the outcome of the analysis has led to a bias of certain waves. The only successful analysis used to date is a Dalitz plot analysis using the Zemach Formalism [87] where only the decay vertex is considered.

In this formalism the decay of a system X to three pseudoscalar particles a, b and c is assumed to proceed through an intermediate state of two particles, which then decays to give the observed three body final state.

$$X \rightarrow Y + c$$

$$Y \rightarrow a + b$$

This is known as the Standard Isobar model [88] in which the particle Y with spin S is represented by a traceless symmetric tensor of rank S constructed in momentum space.

Table 8 shows the matrix elements for these tensors up to spin 2, in terms of $p_\mu = a_\mu - b_\mu$ and $q_\mu = a_\mu + b_\mu$ where a_μ and b_μ are the energy-momentum four-vectors of particles a and b.

The spin-parity (J^P) of particle X is then constructed by calculating the coupling of particle c to Y in terms of the momentum of c ($\vec{p}$) and the angular momentum (L) between them. Table 9 gives an example of these constructions for spin 0 and 1, where $\vec{t}$ is the three vector part of $T^1{}_\mu(p,q)$ in the centre of mass of X.

To get the matrix element for the decay of X the tensors in table 9 have to be multiplied by the Breit-Wigner corresponding to the intermediate resonance Y. In the case where the intermediate resonance can be present in several charge states the total amplitude is the sum of the individual amplitudes multiplied by the appropriate Clebsch-Gordan coefficient of Isospin.

Table 8: Tensors describing an intermediate resonance of spin S

S	Four−momentum tensors	in cm of X	Tensors
0	$T^0(p,q)$	$=1$	1
1	$T^1{}_\mu(p,q)$	$=p_\mu - q_\mu(m^2{}_a - m^2{}_b/m^2{}_{ab})$	$\vec{t}$
2	$T^2{}_{\mu\nu}(p,q)$	$=p_\mu q_\nu - (1/3)(g_{\mu\nu} - q_\mu q_\nu/m^2{}_{ab})p^\rho p_\rho$	$t_i t_j - (1/3)\delta_{ij}\vec{\lvert t\rvert}^2$

Table 9: An example of the construction of the Tensors describing state X.

J^P	L	S	Tensor
0^-	0	0	scalar
0^-	1	1	$\vec{t}.\vec{p}$
1^+	0	1	$\vec{t}$
1^+	1	0	$\vec{p}$
1^+	2	1	$\vec{p}(\vec{t}.\vec{p}) - (\vec{p}.\vec{p})\vec{t}/3$

For the $K^0{}_S K^\pm \pi^\mp$ channel the state Y can either be a K^* or a $\delta(a_0(980))$ in which case c is either a K or π respectively. Since the K^* resonance can also occur as a $\bar{K}^*$ the final matrix element describing the decay into a $K^*\bar{K}$ plus charge conjugate system is :−

$$M = (1/\sqrt{6})(BW_1.M_1 + G.BW_2.M_2)$$

where BW_1 and BW_2 are the Breit-Wigner functions describing the K^* and $\bar{K}^*$ decays respectively, the

factor $(1/\sqrt{6})$ is a Clebsch Gordan coefficient[4] and G is related to the C parity of the parent particle by

$$C = (-1)^I G$$

i.e. the interference between the $K^*\bar{K}$ and $\bar{K}^*K$ is fixed by G Parity.

6.1.1 The Breit-Wigner used for the K^*'s

A relativistic Breit-Wigner [89] has been used to describe the K^* of the form,

$$BW(K^*) = \frac{\sqrt{(m\Gamma(q)/q)}}{m^2{}_0 - m^2 - im_0\Gamma(q)}$$

where

$$\Gamma(q) = \Gamma_0(q/q_0)^{2L+1}(2q_0{}^2/(q_0{}^2+q^2))$$

$$q_0 = \sqrt{(\Lambda(m_0{}^2, m_\pi{}^2, m_K{}^2)/(2m_0)}$$

$$q = \sqrt{(\Lambda(m^2, m_\pi{}^2, m_K{}^2)/(2m)}$$

$$\Lambda(a,b,c) = a^2 + b^2 + c^2 - 2ab - 2ac - 2bc$$

and $m_0 = m(K^*) = 0.8921$ GeV/c^2, $m = m(K\pi)$ and $\Gamma_0 = \Gamma(K^*) = 0.0513$ GeV/c^2.

6.1.2 The Breit-Wigner used for the δ

The Breit-Wigner for the decay of the δ is different due to the fact that it has two decay modes, $\eta\pi$ and $K\bar{K}$ and it is near threshold in the latter. This means that a coupled channel Breit-Wigner has to be used. The formalism used [90] is as follows :–

$$BW(\delta) = 0 \quad \text{Below } K\bar{K} \text{ threshold.}$$

$$BW(\delta) = \frac{m_0\sqrt{(\Gamma_1/\Gamma_2)}}{m_0{}^2 - m^2 - im_0(\Gamma_1+\Gamma_2)} \quad \text{above threshold}$$

where $m_0 = m(\delta)$, $\Gamma_1 = \Gamma(\eta\pi)$, $\Gamma_2 = \Gamma(K\bar{K})$ and $m = m(K\bar{K})$.

---

[4] The final state $K^0K^\pm\pi^\mp$ can proceed through a neutral or charged K^* state. Then the Clebsch Gordan coefficient is given by $(1/\sqrt{2})(|K^{*0}>|K^0> + |K^{*\pm}>|K^{\mp}>) = (1/\sqrt{6})(|K^*>|\bar{K}>)$

$\Gamma(\eta\pi) = g_\eta q_\eta$ and $\Gamma(K\bar{K}) = g_K\sqrt{(m^2/4 - m_K{}^2)}$, where $g_\eta(g_K)$ is the coupling constant squared for the resonance coupling to the $\pi\eta(K\bar{K})$ channels. q_η is the decay momentum of the mass m into a $\pi\eta$ system and is given by

$$q_\eta = \sqrt{(m^4 - (m_\eta + m_\pi)^4)}/(2m)$$

with $m(\delta) = 0.979$ GeV/c^2 and $\Gamma(\eta\pi) = 0.051$ GeV/c^2 [91] and the SU(3) prediction [92] of 2/3 has been used for the ratio g_η/g_K.

6.2 Decay matrix elements for the $K\bar{K}\pi$ channel.

Table 10: Decay matrix elements

J^P	L	Decay modes	Amplitudes
0^-	S	$\delta\pi$	Coup. Ch. $(\delta)^*$
	P	K^*K	$BW(K^*_{12})t_3 \cdot P_3 + G\,BW(K^*_{13})t_2 \cdot P_2$
1^-	S	K^*K	$BW(K^*_{12})t_3 + G\,BW(K^*_{13})t_2$
	P	$\delta\pi$	Coup. Ch. $(\delta)\,P_1$
	D	K^*K	$BW(K^*_{12})[P_3(t_3 \cdot P_3) - \frac{1}{3}(P_3 \cdot P_3)t_3] + G\,BW(K^*_{13})[P_2(t_2 \cdot P_2) - \frac{1}{3}(P_2 \cdot P_2)t_2]$
1^-	P	K^*K	$BW(K^*_{12})(t_3 \times P_3) + G\,BW(K^*_{13})(t_2 \times P_2)$
2^-	P	K^*K	$BW(K^*_{12})[\frac{1}{2}(t'_3 \cdot P^4_3 + P'_3 \cdot t^4_3) - \frac{1}{3}(t_3 \cdot P_3)\delta'']$ $+ G\,BW(K^*_{13})[\frac{1}{2}(t'_2 \cdot P^4_2 + P'_2 \cdot t^4_2) - \frac{1}{3}(t_2 \cdot P_2)\delta'']$
	D	$\delta\pi$	Coup. Ch. $(\delta)[P'_1 P^4_1 - \frac{1}{3}\lvert P_1\rvert^2\delta'']$
2^+	D	K^*K	$BW(K^*_{12})(\frac{1}{2}[(t_3 \times P_3)' P^4_3 + P^4_3(t_3 \times P_3)'] - \frac{1}{3}[(t_3 \times P_3) \cdot P_3]\delta'')$ $+ G\,BW(K^*_{13})(\frac{1}{2}[(t_2 \times P_2)' P^4_2 + P^4_2(t_2 \times P_2)'] - \frac{1}{3}[(t_2 \times P_2) \cdot P_2]\delta'')$

Amplitudes

$E \to \pi^+_1 K^-_2 K^0_3$,

t_i is the vector part (in E c.m.) of

$$P^\mu_i - P^\mu_k - \left[\frac{m_i^2 - m_k^2}{m^2_{jk}}\right]\left[P^\mu_j + P^\mu_k\right]$$

P_i $(i = 1, 2, 3)$ are the vector parts of the three decaying particle 4-momenta in the E c.m. system

$G = \pm 1$

*Coup. Ch(δ): coupled channel amplitude of the δ meson

In a Dalitz plot analysis of the $K^0_S K^{\pm}\pi^{\mp}$ channel either $K^*\bar{K}$ and $\bar{K}^*K$ or $K^*_{ch}K$ and $K^*_{ne}K$ can be used to describe the intermediate state. G parity eigenstates have a Dalitz plot population which is symmetric in all $K\pi$ combinations (appendix E). Therefore the G parity of the decaying state can be found whichever combination is used.

Different $K^*_{ch}K$ and $K^*_{ne}K$ production is expected from background events, therefore incoherent K^*K production shows up as an asymmetry between the K^*_{ch} and K^*_{ne} projections of the Dalitz plot. However this method does not allow the interference term between two different G parity states to be seen but if the individual states are correctly normalised this does not stop the two states being identified separately.

The relative merits of each combination are discussed in appendix E. In this analysis the $K^*_{ch}K$ and $K^*_{ne}K$ combination has been used due to the fact that this allows better signal to background separation but for completeness the method has been repeated in the $f_1(1420)$ region using $K^*\bar{K}$ and $\bar{K}^*K$. The decay matrix elements for a resonance X to decay to $K^*_{ch}K + K^*_{ne}K$ or $\delta\pi$ are given in table 10.

An element of phase space for a three body decay is

$$d\phi_3 = (1/32\pi^3)\, dE_2 dE_3$$

Therefore in the E_2E_3 plane, i.e. on a Dalitz plot of S_{13} versus S_{12}, the density of phase space is constant. The density of points on the Dalitz plot will be given by

$$D = |M|^2$$

However these densities are not normalised to one another and although this is not a problem if there is only one wave, if two or more waves need to be superimposed a correct normalisation between them is required.

In order to normalise all the waves it is necessary to compute the integrals of each wave in the total Lorentz invariant phase space. These integrals are mass dependent and have been calculated over the mass range 1.2 to 1.76 GeV/c^2 in steps of 0.01 GeV/c^2.

The integrals are calculated using FOWL [93], which is a program which uses the Monte Carlo method to calculate phase space distributions arising from particle interactions. The total centre-of-mass energy is given as input to FOWL which calculates the four-momenta of the three outgoing particles, together with a weight which is related to the phase space distributions. These four-momenta are then used as input to the Zemach amplitudes so as to generate the matrix elements squared for the waves in question. These waves are then weighted by the FOWL weight and are summed. The normalisation integral for each wave is then given by :−

$$\text{Norm Int(wave)} = \frac{\Sigma.\,\text{WT(FOWL)}\;|\text{M(wave)}|^2}{\Sigma\text{WT(FOWL)}}$$

Waves of the same spin-parity decaying to $K^*_{ch}K + K^*_{ne}K$ and $\delta\pi$ can interfere. The normalisation of these waves is explained in the following section.

6.2.1 Normalisation of interference terms

Consider two complex amplitudes A and B which are normalised by

$$\int |A|^2\, d^4E = \int |B|^2\, d^4E = 1$$

If the two amplitudes are present such that the observed intensity is given by :−

$$|A + e^{i\phi}B|^2 = |A|^2 + |B|^2 + 2\cos\phi\,\text{Re}(AB^*) + 2\sin\phi\,\text{Im}(AB^*)$$

then the normalised intensity is

$$|(A/x) + e^{i\phi}(B/y)|^2$$

$$= (|A|^2/x^2) + (|B|^2/y^2) + 2\cos\phi(\text{Re}(AB^*)/xy) + 2\sin\phi(\text{Im}(AB^*)/xy)$$

where

$$x^2 = \int|A|^2d^4E \quad \text{and} \quad y^2 = \int|B|^2d^4E$$

The total set of waves for which normalisation integrals have been calculated are given in table 11.

Table 11: Complete set of waves used

0^-+ S	$\delta\pi$	0^-+ P	K^*K
0^-+	Re(SP)	0^-+	Im(SP)
1^++ P	$\delta\pi$	1^++ S	K^*K
1^++	Re(SP)	1^++	Im(SP)
1^++ D	K^*K		
1^++	Re(SD)	1^++	Im(SD)
1^++	Re(PD)	1^++	Im(PD)
1^-+ P	K^*K		
2^-+ D	$\delta\pi$	2^-+ P	K^*K
2^-+	Re(PD)	2^-+	Im(PD)
2^++ D	K^*K		
1^+- S	K^*K		
1^++1^+-	Real(int)	1^++1^+-	Im(int)

6.3 Fit to the Dalitz plot using a maximum likelihood function

Often in experiments an observation is made of a quantity "x" which is related to some parameter "a" by a probability distribution P(a,x). From this distribution the quantity

$$L(a) = \Pi\, P(a,x_i)$$

is formed where the x_i's are the events observed in an experiment. The likelihood method consists of choosing the best estimate of "a" so as to maximise L(a) [94] (see appendix D).

In this case the x_i's are the Zemach amplitudes, as calculated from the observed particle four-momenta, and "a" is the amount of each amplitude. The overall probability to be fitted is of the form :–

$$P = \Sigma\alpha_i|A^{JP}{}_G|^2 + (1 - \Sigma\alpha)$$

The log likelihood, which is given by :–

$$Ln(L(a)) = \Sigma Ln(P(a,x_i)),$$

is calculated and the negative log likelihood is minimised using MINUIT [95] to give the amount of each wave required in the fit.

The physical events are read in, the waves are computed and are normalised using the normalisation integrals. The negative log likelihood function is calculated for the waves being considered and is minimised to give the fractions of each wave. A fit using all 22 waves simultaneously is impractical. Therefore a fit has to be made in an iterative manner using sets of waves.

6.3.1 A fit to the $f_1(1285)$ region

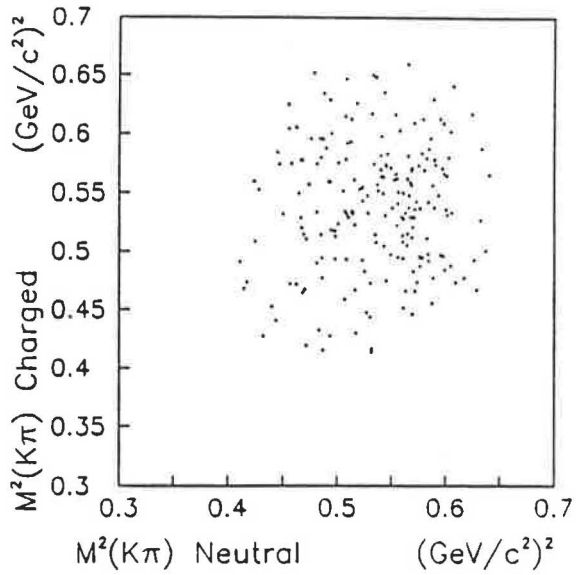

Figure 31: Dalitz plot for the mass region $1.25-1.32$ GeV/c^2.

Fig. 31 shows the Dalitz plot for the $f_1(1285)$ region, defined as $1.25 \leq M(K^0_S K^{\pm}\pi^{\mp}) \leq 1.32$ GeV/c^2, which has 200 entries. The $f_1(1285)$ region is the simplest as the only isobar available is the δ because this region is below $K^*\overline{K}$ threshold. The only states that are possible for the object at 1280 MeV/c^2 are :–

$$0^{-+}\ S,\ 1^{++}\ P \text{ and } 2^{-+}\ D$$

The three waves were initially fitted separately using a probability function defined as :−

$$P = (x|M|^2)/(\int|M|^2) + (1-x)$$

where $(1-x)$ represents the background. The fits show that the best solution is for 70 ± 6 % 1^{++} $\delta\pi$ with 30 % phase space background. Introducing a 0^{-+} wave in addition to the 1^{++} wave does not improve the log likelihood of the fit significantly.

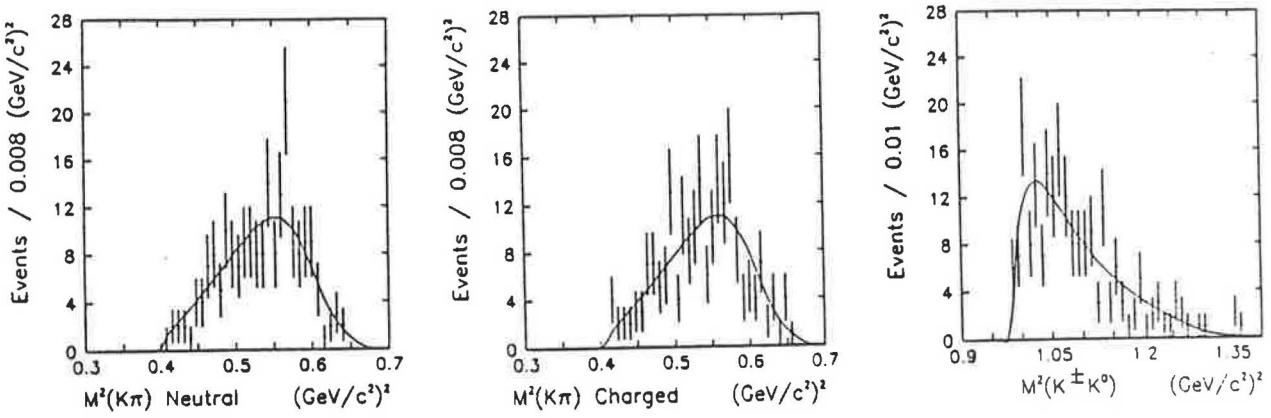

Figure 32: Dalitz plot projections for the mass region 1.25 − 1.32 GeV/c² with fit using 70% 1^{++} P wave.

The results of the fit have been given as input to a Monte Carlo FOWL program which computes the Dalitz plot density for 70% 1^{++} $\delta\pi$ with a 30% background. The results of this simulation are superimposed on the Dalitz plot projections in fig. 32 and shows good agreement.

Therefore we conclude that we are observing the $f_1(1285)$ and that no other wave is required. This agrees with the results obtained at 85 GeV/c [31].

6.3.2 A fit to the $f_1(1420)$ region

The $f_1(1420)$ region is more complicated than the $f_1(1285)$ region as not only can the decay proceed through either the $K^*\bar{K}$ or $\delta\pi$ channels but interference can also occur between the two decay modes.

Fig. 33 shows the Dalitz plot, with projections, in the $f_1(1420)$ region defined as $1.37 \leq M(K^0_S K^{\pm}\pi^{\mp}) \leq 1.49$ GeV/c². There are 671 events in the plot and well defined K^* bands can be seen. The K^* bands are equally populated which implies that very little incoherent K^* production is occurring. Therefore incoherent K^* waves have been excluded from the fit.

It is interesting to compare the experimental Dalitz plot with those generated by Monte Carlo for pure J^{PC} waves which are shown in fig. 34. The Dalitz plot for the data from the $f_1(1420)$ region, shown in fig. 33, is similar to the 1^{++} $K^*\bar{K}$ wave shown in fig. 34d.

The $f_1(1420)$ region has been fitted in 40 MeV/c² slices from 1.33 to 1.69 GeV/c² so that the behaviour of the resonance and the background can be studied. Full interference between waves having the same spin-parity has been allowed. Interference was also allowed between the 1^{++} and 1^{+-} $K^*\bar{K}$ waves.

The fit shows that the $1^{++}(K^*\bar{K})$ is the dominant wave. The addition of 0^{-+} or any other waves up to J equals 2 does not increase the log likelihood within the errors. A fit including 0^{-+} and 1^{++} S waves is shown in fig. 35. If the $f_1(1420)$ region is defined as $1.37 \leq M(K^0_S K^{\pm}\pi^{\mp}) \leq 1.49$ GeV/c² then the percentage of each wave present is

0^{-+}	(3 ± 2) %
1^{++} S	(56 ± 4) %

Therefore it is concluded that the 0^{-+} waves are consistent with zero and only the 1^{++} wave is needed. A fit with 1^{++} and phase space only gives

1^{++} S	(58 ± 4) %

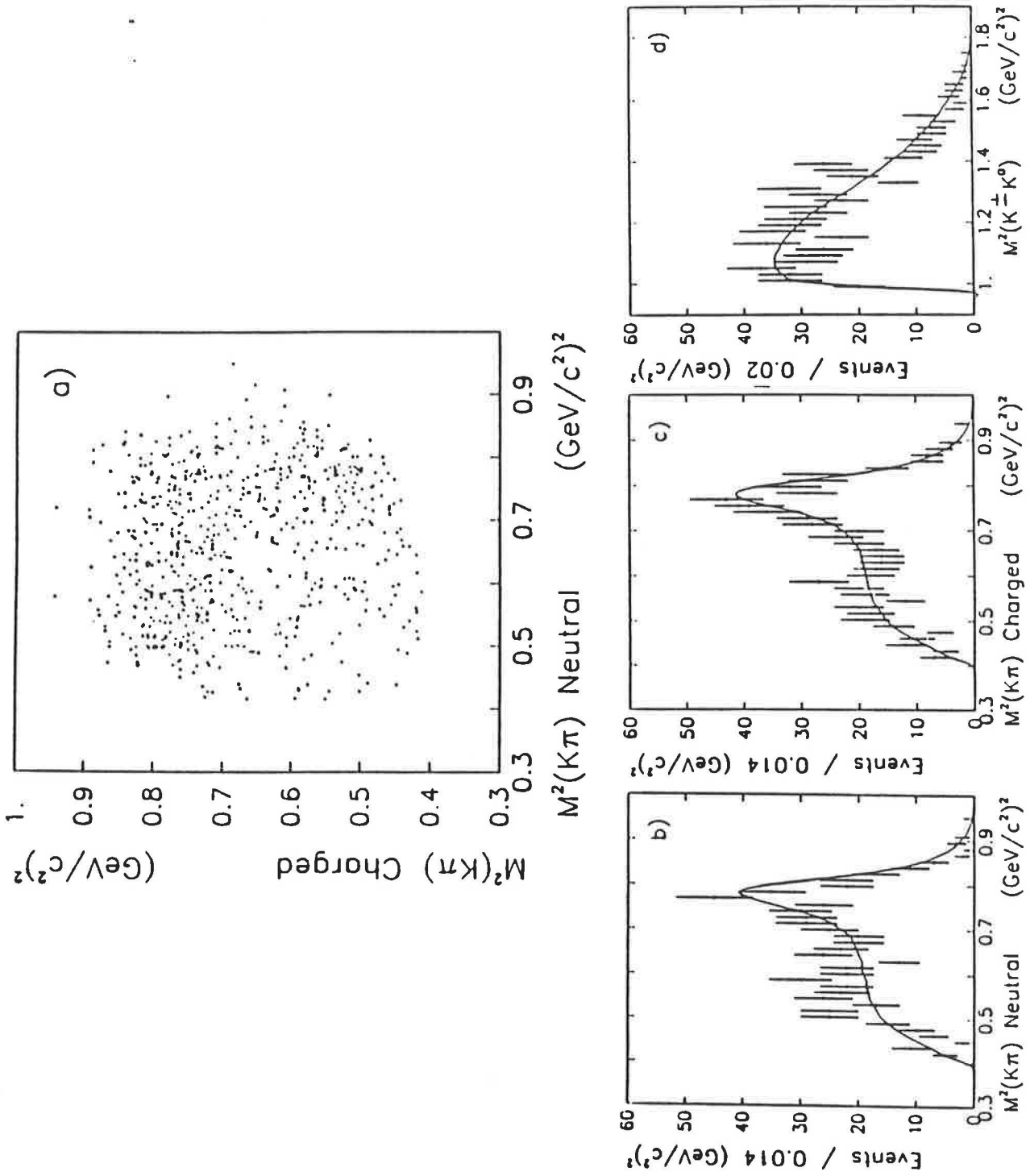

Figure 33: a) Dalitz plot with b),c) $K\pi$ and d)$K\bar{K}$ projections for the mass region $1.37-1.49$ GeV. The superimposed curve corresponds to the Monte Carlo simulation using 58 % 1^{++} S wave.

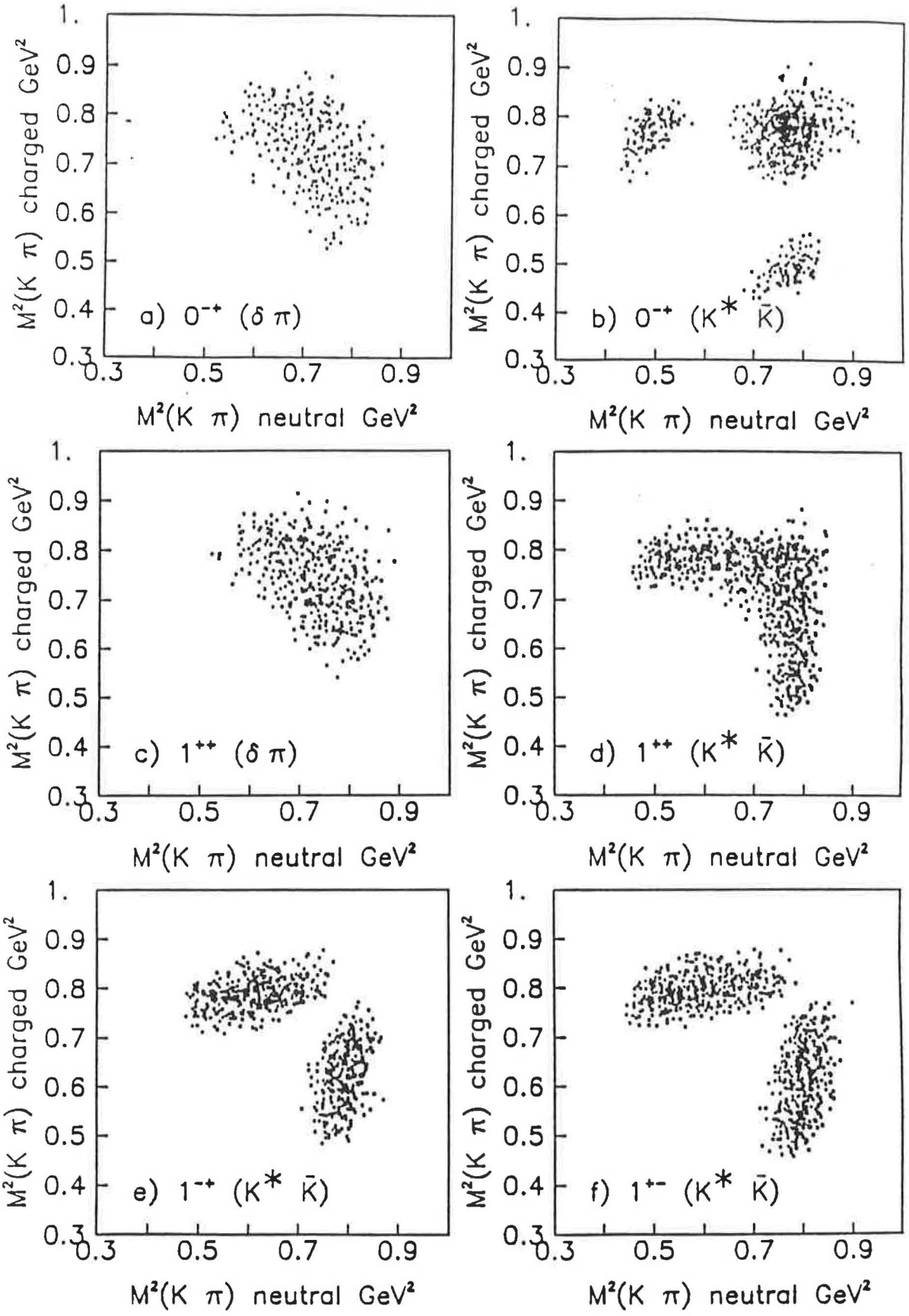

Figure 34: Monte Carlo Dalitz plot's for the mass region 1.37 – 1.49 GeV/c².

with 42 % background which is consistent with a fit to the total mass spectrum. The result of a Monte Carlo simulation based on the results of this fit is shown superimposed on the Dalitz plot projections in fig. 33 and shows good agreement.

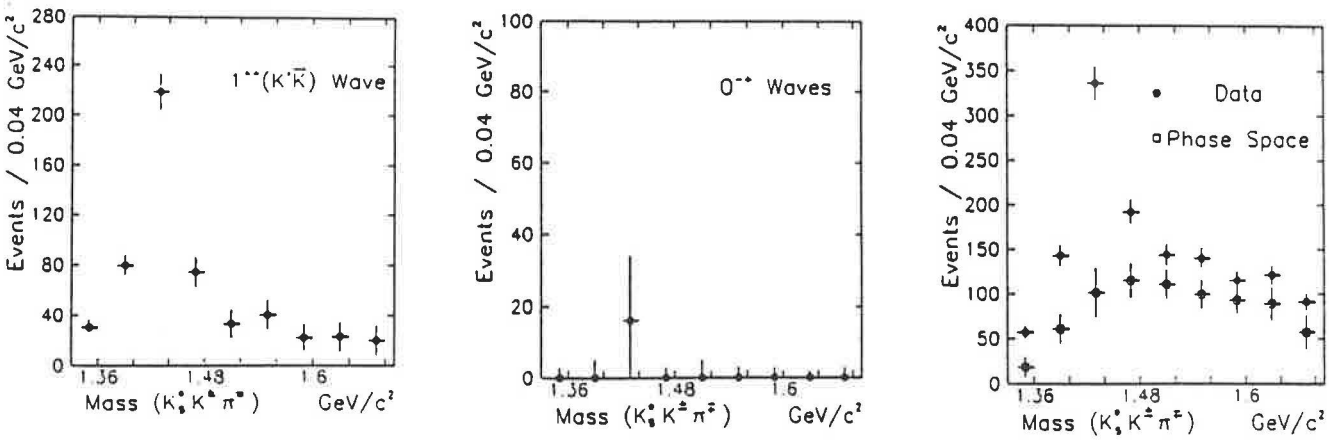

Figure 35: Result of the Dalitz plot analysis.

Therefore the data can be well described by using only a 1^{++} S ($K^*\bar{K}$) wave and we conclude that we are observing the $f_1(1420)$ and no other wave is required.

An investigation of the stability of the fit with changes in the parameterisation of the coupled channel decay of the δ has been carried out. The partial decay width of the δ to $\eta\pi$ has been varied between 30 and 80 MeV/c² and the ratio of g_K/g_η has been changed between 1.0 and 2.0. The outcome of the fit, determined by the amount of each wave required, appears to be stable within these limits.

The fits have been repeated on the acceptance corrected data. The conclusion that only the 1^{++} wave is required remains unchanged.

The fits have been repeated using a Dalitz plot analysis where the combinations are plotted according to their strangeness rather than their charge. The best fit is again found to be for 58 % 1^{++} $K^*\bar{K}$ with no other wave required. The K^* versus $\bar{K}^*$ Dalitz plot is shown in fig. 36 with projections. The result of a Monte Carlo simulation based on the results of the fit is shown superimposed on the Dalitz plot projections and shows good agreement.

6.4 Comparison of the 85 and 300 GeV/c $K^0_S K^{\pm}\pi^{\mp}$ channels

In the $K^0_S K^{\pm}\pi^{\mp}$ channel at 85 [31] and 300 GeV/c a spin-parity analysis has determined that the two states observed are the $f_1(1285)$ decaying to $\delta\pi$ and the $f_1(1420)$ decaying to $K^*\bar{K}$.

In order to compare the reaction $pp \rightarrow p_f (K^0_S K^{\pm}\pi^{\mp}) p_s$ at the two energies, a cut has been placed on the Feynman x of the $K^0_S K^{\pm}\pi^{\mp}$ system to select a region for which the acceptance is good for both experiments. The cut used is $|x_F| \leq 0.15$. The $K^0_S K^{\pm}\pi^{\mp}$ mass distributions have been corrected for geometrical acceptance as shown in figs. 37 and 38 for the 85 and 300 GeV/c data respectively. The method used to calculate the errors is given in appendix D.

The two spectra have been added together and fitted using two Breit-Wigners and the background described above. The masses and widths of the two resonances are determined by the fit and are given in table 12. The 85 and 300 GeV/c data have then been fitted separately using these parameters and the number of events belonging to the $f_1(1285)$ and the $f_1(1420)$ resonances have been determined from the fit. The results are given in table 12.

The ratio (R) of the number of $f_1(1285)$ events to the number of $f_1(1420)$ events has been calculated for the two sets of data,

$$\text{at } 85 \text{ GeV/c} \quad R = 0.58 \pm 0.07$$

$$\text{at } 300 \text{ GeV/c} \quad R = 0.34 \pm 0.03$$

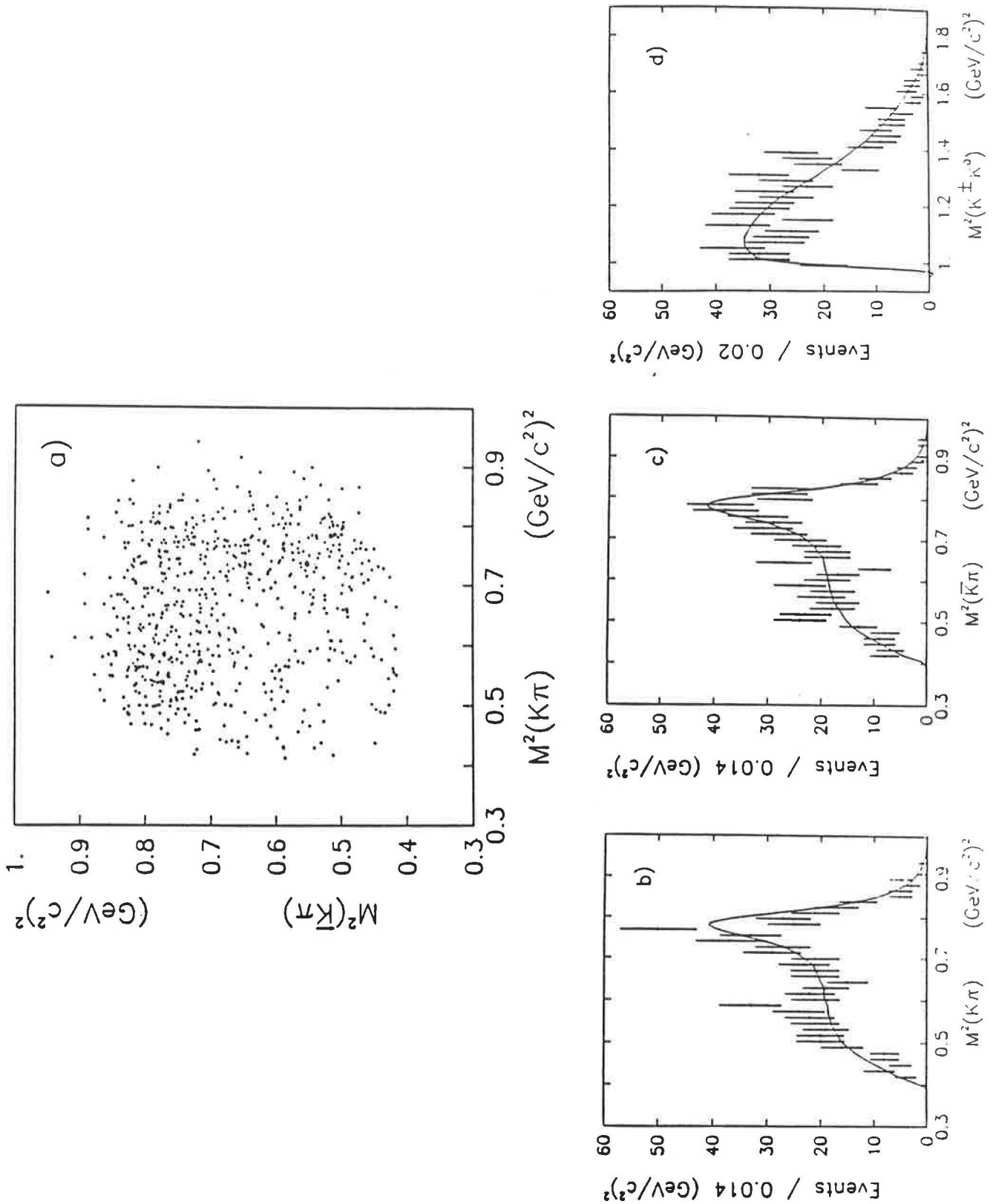

Figure 36: a) Dalitz plot with b),c) $K\pi$ and d)$K\bar{K}$ projections for the mass region 1.37 – 1.49 GeV. The superimposed curve corresponds to the Monte Carlo simulation using 58 % 1^{++} S wave.

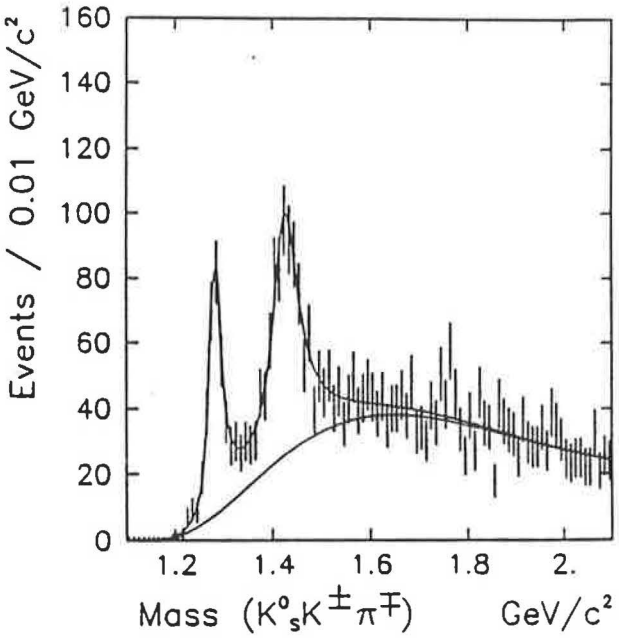

Figure 37: $K^0_S K^{\pm}\pi^{\mp}$ acceptance corrected mass distributions for the 85 GeV/c data, with fit .

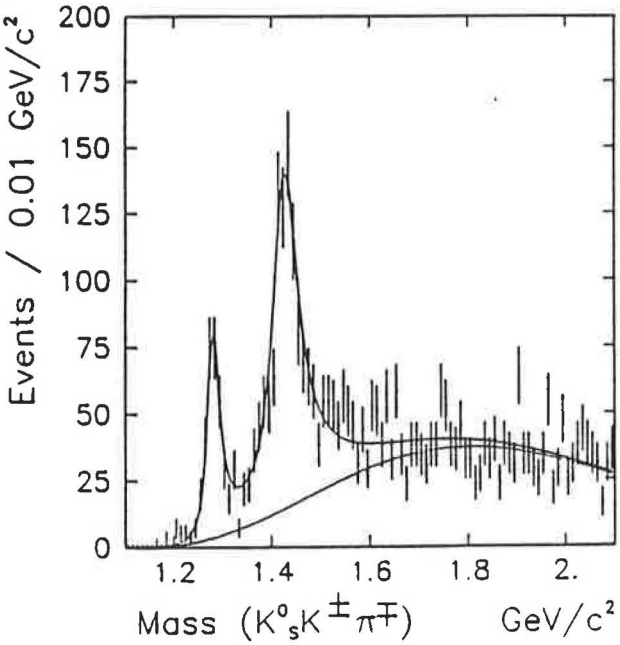

Figure 38: $K^0_S K^{\pm}\pi^{\mp}$ acceptance corrected mass distributions for the 300 GeV/c data, with fit .

This suggests that the energy dependence of the $f_1(1285)$ production is different from that of the $f_1(1420)$.

In order to investigate the energy dependence of the $f_1(1285)$ and the $f_1(1420)$ individually the cross sections are calculated in the following section.

Table 12: Masses, widths and number of events from a fit to the acceptance corrected $K^0_S K^{\pm}\pi^{\mp}$ spectra.

	Mass MeV/c^2	Width MeV/c^2
For the combined data		
$f_1(1285)$	1280 ± 2	28 ± 4
$f_1(1420)$	1426 ± 2	62 ± 8
	Number of events	
	85GeV/c	300GeV/c
$f_1(1285)$	375 ± 29	389 ± 36
$f_1(1420)$	645 ± 59	1156 ± 58

6.5 Cross sections

In order to calculate the cross sections for the $f_1(1285)$ and $f_1(1420)$, in addition to the losses due to the geometrical acceptance corrected for in the previous section, the losses due to the slow proton, selection cuts, detector efficiencies etc. have to be calculated.

The losses that have been considered are given below and the numerical values are given in table 13.

1. Losses due to the cuts on the components of missing momentum, Delta function and Ehrlich mass.

2. The slow proton geometrical acceptance, which is constant as a function of the $K^0_S K^{\pm}\pi^{\mp}$ effective mass.

3. Losses due to the slow protons being absorbed in the target. This loss shows up as a depletion of events near zero in the four-momentum transferred at the slow vertex.

4. The efficiency of the slow proton detector and the A_1 and A_2 scintillation counters.

5. Losses due to inefficiencies in the reconstruction program. This loss can be calculated by scanning events.

6. Losses due to charged kaon decay resulting in an unambiguously identified event from the Δ function being rejected by Cerenkov information.

7. Corrections due to the K^0 branching ratio and unseen decay modes.

After taking into account these losses and using the number of $f_1(1285)$ and $f_1(1420)$ events calculated in the last section, the cross sections are found to be

$$85\ \text{GeV/c} : \sigma(f_1(1285)) = 230 \pm 70\ \text{nb} \quad \sigma(f_1(1420)) = 400 \pm 125\ \text{nb}$$

$$300\ \text{GeV/c} : \sigma(f_1(1285)) = 135 \pm 40\ \text{nb} \quad \sigma(f_1(1420)) = 400 \pm 110\ \text{nb}$$

These results indicate that the $f_1(1285)$ cross section decreases with incident momentum while the $f_1(1420)$ cross section remains constant.

Table 13: Correction factors

	85 GeV/c	300GeV/c
Selection Cuts	1.9	1.8
Slow proton Geometrical acceptance and low t losses	8.6 1.4	8.6 1.7
Detector inefficiencies	1.4	1.25
Reconstruction program	1.25	1.25
$K^{\pm}$ decay	1.1	1.15
$K^0_S \to \pi^+\pi^-$	1.46	1.46
$K^0 \to K^0_S$ or K^0_L	2.0	2.0
Sensitivity events/nb	208	400

6.6 Conclusions

Clear $f_1(1285)$ and $f_1(1420)$ signals are seen in the $K^0_S K^{\pm}\pi^{\mp}$ channel with masses and widths

$$f_1(1285) \quad m = 1278 \pm 2 \text{ MeV/c}^2 \quad \Gamma = 25 \pm 4 \text{ MeV/c}^2,$$

$$f_1(1420) \quad m = 1429 \pm 3 \text{ MeV/c}^2 \quad \Gamma = 58 \pm 8 \text{ MeV/c}^2.$$

A spin-parity analysis shows that both are 1^{++} states. The $f_1(1285)$ is found to decay via $\delta\pi$ while the $f_1(1420)$ is found to decay only to $K^*\bar{K}$, no 0^{-+} wave being required to describe the data. The energy dependence for the production of the $f_1(1285)$ is not the same as that for the $f_1(1420)$ and it is found that the cross section for the $f_1(1420)$ remains constant as a function of incident momentum.

7. THE $K^+K^-K^+K^-$ CHANNEL IN WA76′

7.1 Introduction

As was discussed in chapter 2, the $\phi\phi$ channel is of interest due to the claimed observation of three $J^{PC} = 2^{++}$ states [57]. One or more of these states could be a glueball. This chapter describes an analysis of the $\phi\phi$ channel observed in experiment WA76 at 300 GeV/c.

7.2 Selection of the channel $K^+K^-K^+K^-$

Events corresponding to the reaction

$$pp \rightarrow p_f (K^+K^-K^+K^-) p_s$$

were selected from charge balancing six-prong events, using the momentum cuts |Missing P_x| < 20.0 GeV/c, |Missing P_y| < 0.16 GeV/c and |Missing P_z| < 0.06 GeV/c, where the x-axis is along the beam direction.

Information from the Cerenkov counters was used to ensure that at least one of the centrally produced particles was a kaon or ambiguous kaon/proton and that none of the centrally produced particles was a positively identified pion. A pulse-height momentum correlation in a system of scintillation counters was used to ensure that the slow particle was a proton.

The method of Ehrlich et al. [86], modified for four tracks, has been used to compute the mass squared of the four central particles (assumed to be equal). The resulting distribution is shown in fig. 39, fitted with an exponential and a Gaussian, where a signal of the four kaon channel can be seen at 0.24 $(GeV/c^2)^2$. A cut on the mass squared of

$$0.18 < M^2 < 0.32 \ (GeV/c^2)^2$$

has been used to select a sample of 4K events.

The four possible K^+K^- mass combinations are plotted in fig. 40, where a clear ϕ signal can be seen. A fit has been performed to this spectrum where the ϕ is represented by a Breit-Wigner convoluted with a Gaussian to represent the experimental resolution, and a background of the form

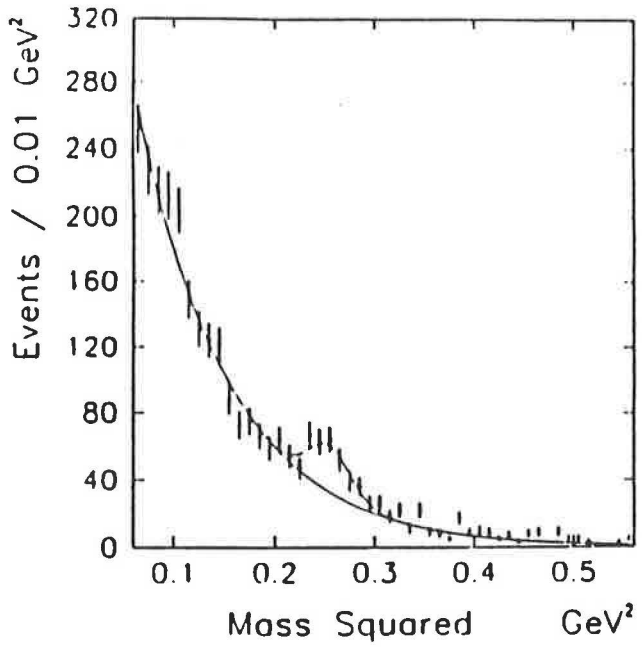

Figure 39: The Ehrlich mass squared distribution for the four charged particles.

$$a(m-m_{th})^b \exp(-cm-dm^2)$$

where m is the K^+K^- mass, m_{th} is the threshold mass and a,b,c and d are fit parameters. This gave the following results

$$m(\phi) = 1019.1 \pm 0.8 \text{ MeV/c}^2$$

$$\sigma(\text{Gaussian}) = 3.3 \pm 0.5 \text{ MeV/c}^2$$

$$\Gamma(\text{Breit-Wigner}) = 4.22 \text{ MeV/c}^2 \text{ (fixed)}$$

The Feynman x_F distribution is shown in fig. 41 for the ϕK^+K^- system, where the central events lie within $|x_F| < 0.2$.

Fig. 42 shows the K^+K^- vs K^+K^- lego plot, which indicates strong $\phi\phi$ production. By selecting one K^+K^- mass to lie within a band around the ϕ mass (from 1.008-1.030 GeV/c²) and plotting the effective mass of the other pair, the spectrum of fig. 43 was produced. The large ϕ signal with little background confirms the presence of a strong $\phi\phi$ signal.

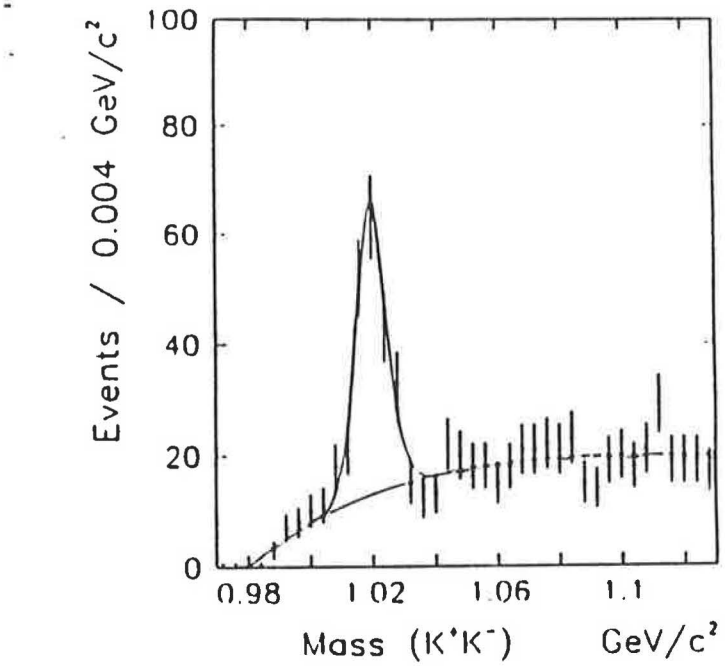

Figure 40: The K^+K^- mass spectrum (four combinations per event) The curve shows the result of a fit using a convoluted Breit-Wigner and Gaussian with a background described in the text.

The number of events in nine regions around the $\phi\phi$ position in the K^+K^- scatter plot are shown in fig. 44; no event has more than one entry in this region. From these numbers and applying a correction for the tails of the ϕ, the total number of $\phi\phi$ events is found to be 39 ± 8.

The $\phi\phi$ effective mass spectrum is shown in fig. 45 for the events in the central bin of fig. 44, and shows an accumulation near threshold similar to that observed at 85 GeV/c [96]. The combined spectrum for 85 and 300 GeV/c is shown in fig. 46. The curve indicates the shape of the $\phi\phi$ mass spectrum observed in the reaction

$$\pi^- p \rightarrow \phi\phi n \qquad (1)$$

at 22 GeV/c [57], which consists of three 2^{++} states. The $\phi\phi$ mass distribution observed in central production is similar.

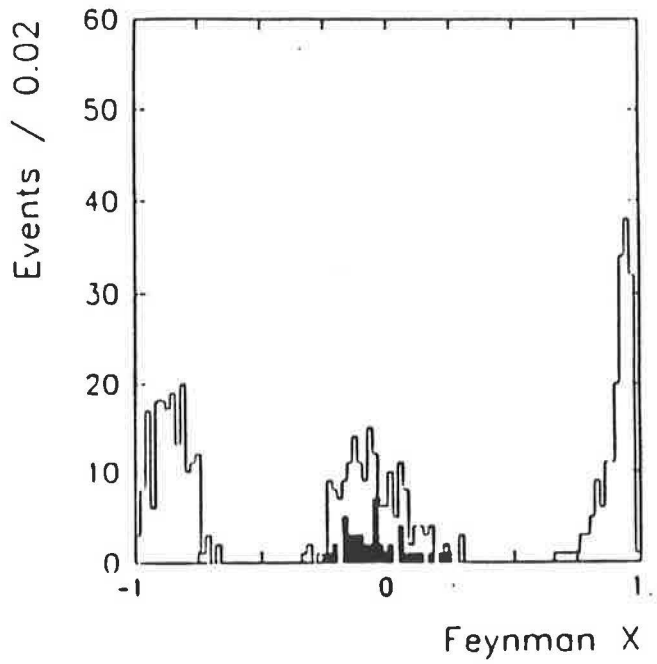

Figure 41: x_F distribution for the ϕK^+K^- system, and the fast and slow particles. The shaded histogram represents the $\phi\phi$ system.

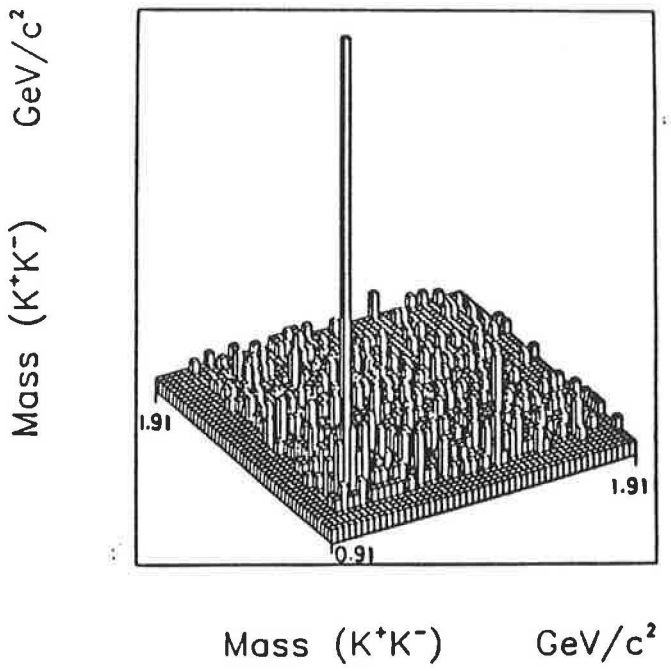

Figure 42: Lego Plot of one K^+K^- mass against the other (two entries per event).

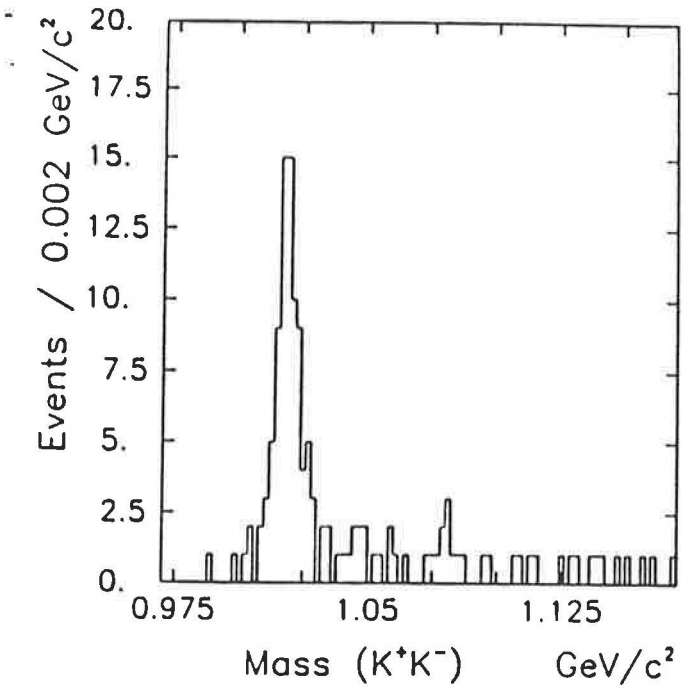

Figure 43: K^+K^- effective mass of one K^+K^- combination after selecting the other to lie in the ϕ mass band.

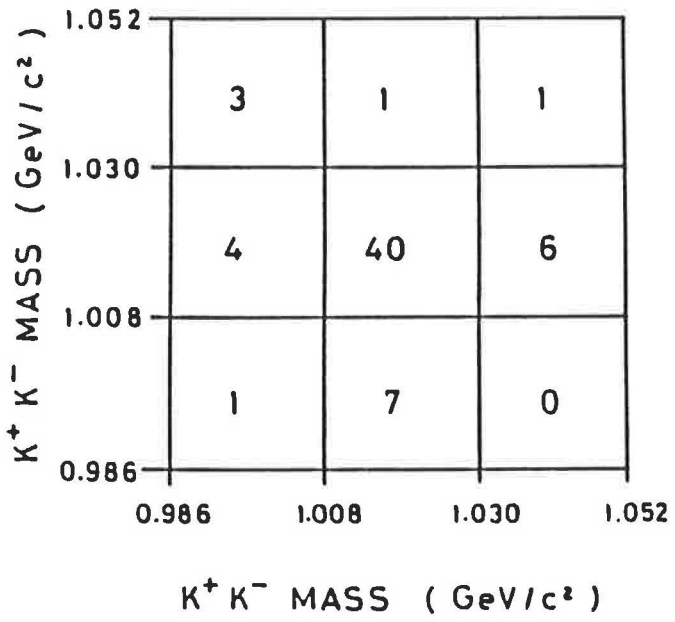

Figure 44: Scatter table of one K^+K^- mass against the other in the $\phi\phi$ region.

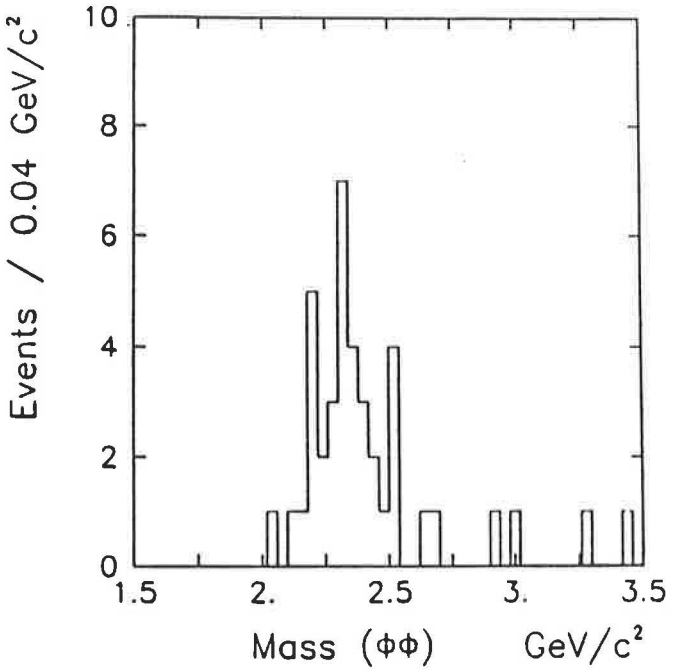

Figure 45: $\phi\phi$ effective mass spectrum for the 300 GeV/c data.

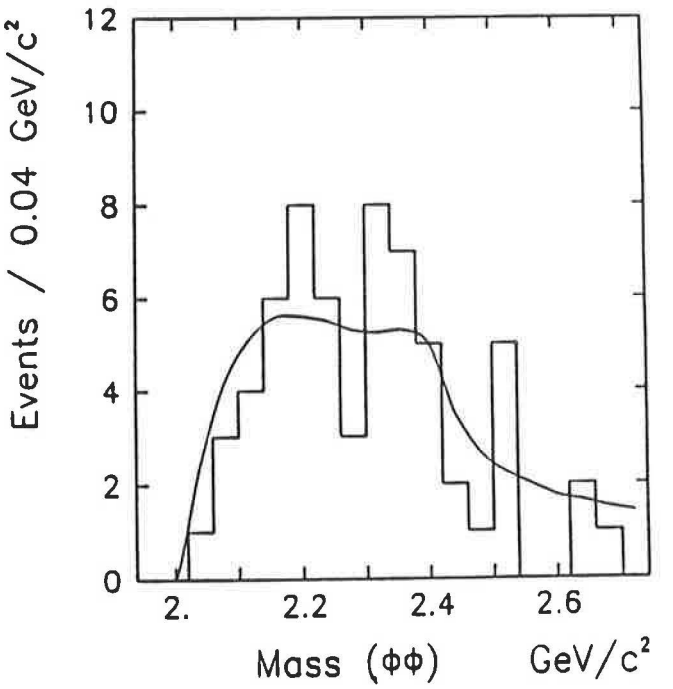

Figure 46: $\phi\phi$ effective mass spectrum for the combined 85 and 300 GeV/c data. The curve superimposed is described in the text.

7.3 A spin analysis of the $\phi\phi$ system

The angular distributions of the 4K system can be used to determine the spin-parity of the intermediate $\phi\phi$ state using a method formulated by Chang and Nelson [97] and Trueman [98]. Three angles have to be considered: the azimuthal angle χ, between the two ϕ decay planes and the two polar angles θ_1 and θ_2 of the K^+ decays in their respective ϕ rest frames relative to the ϕ momenta in the $\phi\phi$ rest frame.

For a $\phi\phi$ sample of unique spin-parity and free of background the distribution of χ takes the form

$$dN/d\chi = 1 + \beta\cos(2\chi)$$

where β is a constant which depends only on the spin-parity of the $\phi\phi$ system and is independent of its polarisation.

Table 14: The β and ξ values for different spins of the $\phi\phi$ system

J^P	L	S	β	ξ
0^+	0	0	2/3	0
0^+	2	2	1/3	1
0^-	1	1	-1	-1
1^-	1	1	0	1/2
1^+	2	2	0	1/2
2^+	0	2	1/15	0
2^+	2	0	2/3	0
2^+	2	2	2/21	3/14
2^-	1	1	$-2/5$	$-1/10$
2^-	3	1	$-3/5$	$-2/3$

Similarly

$$dN/d\cos\theta = 1 + (\xi/2)(3\cos^2\theta - 1) .$$

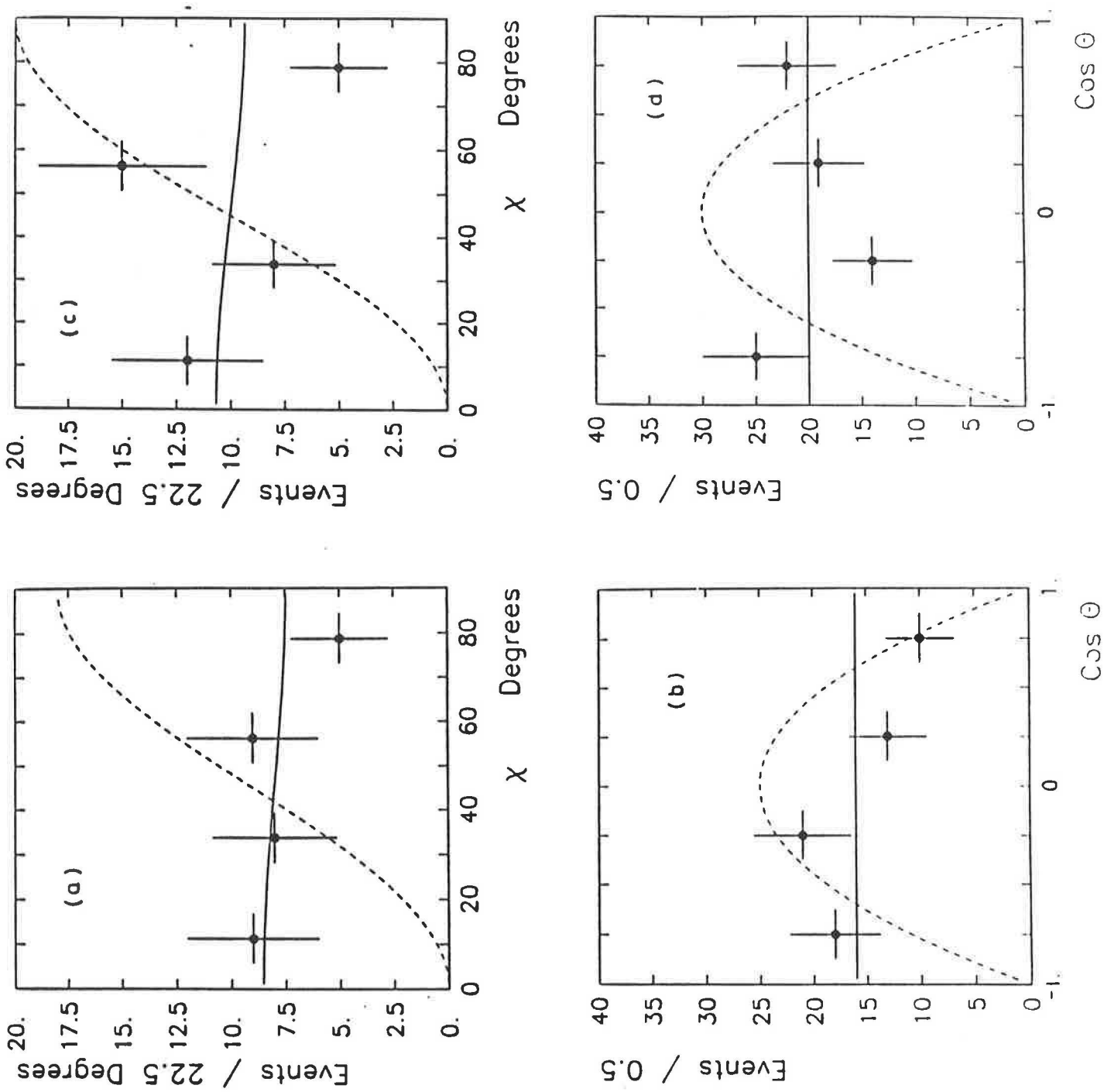

Figure 47: The χ and $\cos\theta$ distributions for a),b) the 85 GeV/c data and c),d) the 300 GeV/c data. The superimposed curves represent the 2^+ (solid) and $0-$ (broken) waves.

Values of β and ξ for different spin-parity states are given in table 14. [99]. Fig. 47 shows the χ and $\cos\theta$ distributions for the 85 and 300 GeV/c data. The $\phi\phi$ system observed in radiative J/ψ decays [59] is dominated by $J^P = 0^-$ while the $\phi\phi$ system observed in reaction (1) is dominated by $J^P = 2^+$ [57]. Curves corresponding to the distributions expected for states with $J^P = 0^-$ ($\beta = -1$, $\xi = -1$) and 2^+ ($\beta = 1/15$, $\xi = 0$) are shown in fig. 47. The data is more compatible with the 2^+ hypothesis than with the 0^-. A fit to the distributions has been performed in order to determine the values of β and ξ and gives

85 GeV/c data : $\beta = 0.3 \pm 0.2$, $\xi = -0.1 \pm 0.1$

300 GeV/c data : $\beta = 0.3 \pm 0.2$, $\xi = 0.0 \pm 0.2$

The two sets of parameters are similar and rule out the 0^- hypothesis. The acceptance has been calculated as a function of χ and $\cos\theta$ and does not change this conclusion.

7.4 $\phi\phi$ and ϕK^+K^- cross sections

In order to compare the production rates for ϕK^+K^- and $\phi\phi$, the number of ϕK^+K^- events has been estimated. This was done by subtracting twice the number of $\phi\phi$ events from the total number of ϕ's observed in fig. 40, and gives 81 ± 22 ϕK^+K^- events. The geometrical acceptance has been found to be similar for $\phi\phi$ and ϕK^+K^- production. After correcting for unseen decay modes of the ϕ, the ratio of cross sections is estimated to be

$$\sigma(\phi K^+K^-)/\sigma(\phi\phi) = 1.0 \pm 0.3$$

This compares with a value of 1.5 ± 0.6 found in central production at 85 GeV/c [96].

In order to calculate the cross-sections for the reaction

$$pp \rightarrow p_f\,(\phi\phi)\,p_s$$

at 85 and 300 GeV/c a cut has been placed on the Feynman x of the $K^+K^-K^+K^-$ system to select a region for which the acceptance is good for both experiments. The cut used is $0.0 < x_F \leq 0.2$. The number of $\phi\phi$ events in this region is

Table 15: Correction factors

	85 GeV/c	300GeV/c
Selection Cuts	1.65	1.7
Fast and medium track Geometrical acceptance	1.5	3.0
Slow proton Geometrical acceptance and low t losses	8.6 1.4	8.6 1.5
Detector inefficiencies	1.4	1.3
Reconstruction program	1.25	1.25
$K^{\pm}$ decay	2.0	1.5
$\phi\phi$ Branching ratio	4.11	4.11
Sensitivity events/nb	208	400

at 85 GeV/c	10 ± 3
at 300 GeV/c	11 ± 3

In order to calculate the cross sections the losses due to the geometrical acceptances of the fast, medium and slow tracks together with the losses due to selection cuts, detector inefficiencies etc. have been calculated. The method of calculating these correction factors is the same as that described in the previous chapter for the $K^0_S K^{\pm}\pi^{\mp}$ channel and their numerical values are given in table 15.

After taking into account these losses the cross sections are found to be

85 GeV/c :	$\sigma(\phi\phi) = 21 \pm 9$ nb
300 GeV/c :	$\sigma(\phi\phi) = 18 \pm 6$ nb

for $0.0 < x_F < 0.2$. These results are consistent with the $\phi\phi$ cross section remaining constant with incident momentum.

7.5 Conclusions

In conclusion, $\phi\phi$ production has been observed in the central region in the reaction $pp \rightarrow p_f (K^+K^-K^+K^-)\, p_s$ at 300 GeV/c. The $\phi\phi$ mass spectrum shows an accumulation of events near threshold and is similar to that observed in reaction (1) at 22 GeV/c. An angular analysis of the $\phi\phi$ system shows that $J^P = 2^+$ is favoured over 0^-, although other waves cannot be ruled out. The ratio of ϕK^+K^- to $\phi\phi$ production is 1.0 ± 0.3, which is similar to the value of 1.5 ± 0.6 found in the same reaction at 85 GeV/c [96]. The cross-sections for $\phi\phi$ production at 85 and 300 GeV/c are the same within errors. This is consistent with the $\phi\phi$ system being produced by a double Pomeron exchange mechanism which predicts that the cross section should remain constant with centre-of-mass energy.

8. THE $\pi^+\pi^-\pi^+\pi^-$ CHANNEL IN WA76′

8.1 Introduction

In recent years the 4π channel has been studied using several different production mechanisms. In two photon physics a broad enhancement is observed near threshold in $\rho^0\rho^0$ which is produced with a four times larger cross section than $\rho^+\rho^-$ [100]. It has been suggested that this suppression of $\rho^+\rho^-$ could be due to the presence of a four quark state [101]. In radiative J/ψ decays the 4π spectrum is dominated by pseudoscalar $\rho\rho$ production. No $\rho^+\rho^-$ suppression is observed but two enhancements are observed in the mass region between 1.5 and 1.8 GeV/c² with $J^{PC} = 0^{-+}$ decaying to $\rho\rho$ [102] [103]. The $4\pi^0$ channel has been studied in peripheral π^-p interactions [64] where the production mechanism is assumed to be dominated by one pion exchange. This means that the $4\pi^0$ system is restricted to $J^{PC} = (\text{even})^{++}$ and also decays involving ρ's are not possible; an analysis of this data provides evidence for two new states in the mass range 1.5 to 1.8 GeV/c².

This chapter describes an analysis of the centrally produced $\pi^+\pi^-\pi^+\pi^-$ channel from experiment WA76 at 300 GeV/c.

8.2 Selection of the channel $\pi^+\pi^-\pi^+\pi^-$

The reaction

$$pp \rightarrow p_f\,(\pi^+\pi^-\pi^+\pi^-)\,p_s,$$

has been isolated from the sample of events having six outgoing tracks by first imposing the following cuts on the components of missing momentum,

$$|\text{missing } P_x| < 20.0 \text{ GeV/c.}$$

$$|\text{missing } P_y| < 0.16 \text{ GeV/c.}$$

$$|\text{missing } P_z| < 0.06 \text{ GeV/c.}$$

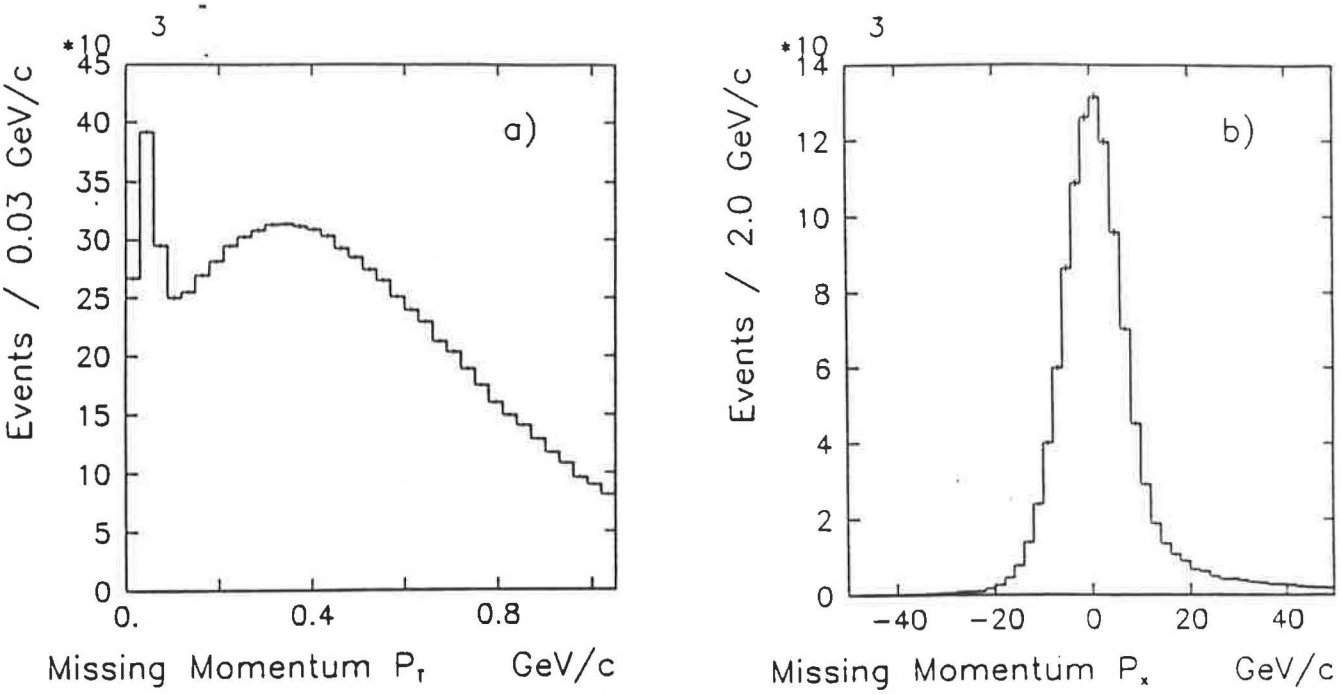

Figure 48: Missing momentum distributions for the six prong events.
a) Missing transverse momentum distribution
b) Missing longitudinal momentum distribution after a cut on the missing P_T.

Fig. 48a shows the total missing P_T where a clear signal of "4C" events can be seen. Fig. 48b shows the resulting longitudinal missing momentum after placing a cut on the missing P_T. The peak is centred at zero with very little background.

The momentum imbalance that results from these cuts is due mainly to the fast track. Therefore the fast track's momentum is recalculated to produce a completely momentum balanced system. The slow particle is identified as a slow proton by applying a cut to the pulse heights in the SPC and the TS as a function of momentum as described in chapter 3.

The central particles are then required to have a mass consistent with being a pion as given by the Cerenkov information. The Delta function defined as

$$\Delta = MM^2(p_f p_s) - M^2(\pi^+\pi^-\pi^+\pi^-)$$

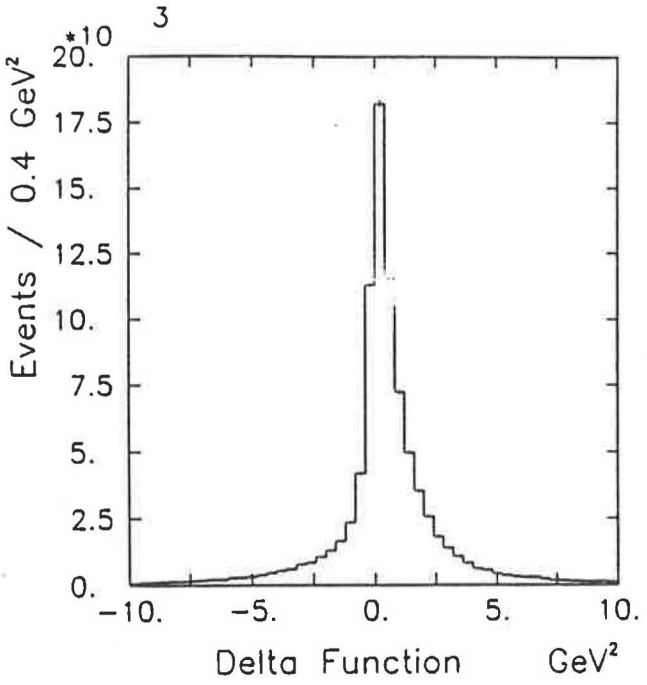

Figure 49: Delta function for the reaction $pp \rightarrow p_f(\pi^+\pi^-\pi^+\pi^-)\,p_s$.

is then calculated for each event and is shown in fig. 49. A cut of $|\Delta| \leq 3.0\ (GeV/c^2)^2$ is used to select the $\pi^+\pi^-\pi^+\pi^-$ channel (67034 events).

Figs. 50a and b show the effective mass spectrum of the fast proton and the positive and negative pions respectively. There is $\approx$ 8 % Δ^{++} contamination but no evidence for Δ^0 production. A cut of $M(p_f\pi^+) < 1.4\ GeV/c^2$ is used to remove the Δ^{++} contamination. There is no evidence of any Δ^{++} or Δ^0 production associated with the slow proton.

The four-momentum transfer squared at the fast and the slow vertex is shown in fig. 51a and b respectively. A fit to these spectra using an expression of the form exp(B|t|) gives for

$$|t(\text{fast})| \qquad B = -(6.5 \pm 0.1)\ GeV^{-2}.$$

$$|t(\text{slow})| \qquad B = -(6.0 \pm 0.1)\ GeV^{-2},$$

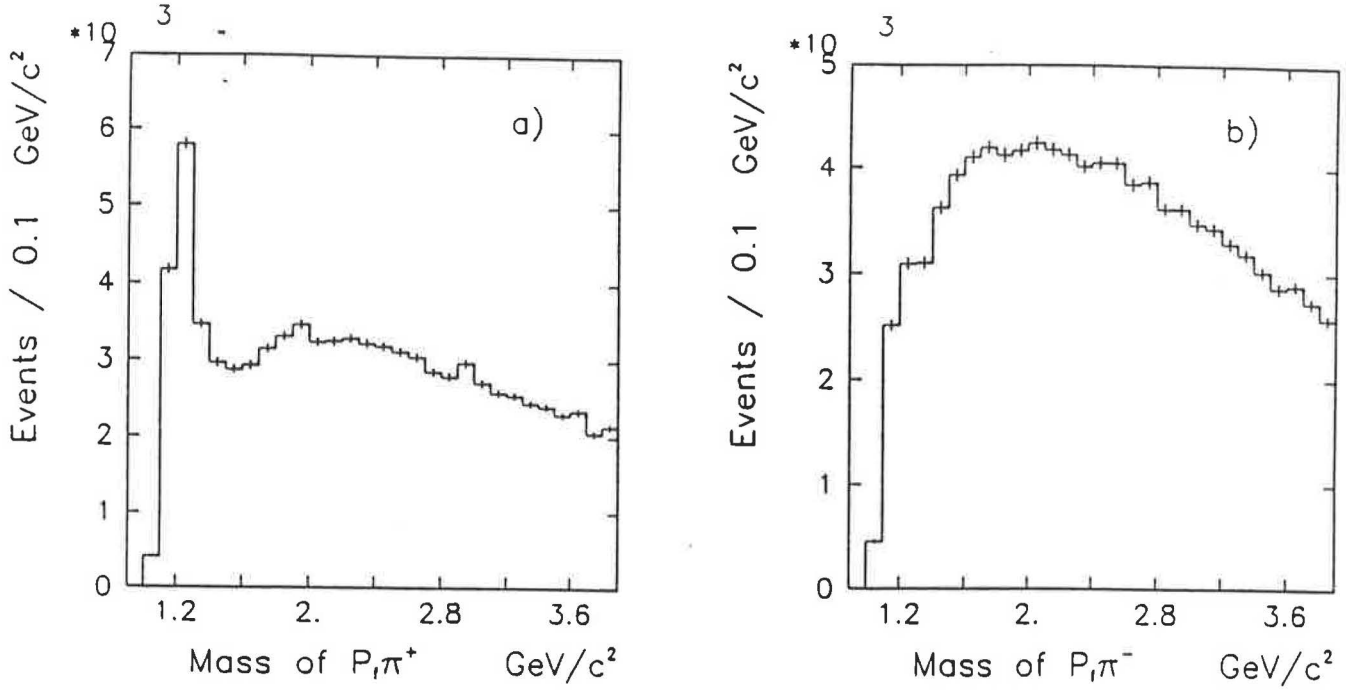

Figure 50: Fast track effective mass distributions.
a) $M(p_f\pi^+)$ and
b) $M(p_f\pi^-)$ in the reaction $p_f\,(\pi^+\pi^-\pi^+\pi^-)\,p_s$.

Fig. 52a shows the $\pi^+\pi^-\pi^+\pi^-$ effective mass spectrum; a clear peak is seen at 1.28 GeV/c² which is probably due to the $f_1(1285)$. It is also difficult to ignore the enhancement in the 1.45 GeV/c² region. In order to try to describe the $\pi^+\pi^-\pi^+\pi^-$ mass spectrum it was initially fitted with a single Breit-Wigner, representing the peak in the 1.28 GeV/c² region, plus a background of the form $a(m-m_{th})^b\exp(-cm-dm^2)$, where m is the $\pi^+\pi^-\pi^+\pi^-$ mass, m_{th} is the $\pi^+\pi^-\pi^+\pi^-$ threshold mass and a, b, c, d are fit parameters. Also included in the fit are two histograms, generated from real data, representing reflections from the $\eta\pi^+\pi^-$ decay of the η' and $f_1(1285)$. These reflections give small enhancements in the $\pi^+\pi^-\pi^+\pi^-$ mass spectrum in the 0.8 and 1.1 GeV/c² regions and are due to a slow π^0 from the decay of an η falling within the missing momentum cuts. The χ^2/NDF obtained was 283/142 indicating a bad fit. The major contributions to the χ^2 come from the 1.45 and 1.9 GeV/c²

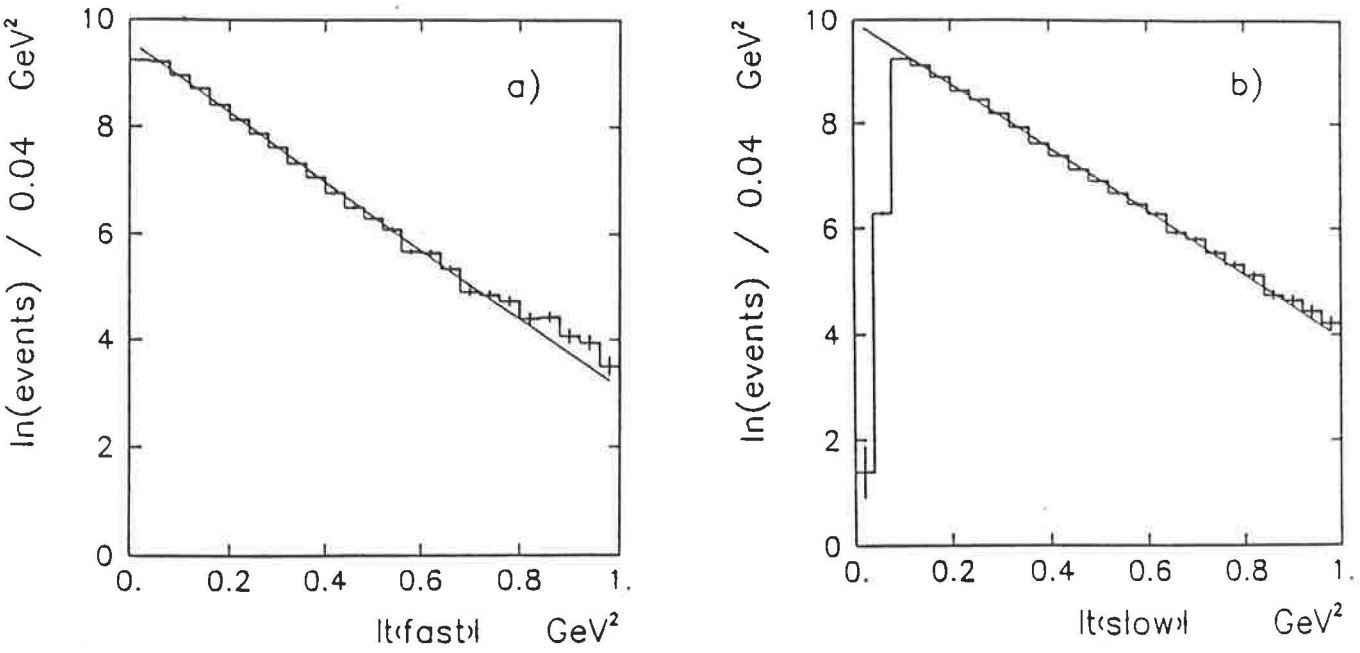

Figure 51: The Four-momentum transfer squared at the a) fast and b) slow vertex.

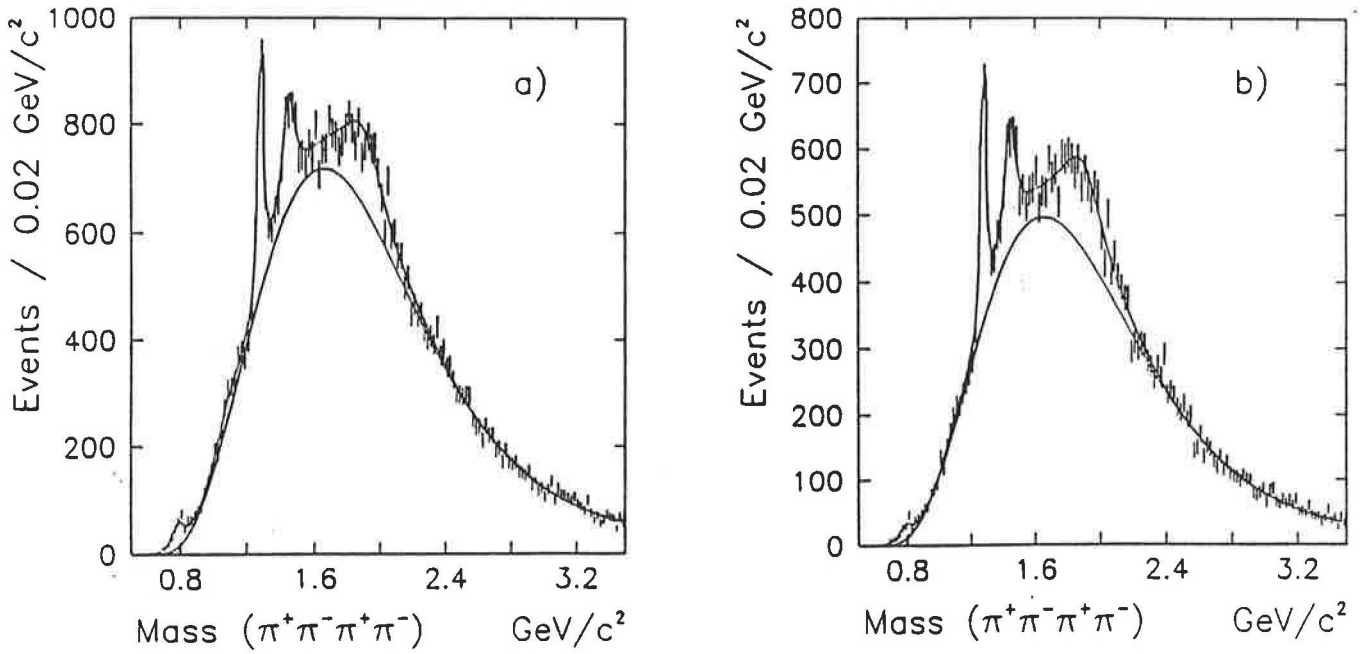

Figure 52: The $\pi^+\pi^-\pi^+\pi^-$ effective mass spectrum with fit using 3 Breit-Wigners.
a) Total spectrum and b) requiring no γ's detected in the gamma calorimeter.

Table 16:	Parameters of resonances in the fit to the $\pi^+\pi^-\pi^+\pi^-$ mass spectrum				
$f_1(1285)$	Mass	1281	±	1	MeV
	Γ	31	±	5	MeV
X(1450)	Mass	1449	±	4	MeV
	Γ	78	±	18	MeV
X(1900)	Mass	1901	±	13	MeV
	Γ	312	±	61	MeV

regions. A Breit-Wigner was then introduced to take account of the enhancement at 1.45 GeV/c^2 which resulted in a χ^2/NDF of 233/139. If a third Breit-Wigner is introduced to describe the excess of events in the 1.9 GeV/c^2 region the fit has a χ^2/NDF of 137/136. If now the Breit-Wigner describing the 1.45 GeV/c^2 enhancement is omitted the χ^2/NDF increases to 231/139 again requiring a third Breit-Wigner in the 1.45 GeV/c^2 region.

Thus the data require the introduction of two Breit-Wigners, in addition to the one to describe the peak at 1.28 GeV/c^2, to account for the excess of events at 1.45 GeV/c^2 and at 1.9 GeV/c^2. From now on these enhancements are referred to as X(1450) and X(1900). The masses and widths determined from the fit are given in table 16.

Fig. 52b shows the $\pi^+\pi^-\pi^+\pi^-$ mass spectrum when no γ's are detected in the gamma calorimeter. The η' and $f_1(1285)$ reflections are reduced but the $f_1(1285)$, X(1450) and X(1900) signals are enhanced, indicating that they are not themselves reflections from a channel involving a π^0 which falls within the missing momentum cuts.

Fig. 53a shows the $\pi^+\pi^-\pi^+\pi^-$ mass spectrum when a cut of $|t| < 0.15$ GeV^2 has been placed on the four-momentum transfer squared at both the fast and slow vertices. The spectrum is fitted using three Breit-Wigners, with masses and widths fixed to the values given in table 16, and a background as

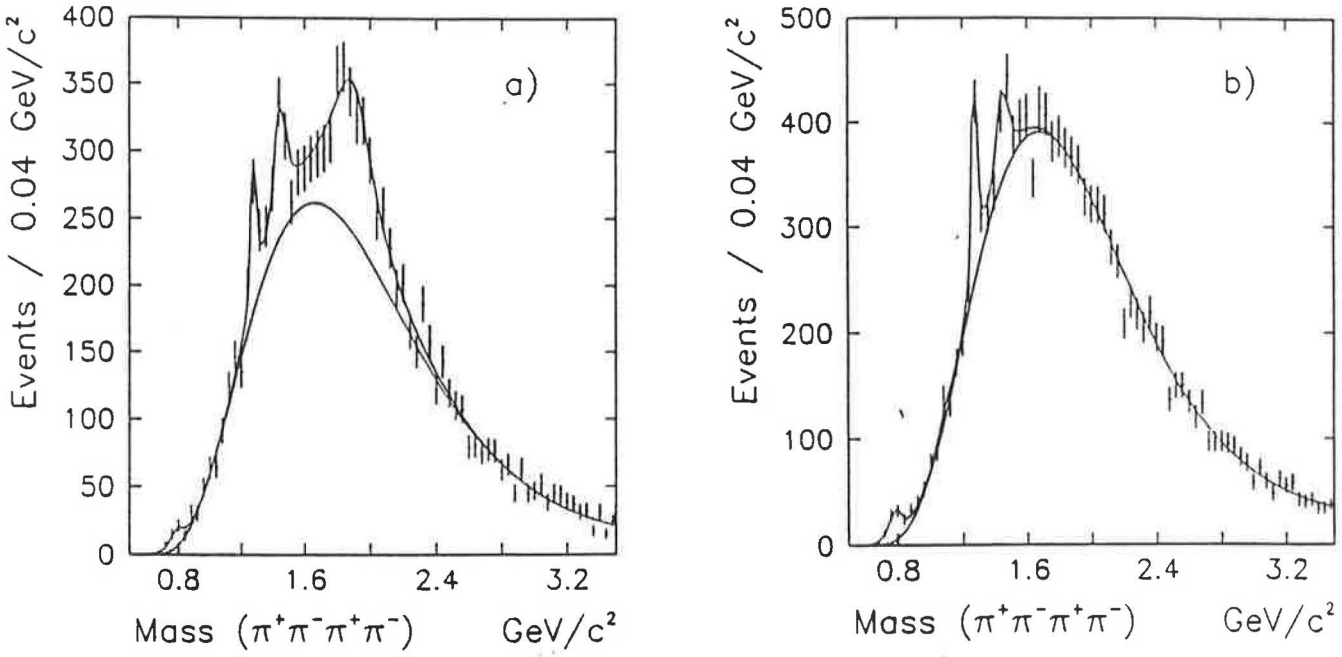

Figure 53: The $\pi^+\pi^-\pi^+\pi^-$ effective mass spectrum with fit, for a) |t(slow)| and |t(fast)| < 0.15 $(GeV)^2$ and b) |t(slow)| and |t(fast)| > 0.15 $(GeV)^2$.

described above (χ^2/NDF = 67/65). Fig. 53b shows a fit to the $\pi^+\pi^-\pi^+\pi^-$ mass spectrum when both the slow and fast vertices have |t| > 0.15 GeV^2. Since there is only evidence for the $f_1(1285)$ and X(1450) the fit uses only two Breit-Wigners, with fixed mass and width and has a χ^2/NDF of 61/66. If a third Breit-Wigner is introduced describing the X(1900) the χ^2/NDF changes to 59/65. It thus appears that the X(1900) is produced predominantly at low |t|.

8.3 A comparison of the enhancements at 1.28 and 1.45 GeV/c^2 in the $K^0_S K^{\pm}\pi^{\mp}$ and $\pi^+\pi^-\pi^+\pi^-$ channels

A possible explanation of the X(1450) is that it is the $f_1(1420)$ observed in the $K^0_S K^{\pm}\pi^{\mp}$ channel. The selection of the channel $K^0_S K^{\pm}\pi^{\mp}$ has been described in chapter 5 and shows enhancements which have been identified as the $f_1(1285)$ and $f_1(1420)$. The mass and width of the peak observed in the $\pi^+\pi^-\pi^+\pi^-$ spectrum at 1.28 GeV/c^2 (1281±1, 31±5 MeV/c^2) is consistent with that found for the $f_1(1285)$ in the $K^0_S K^{\pm}\pi^{\mp}$ spectrum (1278±2, 25±4 MeV/c^2). In contrast, the peak at 1.45 GeV/c^2 in the $\pi^+\pi^-\pi^+\pi^-$ mass spectrum has a mass of 1449±4 MeV/c^2 which differs from the mass of 1429±3 MeV/c^2 found for the mass of the $f_1(1420)$ in the $K^0_S K^{\pm}\pi^{\mp}$ spectrum by 4σ. In addition, to test whether the peak seen at 1.45 GeV/c^2 in the $\pi^+\pi^-\pi^+\pi^-$ mass spectrum is a new $\pi^+\pi^-\pi^+\pi^-$ decay mode of the $f_1(1420)$, the $\pi^+\pi^-\pi^+\pi^-$ mass spectrum has been fitted using the mass and width determined for the $f_1(1420)$ from a fit to the $K^0_S K^{\pm}\pi^{\mp}$ spectrum. The χ^2/NDF increases from 137/136, with a free mass and width of the X(1450), to 169/138 when the parameters are fixed.

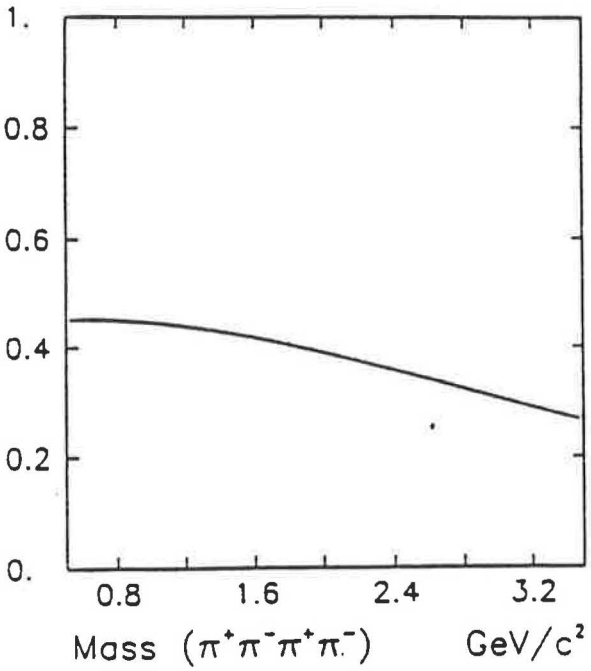

Figure 54: The geometrical acceptance as a function of the $\pi^+\pi^-\pi^+\pi^-$ effective mass.

A study has been made of the branching ratios of the 1.28 and 1.45 GeV/c^2 enhancements to $K^0_S K^{\pm}\pi^{\mp}$ and $\pi^+\pi^-\pi^+\pi^-$ for |t(slow)| < 0.2 GeV^2 and |t(slow)| > 0.2 GeV^2 which divides the data into two equal samples. If the enhancements seen in the two channels are the same the branching ratios should be constant with |t|.

The geometrical acceptance for the $\pi^+\pi^-\pi^+\pi^-$ system has been calculated and is found to be smoothly varying with effective mass as is shown in fig. 54, where it has been fitted by a third order polynomial. The calculation of the geometrical acceptance for the $K^0_S K^{\pm}\pi^{\mp}$ has been described in chapter 5.

Table 17: The number of events in the enhancements in the 1.28 (R_1) and 1.4 (R_2) GeV/c^2 regions.

	Low |t|	High |t|
For the $K^0_S K^{\pm}\pi^{\mp}$ channel.		
R_1	202±27	275±27
R_2	581±42	904±51
For the $\pi^+\pi^-\pi^+\pi^-$ channel.		
R_1	1294±58	1741±67
R_2	1639±173	1139±181

The geometrically acceptance corrected mass spectra have been fitted in the two |t| regions where the masses and widths of the enhancements have been fixed to the values determined from a fit to the total mass spectra. The number of events in the resonance peaks for each channel and in each |t| region is given in table 17.

Defining R to be the number of events in the $\pi^+\pi^-\pi^+\pi^-$ peak divided by the number in the $K^0_S K^\pm\pi^\mp$ peak, results in the following values for the 1.28 GeV/c^2 region

$$R = 6.4 \pm 0.9 \text{ at low } |t| \text{ and}$$

$$R = 6.3 \pm 0.7 \text{ at high } |t|.$$

This, together with the fact that the masses and widths are found to be consistent in the two channels indicates that they are two decay modes of the same resonance which has been determined to be the $f_1(1285)$ from a spin parity analysis of the $K^0_S K^\pm\pi^\mp$ channel.

In contrast, however, in the 1.45 GeV/c^2 region

$$R = 2.8 \pm 0.4 \text{ at low } |t| \text{ and}$$

$$R = 1.3 \pm 0.2 \text{ at high } |t|.$$

Hence there is a 3σ change with |t|. This change in R together with the fact that the mass of the $\pi^+\pi^-\pi^+\pi^-$ enhancement (1449 ± 4 MeV/c^2) is inconsistent with the mass of the $f_1(1420)$ in the $K^0_S K^\pm\pi^\mp$ channel (1429 ± 3 MeV/c^2) suggests that the resonance observed in the $\pi^+\pi^-\pi^+\pi^-$ channel is not due to a $\pi^+\pi^-\pi^+\pi^-$ decay mode of the $f_1(1420)$.

If the X(1450) is not the $f_1(1420)$ then another possibility is that it could be a $\pi^+\pi^-\pi^+\pi^-$ decay mode of the $J^{PC} = 0^{-+}$ $\iota/\eta(1440)$ observed in radiative J/ψ decays to $K\bar{K}\pi$ with a mass of 1454 ± 3 MeV/c^2 and a width of 98 ± 7 MeV/c^2 [5]. However this state is not observed in the $K^0_S K^\pm\pi^\mp$ channel of the present experiment as was discussed in chapters 5 and 6, thus ruling out this hypothesis.

8.4 Channel likelihood fit

8.4.1 Introduction

In order to determine the different reactions that contribute to the observed final states a channel likelihood fit [104] using a modified version of CHAFIT [105] has been used. The program performs a maximum likelihood fit of different overlapping amplitudes. The amplitudes used are Breit-Wigners describing the observed resonances. The resonances considered are as follows :−

1. In the 4π channel the $f_1(1285)$, X(1450) and X(1900) together with the η' and $f_1(1285)$ reflections from the $\eta\pi\pi$ channel.

2. In the 3π channel the $a_1(1260)$ and $a_2(1320)$, where both states are considered decaying to 3π and $\rho^0\pi$.

3. In the 2π channel the $\rho^0(770)$, $f_2(1270)$ and K^0_S.

4. In the $p_f\pi$ channel the Δ^{++} and Δ^0, where $\Delta 3\pi$ and $\Delta\rho^0\pi$ decay modes are considered.

Table 18 shows a list of all the amplitudes used in the fit.

The masses and widths used to describe the $f_1(1285)$, X(1450) and X(1900) are those determined from the fit to the $\pi^+\pi^-\pi^+\pi^-$ mass spectrum. The η' and $f_1(1285)$ reflections from the $\eta\pi\pi$ channel have been parameterised as two Gaussians with masses of 800 and 1059 MeV/c^2 respectively and with σ's of 56 and 99 MeV/c^2 respectively. The K^0_S was parameterised as a Gaussian centred at the K^0_S mass and having a σ of 7.0 MeV/c^2. The masses and widths of the particles observed in the 2π, 3π and $p_f\pi$ channels have been fixed at their PDG values [42].

Each amplitude has to be normalised by integrating over the Lorentz Invariant Phase Space (LIPS). However due to the trigger and the acceptance the observed phase space represents a limited region of the true phase space. Therefore it is not easy to generate a phase space that would reproduce the experimentally observed phase space.

Table 18: Amplitudes used in the fit

$f_1(1285)\rightarrow 4\pi$	$f_1(1285)\rightarrow \rho\pi\pi$	
$X(1450)\rightarrow 4\pi$	$X(1450)\rightarrow \rho\pi\pi$	$X(1450)\rightarrow \rho\rho$
$X(1450)\rightarrow a_1(\rho\pi)\pi$	$X(1450)\rightarrow a_2\pi$	
$X(1900)\rightarrow 4\pi$	$X(1900)\rightarrow \rho\pi\pi$	$X(1900)\rightarrow \rho\rho$
$X(1900)\rightarrow a_1\pi$	$X(1900)\rightarrow a_2\pi$	$X(1900)\rightarrow f_2\pi\pi$
η'(refl)	$f_1(1285)$(refl)	
$a_1(\rightarrow 3\pi)\pi$	$a_1(\rightarrow \rho\pi)\pi$	$a_1(3\pi(\text{phase}))\pi$
$a_2(\rightarrow 3\pi)\pi$	$a_2(\rightarrow \rho\pi)\pi$	
$\rho\pi\pi$	$f_2\pi\pi$	$K^0S\pi\pi$
$\rho\rho$	ρf_2	f_2f_2
$\Delta^{++}3\pi$	$\Delta^{++}\rho\pi$	$\Delta^{++}f_2\pi$
$\Delta^{++}a_2$		
$\Delta^0 3\pi$	$\Delta^0\rho\pi$	$\Delta^0 f_2\pi$
$\Delta^0 a_2$		

The best method that has been found to reproduce the experimental phase space is to take the six outgoing tracks from 1000 events and randomly mix them, so that 100000 artificial events were generated using one fast, one slow and four central tracks from six different events.

Initially the fit is performed using the amplitudes which are known to be present (i.e. $\rho\pi\pi$, $\rho\rho$, $f_2\pi\pi$, $a_2\pi$ and $\Delta^{++}3\pi$). Then other amplitudes are added (e.g. $f_1(1285)\rightarrow 4\pi$ etc.) one at a time and a new fit is performed. Whether an amplitude is required or not is decided upon by consideration of the following:

1. The change in the likelihood of the fit if the amplitude is omitted.

2. The resulting spectra after subtraction of the amplitudes i.e. if they appear phase space like.

3. The amount of wave required by the fit must agree approximately with the amount calculated from a fit to the mass spectrum.

The aim of this study is :

1. To determine through which channel(s) the enhancements at 1.28 and 1.45 GeV/c^2 decay.

2. To see whether or not the enhancement at 1.9 GeV/c^2 is due to a peak in the phase space distributions of the two and/or three body decay processes. If it can not be accounted for in this way then to consider it as a resonance and determine which channels it decays through.

3. To determine what subprocesses occur and in what fractions e.g. $\rho^0\rho^0$ production.

The method for the calculation of the errors in the histograms of weighted events is described in appendix D.

8.4.2 Results of the fit

The results of the fit to the total $\pi^+\pi^-\pi^+\pi^-$ mass spectrum (67034 events) is shown in table 19. Figs. 55a and b show the total $\pi^+\pi^-\pi^+\pi^-$ mass spectrum before and after subtraction of the amplitudes. Figs. 56a and b show the various subprocess mass spectra before and after subtraction of the amplitudes. As can be seen all the resonances have been subtracted by the fit.

In order to test whether the X(1900) is due to reflections coming from the combinations of 2π and 3π subprocesses CHAFIT has been used and the parameterisation of the X(1900) as a Breit-Wigner has been omitted. Since the X(1900) is seen predominantly at low |t| this analysis has been performed requiring that both the slow and fast vertices has $|t| < 0.15$ GeV^2. The $\pi^+\pi^-\pi^+\pi^-$ mass spectrum after subtraction of the 2π, 3π and 4π resonances should be phase space like if the X(1900) is a background effect. The resulting spectrum is shown in fig. 57 where the X(1900) signal can be seen showing that a resonance interpretation is required.

The main results can be summarised as follows :

1. The $f_1(1285)$ and X(1450) decay dominantly to $\rho^0\pi^+\pi^-$.

2. The X(1900) is found to decay equally to $f_2(1270)\pi\pi$ and $a_2(1320)\pi$.

Table 19: Results from CHAFIT.

Channel	Percentage
$p_f(f_1(1285)\rightarrow\rho^0\pi^+\pi^-)p_S$	3.1 ± 0.1
$p_f(X(1450)\rightarrow\rho^0\pi^+\pi^-)p_S$	2.7 ± 0.2
$p_f(X(1900)\rightarrow f_2\pi^+\pi^-)p_S$	2.3 ± 0.2
$p_f(X(1900)\rightarrow a_2\pi)p_S$	2.5 ± 0.4
$p_f(\rho^0\pi^+\pi^-)p_S$	40.0 ± 1.0
$p_f(f_2\pi^+\pi^-)p_S$	3.8 ± 0.3
$p_f(a_2\pi)p_S$	5.0 ± 0.6
$p_f(\rho^0\rho^0)p_S$	3.0 ± 0.4
$\Delta^{++}\rightarrow p_f\pi^+(\pi^+\pi^-\pi^-)p_S$	8.7 ± 0.2
$\Delta^0\rightarrow p_f\pi^-(\pi^+\pi^-\pi^+)p_S$	1.5 ± 0.1
K^0_S contamination	1.4 ± 0.1
η' reflection	0.8 ± 0.1
$f_1(1285)$ reflection	2.9 ± 0.1
Phase Space	21.8 ± 0.8

3. There is 3.0 ± 0.4 % $\rho^0\rho^0$ production.

The results from CHAFIT have been checked by fitting the 2π and 3π mass spectra as a function of the 4π mass using Breit-Wigners to describe the $\rho^0(770)$, $f_2(1270)$ and $a_2(1320)$. The number of $\rho\pi\pi$, $f_2\pi\pi$ and $a_2\pi$ events have been calculated from these fits in 50 MeV/c^2 intervals. Fig. 58 shows the resulting $\rho\pi\pi$ mass spectrum. The $f_1(1285)$ and X(1450) can be seen; the number of events in each peak is consistent with the result from CHAFIT that they both decay dominantly to $\rho\pi\pi$. Fig. 59a and b shows the resulting $a_2\pi$ and $f_2\pi\pi$ mass spectra respectively. A peak can be seen just below 1.9 GeV/c^2 in the $a_2\pi$ spectrum and just above 1.9 GeV/c^2 in the $f_2\pi\pi$ spectrum. This is again consistent with the result from CHAFIT that the X(1900) decays equally to $a_2\pi$ and $f_2\pi\pi$. The

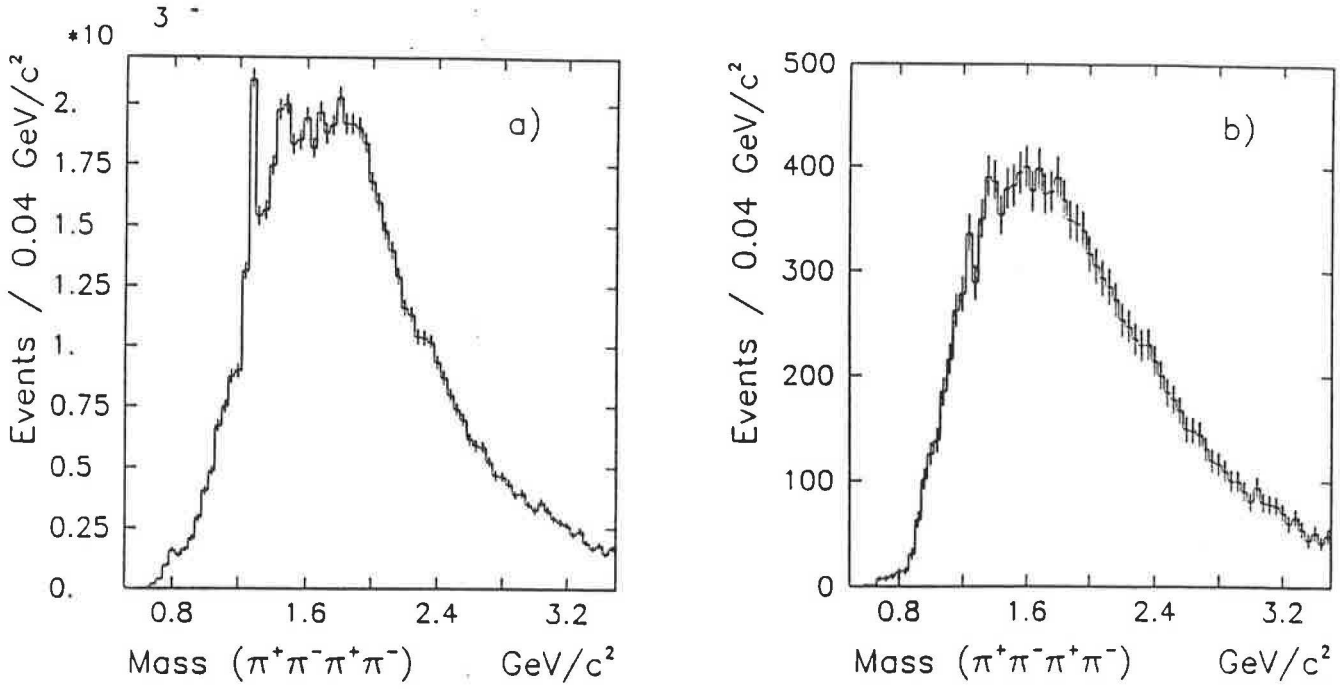

Figure 55: The $\pi^+\pi^-\pi^+\pi^-$ effective mass spectrum
a)Total, b) After subtraction of the amplitudes used in the fit.

splitting could either be due to phase space consideration or due to the fact that the X(1900) is not a single resonance but in fact two separate resonances, one that decays to $a_2\pi$ and one that decays to $f_2\pi\pi$.

8.5 A spin-parity analysis of the $f_1(1285)$ and X(1450)

A spin-parity analysis of the $\pi^+\pi^-\pi^+\pi^-$ channel has been performed, assuming that the resonances are isoscalar. The $\rho^0\pi^+\pi^-$ decay mode of the $f_1(1285)$ and X(1450) have been parameterised in terms of quasi two-body final states corresponding to ρ $(\pi\pi)$ and $(\rho\pi)$ π where it is assumed that the $\pi\pi$ and $\rho\pi$ interactions are strong compared to any other interaction.

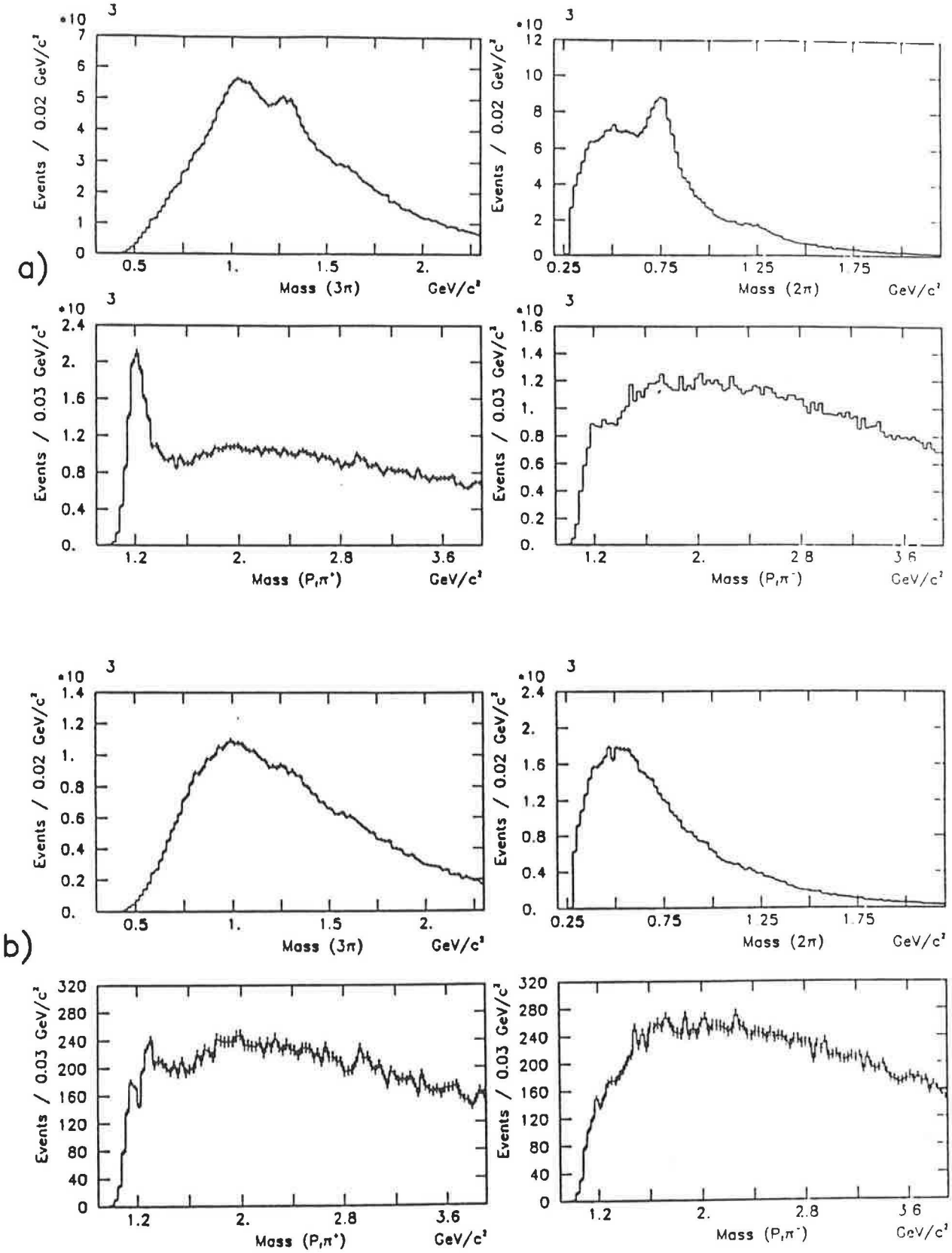

Figure 56: The 2π, 3π and $p\pi$ effective mass spectra
a)Total, b) After subtraction of the amplitudes used in the fit.

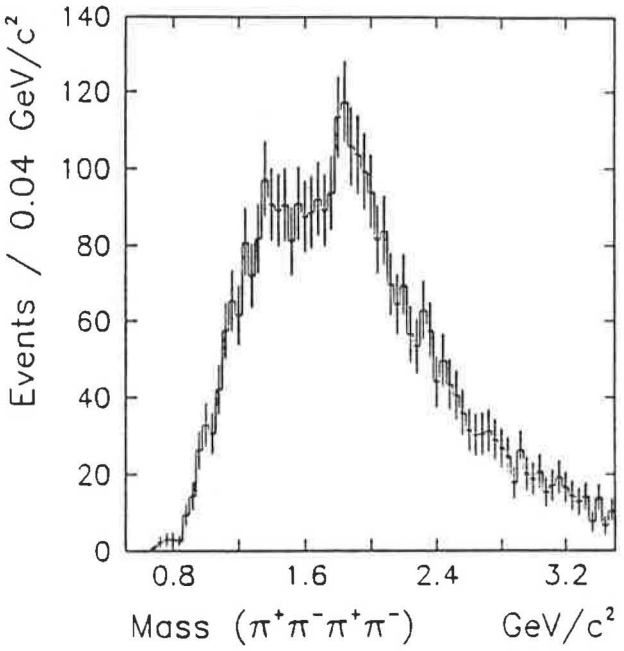

Figure 57: The $\pi^+\pi^-\pi^+\pi^-$ mass spectrum after subtraction of the 2π, 3π and 4π resonances. X(1900) parameterisation omitted.

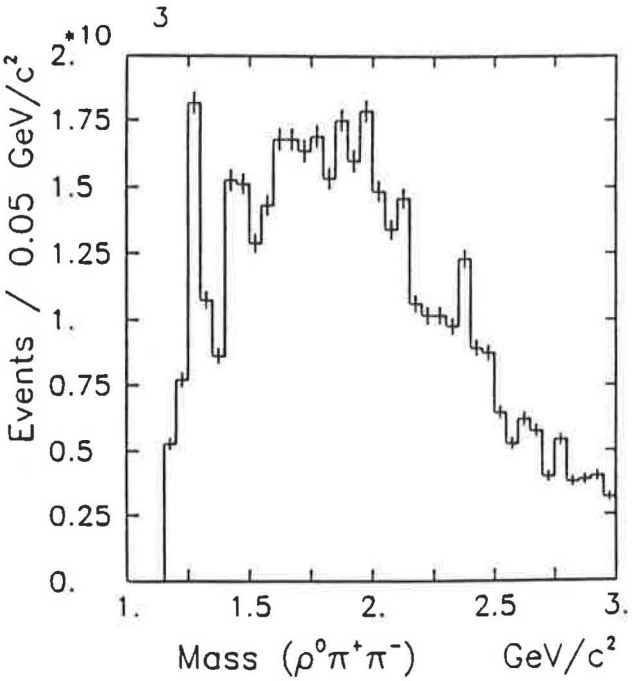

Figure 58: The $\rho^0\pi^+\pi^-$ effective mass spectrum.

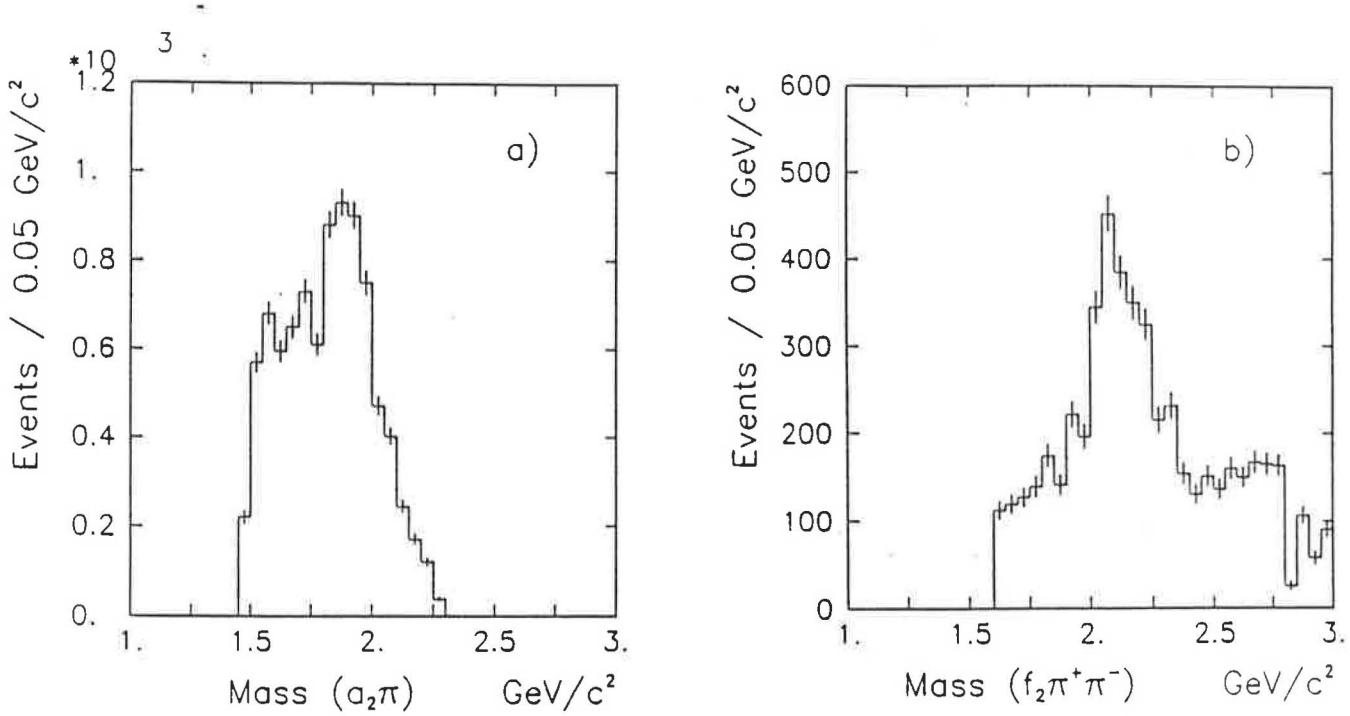

Figure 59: The a) $a_2\pi$ and b) $f_2\pi\pi$ mass spectra.

8.5.1 The ρ ($\pi\pi$) case

For the decay of an isoscalar resonance to ρ^0 ($\pi^+\pi^-$) since the G-parity of the $\pi^+\pi^-$ pair is positive then by Bose symmetry

$$G = (-1)^{\ell + I} = +1$$

where ℓ is the angular momentum between the π^+ and π^- and I is the isospin of the $\pi^+\pi^-$ system. Since the ρ^0 has I = 1 in order to get an overall isoscalar system the $\pi^+\pi^-$ system must also have I = 1 and hence ℓ must be odd.

Assuming the lowest angular momentum (ℓ = 1) between the π^+ and π^- then the $\pi^+\pi^-$ system has $J^{PC} = 1^{--}$ and can be treated as a pseudo-ρ^0. Therefore there is a real ρ^0 and a pseudo-ρ^0 and hence the system can be described as the decay into two vector particles.

The angular distributions of the $\rho\pi\pi$ system can then be used to determine the spin-parity of the $f_1(1285)$ and X(1450) using a modified version of the formalism of Chang and Nelson [97] and Trueman [98] which was described in chapter 7. In this case two angles have to be considered: the azimuthal angle χ between the ρ^0 and the pseudo-ρ^0 decay planes, and the polar angle θ of the π^+ decay in the ρ^0 rest frame relative to the ρ^0 momentum in the $\rho^0\pi^+\pi^-$ rest frame.

Unlike the $\phi\phi$ case, there is a combinatorial problem in the $\rho^0\pi^+\pi^-$ system because more than one $\pi^+\pi^-$ pair can have an effective mass in the ρ^0 mass range. The number of combinatorials increases from the $f_1(1285)$ to the X(1450) region. A Monte Carlo, based on the FOWL [93] phase space program described in chapter 6, has been used to calculate the predicted angular distributions for different spins, up to J = 2, taking into account the ρ combinatorial effect.

The $\rho^0\pi^+\pi^-$ mass spectra have been fitted as a function of χ and $\cos\theta$ using Breit-Wigners to describe the $f_1(1285)$ and X(1450) and a background of the form $a(m-m_{th})^b\exp(-cm-dm^2)$, where m is the $\rho^0\pi^+\pi^-$ mass, m_{th} is the $\rho^0\pi^+\pi^-$ threshold mass and a, b, c, d are fit parameters. The numbers of $f_1(1285)$ and X(1450) events have been calculated from these fits and the resulting acceptance corrected angular distributions are shown in fig. 60.

In the $f_1(1285)$ region (fig. 60a,b) curves corresponding to states with $J^P = 0^-$, $1^\pm$ and 2^+ are shown. The $J^P = 1^\pm$ hypothesis gives the best description of the data (χ^2/NDF = 4/13). In the X(1450) region (fig. 60c,d) the $J^P = 0^-$ hypothesis can be excluded (χ^2/NDF = 50/13); the $J^P = 1^\pm$ (χ^2/NDF = 13/13) and 2^+ (χ^2/NDF = 9/13) hypotheses all give acceptable descriptions of the data.

8.5.2 The $(\rho\pi)\,\pi$ case

A spin-parity analysis of the $\rho\pi$ subsystem from the $\pi^+\pi^-\pi^+\pi^-$ channel at 85 GeV/c showed that it was dominated by the 1^+ S wave [106] which can be parameterised as a pseudo-$a_1(1260)$. Therefore a spin-parity analysis of the $(\rho\pi)\,\pi$ case has been performed using Zemach tensors [87] and a pseudo $a_1(1260)$ isobar to describe the 1^+ S wave intermediate $\rho\pi$ state, where the fit is not found to be sensitive to the a_1 parameters used.

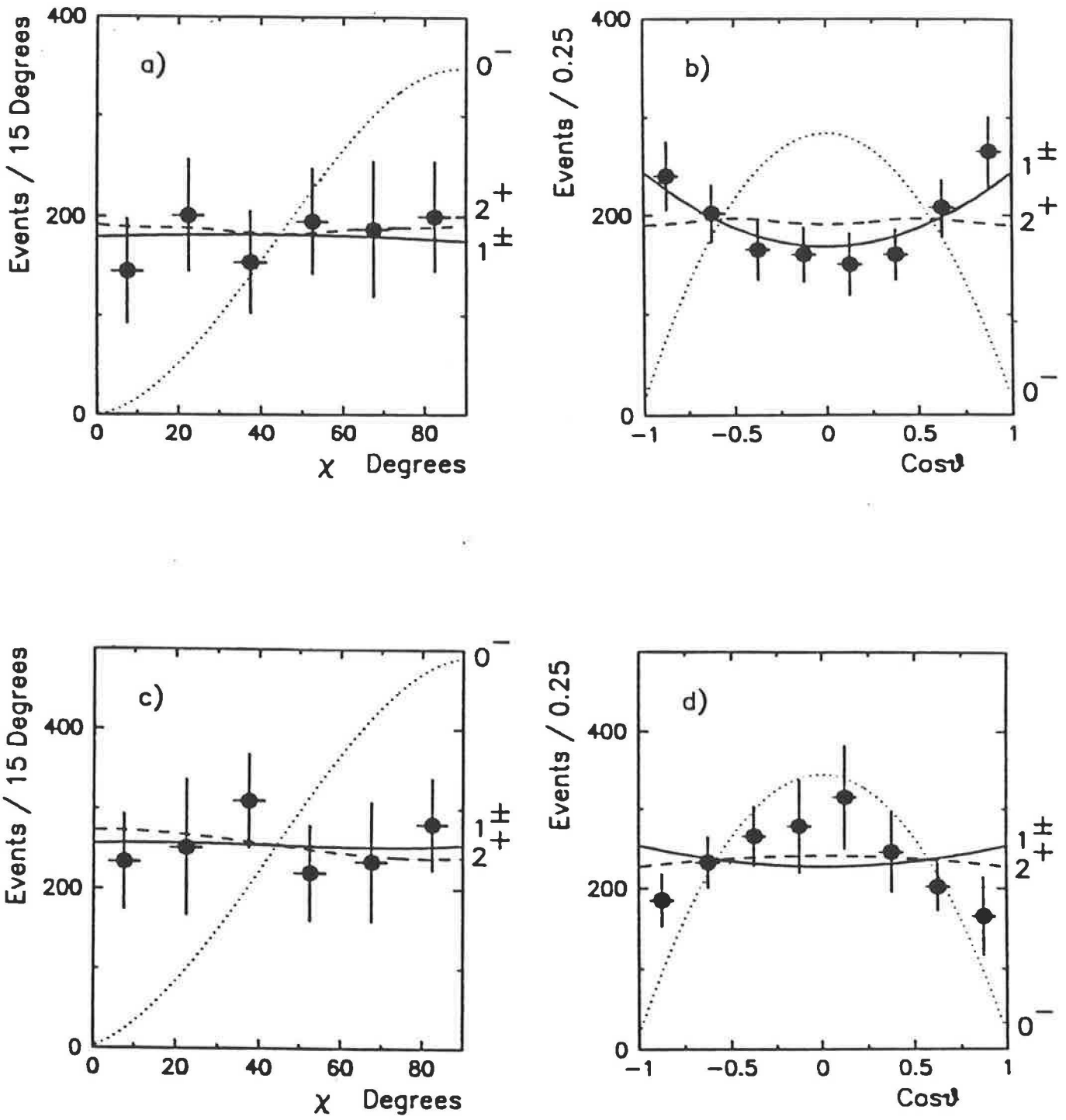

Figure 60: The χ and $\cos\theta$ distributions for a),b) the $f_1(1285)$ region and c),d) the X(1450) region.
The superimposed curves are described in the text.

The $\pi^+\pi^-\pi^+\pi^-$ state can decay into four pseudo-$a_1(1260)$ states which can themselves decay into two $\rho\pi$ states. The interference terms between these various intermediate states are determined by their G-parity. The final matrix element for the decay into $\pi^+{}_1\pi^-{}_2\pi^+{}_3\pi^-{}_4$ via an intermediate $a_1(1260)$ state is

$$\begin{aligned} M \quad = \quad & BW(a_1(123))[BW(\rho(12))M(1234) - BW(\rho(23))M(2314)] \\ & + BW(a_1(124))[BW(\rho(12))M(1243) - BW(\rho(14))M(1423)] \\ & + BW(a_1(134))[BW(\rho(14))M(1432) - BW(\rho(34))M(3412)] \\ & + BW(a_1(234))[BW(\rho(23))M(2341) - BW(\rho(34))M(3421)]. \end{aligned}$$

Where M(ijkl) is the matrix element describing the spin-parity of the decaying particle and $BW(a_1(ijk))$ and $BW(\rho(ij))$ are Breit-Wigner functions describing the $a_1(1260)$ and $\rho(770)$ decays respectively.

The decay matrix elements for a state X to decay to a $\pi^+\pi^-\pi^+\pi^-$ final state through the decay chain $X \rightarrow a_1\pi \rightarrow \rho\pi\pi$, with angular momentum L between the a_1 and π, are given in table 20. Where $\vec{t}$ is the tensor describing the 1^+ S wave decay of the $a_1(1260)$ into a ρ and a π and is given by

$$\vec{t} = \vec{P}_i - \vec{P}_j$$

where $\vec{P}_i$ and $\vec{P}_j$ are the momenta of the two π's, in the 4π centre-of-mass, coming from the decay of the ρ. $\vec{P}_l$ is the momentum of the π opposite the $a_1(1260)$ in the 4π centre-of-mass and

$$A_{ij}(\vec{a},\vec{b}) = 1/2(a_ib_j - a_jb_i) - 1/3\,\delta_{ij}(\vec{a}.\vec{b}).$$

For the $(\rho\pi)\,\pi$ case the angles found to contain information are the polar angle θ_1 between the π^+ coming from the decay of the ρ^0 relative to the ρ^0 momentum, and the polar angle θ_2 of the π^+ from the $\pi^+\pi^-$ pair not in the ρ^0 relative to the ρ^0 momentum in the $\rho^0\pi^+\pi^-$ rest frame.

The experimental angular distributions are obtained as described above for the ρ $(\pi\pi)$ case and are shown for the X(1450) region in fig. 61a,b. The curves corresponding to spin-parities $J^P = 1^-$, 0^+, 1^+ and 2^+ are superimposed on the data. It can be seen that $J^P = 0^+$ can be excluded (χ^2/NDF = 238/15), $J^P = 1^+$ is disfavoured (χ^2/NDF = 22/15) and $J^P = 1^-$ (χ^2/NDF = 11/15) or 2^+ (χ^2/NDF = 8/15) both give an acceptable description of the data.

Table 20: Decay matrix elements for an "a_1"π intermediate state

J^P	L	Matrix Element
1^-	0	$\vec{t}$
0^+	1	$\vec{t}.\vec{P}_1$
1^+	1	$\vec{t}\wedge\vec{P}_1$
2^+	1	$A_{ij}(\vec{t},\vec{P}_1)$

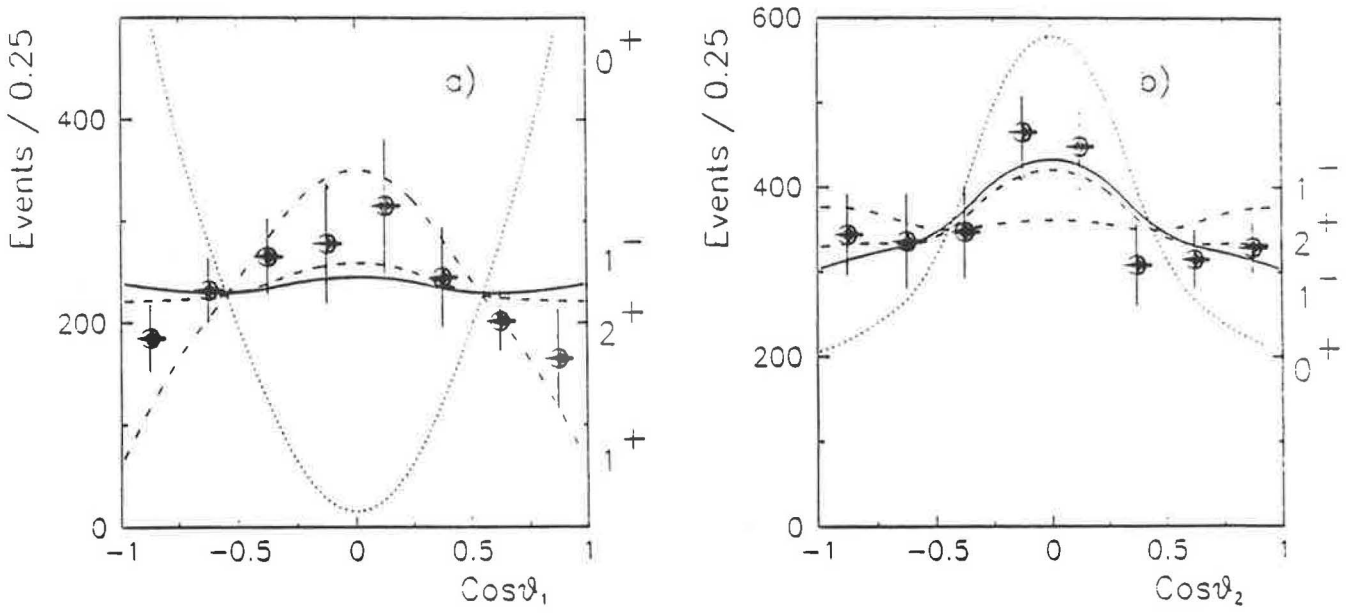

Figure 61: The a) $\cos\theta_1$ and b) $\cos\theta_2$ distributions for the X(1450) region. The superimposed curves are described in the text.

For the $f_1(1285)$ region the $a_1\pi$ $J^P = 1^+$ hypothesis (not shown) gives a poor description of the data, suggesting a ρ^0 $(\pi^+\pi^-)$ decay, in agreement with what has been observed in radiative J/ψ decays [103].

In summary, the peak at 1.28 GeV/c^2 is found to be consistent with a state having $J^P = 1^+$ decaying through a ρ^0 $(\pi^+\pi^-)$ system. For the X(1450), assumed to be isoscalar, $J^P = 1^\pm$ or 2^+ give good descriptions of the data.

8.6 A comparison with the 85 GeV/c data and a calculation of cross sections

Fig. 62 shows the 85 GeV/c $\pi^+\pi^-\pi^+\pi^-$ mass spectrum for the proton incident beam. A clear peak can be seen in the $f_1(1285)$ region but there is very little evidence for structures in the 1.45 and 1.9 GeV/c^2 regions. The spectrum has been fitted with a single Breit-Wigner to describe the $f_1(1285)$ and a background as described above for the 300 GeV/c data.

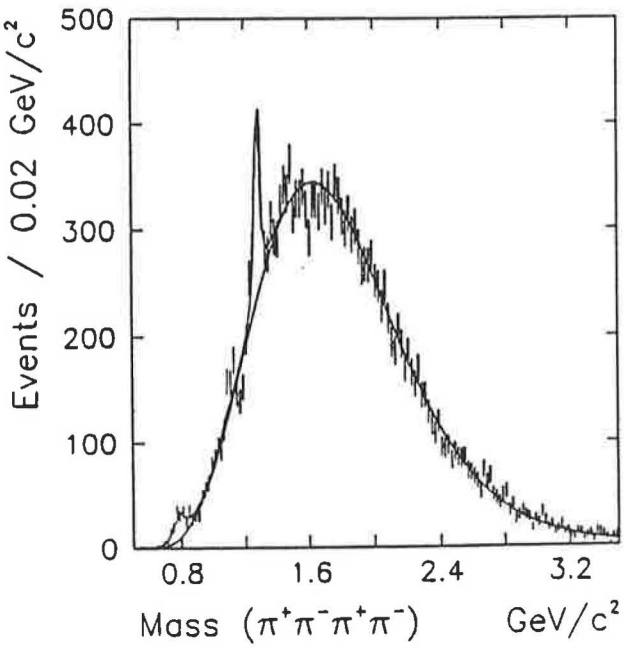

Figure 62: The $\pi^+\pi^-\pi^+\pi^-$ effective mass spectrum for the 85 GeV/c data, with fit.

In order to study the energy dependence of the production of the $f_1(1285)$, X(1450) and X(1900) their cross sections have been calculated at 85 and 300 GeV/c, losses due to geometrical acceptance, selection cuts, detector efficiencies etc. have been calculated as described in chapters 6 and 7. Since there is no evidence for the X(1450) or X(1900) in the 85 GeV/c data only an upper limit on their cross sections can be calculated.

In order to compare the reaction $pp \rightarrow p_f (\pi^+\pi^-\pi^+\pi^-) p_s$ at the two energies, a cut has been placed on the Feynman x of the $\pi^+\pi^-\pi^+\pi^-$ system to select a region in which the acceptance is good for both experiments. The cut used is $|x_F| \leq 0.2$. The cross sections for the $f_1(1285)$ are

$$\sigma(f_1(1285) \rightarrow \pi^+\pi^-\pi^+\pi^-) = 530 \pm 70 \text{ nb} \quad \text{at 85 GeV/c and}$$
$$\sigma(f_1(1285) \rightarrow \pi^+\pi^-\pi^+\pi^-) = 335 \pm 60 \text{ nb} \quad \text{at 300 GeV/c.}$$

This result indicates that the $f_1(1285)$ cross section decreases with incident momentum as was found in the $K^0_S K^{\pm}\pi^{\mp}$ channel.

For the X(1450) and X(1900) the cross sections are

$$\sigma(X(1450) \rightarrow \pi^+\pi^-\pi^+\pi^-) < 145 \text{ nb (95 \% c.l.)} \quad \text{at 85 GeV/c and}$$
$$\sigma(X(1450) \rightarrow \pi^+\pi^-\pi^+\pi^-) = 290 \pm 60 \text{ nb} \quad \text{at 300 GeV/c.}$$

$$\sigma(X(1900) \rightarrow \pi^+\pi^-\pi^+\pi^-) < 140 \text{ nb (95 \% c.l.)} \quad \text{at 85 GeV/c and}$$
$$\sigma(X(1900) \rightarrow \pi^+\pi^-\pi^+\pi^-) = 790 \pm 120 \text{ nb} \quad \text{at 300 GeV/c.}$$

In contrast to the $f_1(1285)$, the cross sections for the X(1450) and X(1900) increase with energy; this behaviour is consistent with a double Pomeron exchange mechanism, which is predicted to be a source of gluonic states.

8.7 A calculation of the $f_1(1285)$ branching ratio

The number of $f_1(1285)$ events in the geometrically acceptance corrected $\pi^+\pi^-\pi^+\pi^-$ and $K^0_S K^\pm \pi^\mp$ mass spectra has been calculated at 300 GeV/c. In order to calculate the branching ratio $(f_1(1285) \rightarrow K\bar{K}\pi)/(f_1(1285) \rightarrow 4\pi)$ corrections have to be applied to account for the unseen decay modes.

For the $K\bar{K}\pi$ case, assuming the decay proceeds via $\delta\pi$, the $f_1(1285)$ has three possible decay modes

$$K^0\bar{K}^0\pi^0$$

$$K^+K^-\pi^0$$

$$K^0K^\pm\pi^\mp$$

The relative fractions for these decay modes are given by the Clebsch-Gordan coefficient of Isospin. The $K^0K^\pm\pi^\mp$ decay constitutes 2/3 of the total decay. The $K^0_S K^\pm \pi^\mp$ decay mode constitutes 1/2 of the $K^0K^\pm\pi^\mp$ decay and the observed decay mode $K^0_S \rightarrow \pi^+\pi^-$ constitutes 68.6 % of the total K^0_S decays. Therefore to calculate the total number of $K\bar{K}\pi$ events the observed number of $K^0_S K^\pm \pi^\mp$ events has to be multiplied by 4.38.

For the 4π case, assuming that the decay proceeds via $\rho\pi\pi$, the $f_1(1285)$ has three possible decay modes

$$\rho^0\pi^+\pi^-$$

$$\rho^+\pi^-\pi^0$$

$$\rho^-\pi^+\pi^0$$

The relative fractions for these decay modes are given by the Clebsch-Gordan coefficient of Isospin, each of which constitutes 1/3 of the total. Therefore to calculate the total number of 4π events the observed number of $\pi^+\pi^-\pi^+\pi^-$ events has to be multiplied by 3.

The branching ratio of the $f_1(1285)$ to 4π and $K\bar{K}\pi$ has been calculated to be

$$(f_1(1285) \rightarrow K\bar{K}\pi)/(f_1(1285) \rightarrow 4\pi) = 0.28 \pm 0.05 .$$

Which is in good agreement with the PDG [42] value of 0.28 ± 0.09.

8.8 Conclusions

An analysis of the $\pi^+\pi^-\pi^+\pi^-$ channel at 300 GeV/c shows evidence for two new structures at 1.45 and 1.9 GeV/c^2 in addition to the well known $f_1(1285)$. The structure at 1.9 GeV/c^2 is found to be produced predominantly when the four-momentum transfers at the slow and fast vertices are small.

A comparison has been made of the ratios of the resonance signals observed in the $\pi^+\pi^-\pi^+\pi^-$ and $K^0_S K^\pm\pi^\mp$ channels at 1.28 and 1.45 GeV/c^2 in two |t| regions. It is found that the ratio for the enhancement at 1.28 GeV/c^2 remains constant with |t| which together with the fact that the masses and widths found in the two channels are consistent leads to the conclusion that the enhancement seen in the $\pi^+\pi^-\pi^+\pi^-$ channel is another decay mode of the $f_1(1285)$ observed in the $K^0_S K^\pm\pi^\mp$ channel.

A similar comparison for the peak in the 1.45 GeV/c^2 region shows a 3σ change in the two |t| regions. This fact together with the fact that the mass of the peak in the $\pi^+\pi^-\pi^+\pi^-$ channel differs by 4σ from that of the peak seen in the $K^0_S K^\pm\pi^\mp$ channel indicates that it is not the $f_1(1420)$ observed in the $K^0_S K^\pm\pi^\mp$ channel.

A channel likelihood fit has been performed on the $\pi^+\pi^-\pi^+\pi^-$ channel using CHAFIT. The results of this analysis show that the $f_1(1285)$ and X(1450) decay to $\rho^0\pi^+\pi^-$. The X(1900) is found to decay equally to $f_2(1270)\pi\pi$ and $a_2\pi$. There is 3.0 ± 0.4 % $\rho^0\rho^0$ production which is small compared to the dominant $\rho^0\rho^0$ decay modes of the $\pi^+\pi^-\pi^+\pi^-$ system in radiative J/ψ decay [102] [103].

An angular analysis has been performed where the $\rho^0\pi^+\pi^-$ decays of the $f_1(1285)$ and X(1450) have been parameterised in terms of quasi two-body final states corresponding to ρ $(\pi\pi)$ and $(\rho\pi)$ π where it is assumed that the $\pi\pi$ and $\rho\pi$ interactions are strong compared to any other interaction.

The peak at 1.28 GeV/c^2 is found to be consistent with a state having $J^P = 1^+$ decaying through a ρ^0 $(\pi^+\pi^-)$ system. For the X(1450), assumed to be isoscalar, $J^P = 1^\pm$ or 2^+ give good descriptions of the data.

The cross section for the centrally produced $f_1(1285)$ decreases with energy. In contrast, the cross sections for the X(1450) and X(1900) increase with energy; this behaviour is consistent with a double Pomeron exchange mechanism, which is predicted to be a source of gluonic states.

9. CONCLUSIONS

Quantum ChromoDynamics (QCD) not only describes how quarks and antiquarks interact to form the standard $q\bar{q}$ mesons but also predicts the existence of glueballs, hybrids and four-quark states. These states are being searched for using several different production mechanisms, one of which is Double Pomeron Exchange (DPE).

This thesis describes a search for these non-$q\bar{q}$ states by studying mesons centrally produced in the reaction

$$pp \rightarrow p_f(X^0)p_s$$

at 300 GeV/c. A study of the centrally produced $\pi^+\pi^-$ spectrum in this experiment, using the presence of the ρ as a measure of the amount of non-DPE type events, suggests that the WA76 data has a large DPE content and by suitable cuts the DPE signal to background can be increased.

There are several non-$q\bar{q}$ candidate states. As was discussed in chapter 2, one of the best is the $\theta/f_2(1720)$ which is observed for the first time in hadronic collisions by experiment WA76. The search for other candidates have been described in chapters 5 to 8 and can be summarised as follows.

In the $K^0_S K^{\pm}\pi^{\mp}$ channel clear $f_1(1285)$ and $f_1(1420)$ signals are seen with masses and widths

$$f_1(1285) \quad m = 1278 \pm 2 \text{ MeV/c}^2 \quad \Gamma = 25 \pm 4 \text{ MeV/c}^2,$$

$$f_1(1420) \quad m = 1429 \pm 3 \text{ MeV/c}^2 \quad \Gamma = 58 \pm 8 \text{ MeV/c}^2.$$

A spin parity analysis shows that both are 1^{++} states. The $f_1(1285)$ is found to decay via $\delta\pi$ while the $f_1(1420)$ is found to decay only to $K^*\bar{K}$, no 0^{-+} wave being required to describe the data. The energy dependence for the production of the $f_1(1285)$ is not the same as that for the $f_1(1420)$ and it is found that the cross section for the $f_1(1420)$ remains constant as a function of incident momentum.

Initially the $E/f_1(1420)$ was thought to be the $s\bar{s}$ isoscalar partner of the $f_1(1285)$ in the 1^{++} nonet. However, as was discussed in chapter 2, the D'(1530) seems to be a better candidate for this state. The fact that it is seen in double exchange processes, such as DPE and $\gamma\gamma^*$ reactions, while it is not observed in peripheral processes and that its cross section remains constant with energy suggests an exotic nature of the E.

Since the mass of the E is too low to be a radial excitation and as a 1^{++} state its mass is too low to be a glueball or hybrid state, a possible explanation is that it is a four-quark state [39] or $K^*\bar{K}$ molecule [40].

The $\phi\phi$ channel is of interest due to the claimed observation of three $J^{PC} = 2^{++}$ states [57] one or more of which could be a glueball. $\phi\phi$ production has been observed in the central region in the reaction $pp \rightarrow p_f (K^+K^-K^+K^-) p_s$ at 300 GeV/c. The $\phi\phi$ mass spectrum shows an accumulation of events near threshold and is similar to that observed in reference [57]. An angular analysis of the $\phi\phi$ system shows that $J^P = 2^+$ is favoured over 0^-, although other waves cannot be ruled out. The cross-sections for $\phi\phi$ production at 85 and 300 GeV/c are the same within errors. This is consistent with the $\phi\phi$ system being produced by a double Pomeron exchange mechanism which predicts that the cross section should remain constant with centre-of-mass energy. Therefore, although the statistics are very limited, the WA76 data is consistent with the hypothesis that the $\phi\phi$ system could contain a gluonic state.

An analysis of the $\pi^+\pi^-\pi^+\pi^-$ channel at 300 GeV/c shows evidence for two new structures at 1.45 and 1.9 GeV/c^2 in addition to the well known $f_1(1285)$. An analysis of the state at 1.45 GeV/c^2 indicates that it is not a $\pi^+\pi^-\pi^+\pi^-$ decay mode of the $f_1(1420)$ or $\iota/\eta(1440)$. The structure at 1.9 GeV/c^2 is found to be produced predominantly when the four-momentum transfers at the slow and fast vertices are small.

A channel likelihood fit has been performed on the $\pi^+\pi^-\pi^+\pi^-$ channel using CHAFIT. The results of this analysis show that the $f_1(1285)$ and X(1450) decay to $\rho^0\pi^+\pi^-$. The X(1900) is found to decay equally to $f_2(1270)\pi\pi$ and $a_2\pi$. There is 3.0 ± 0.4 % $\rho^0\rho^0$ production which is small compared to the dominant $\rho^0\rho^0$ decay modes of the $\pi^+\pi^-\pi^+\pi^-$ system in radiative J/ψ decay [102] [103].

A spin-parity analysis of the $\pi^+\pi^-\pi^+\pi^-$ channel shows that the peak at 1.28 GeV/c^2 is consistent with being a state with $J^P = 1^+$ decaying through a ρ^0 ($\pi^+\pi^-$) system. For the X(1450), assumed to be isoscalar, $J^P = 1^\pm$ or 2^+ give good descriptions of the data.

The cross section for the centrally produced $f_1(1285)$ decreases with energy. In contrast, the cross sections for the X(1450) and X(1900) increase with energy; this behaviour is consistent with a double Pomeron exchange mechanism, which is predicted to be a source of gluonic states.

In conclusion, experiment WA76 is designed to look for non-$q\bar{q}$ states in the central region. There is good evidence that these states exist. The $\theta/f_2(1720)$ appears to be the best glueball candidate and the $E/f_1(1420)$ a good candidate for being a four-quark state. The $\phi\phi$ channel is consistent with there being some gluonic content. Finally in the $\pi^+\pi^-\pi^+\pi^-$ channel the X(1450) and X(1900) are observed for the first time. One or both of these states may have an exotic nature.

APPENDIX A
AN INTRODUCTION TO GAUGE THEORY

A.1 Abelian gauge theory and QED

In the presence of a current density j_μ the electromagnetic field A_μ satisfies [107]

$$\Box^2 A_\mu = j_\mu .$$

Local gauge invariance requires that the Lagrangian of a system be unchanged under

$$\psi(x) \rightarrow e^{(i\alpha(x))}\psi(x)$$

where $\alpha(x)$ depends on space and time in a completely arbitrary way. In order to make the Lagrangian

$$\mathcal{L} = i\,\bar{\psi}\,\gamma\,\delta\psi - m\bar{\psi}\psi$$

invariant under local gauge transformations the derivative D must be modified such that it transforms covariantly under phase transformations, that is, like ψ itself

$$D_\mu\psi \rightarrow e^{(i\alpha(x))}\, D_\mu\psi .$$

To form the covariant derivative D_μ a vector field A_μ has to be introduced which transforms such that the Lagrangian is unaltered. This can be accomplished by the construction

$$D_\mu = \delta_\mu - ieA_\mu$$

where A_μ transforms as

$$A_\mu \rightarrow A_\mu + (1/e)\,\delta_\mu\alpha .$$

Thus, by demanding local phase invariance a vector field A_μ has to be introduced. This is called the gauge field which couples to Dirac particles in exactly the same way as the photon field. Since there is no limit to the distance over which the phases of the electron field might change the gauge field required to cancel these changes must also have an infinite range. This requires the photon to be massless.

Now α can be chosen such that under the transformation

$$A_\mu \rightarrow A'_\mu = A_\mu + (1/e)\,\delta_\mu\alpha \qquad (1)$$

$$\delta_\mu A^\mu = 0$$

which is known as the Lorentz condition.

The wavefunction A^{μ} for a free photon satisfies the equation

$$\Box^2 A^{\mu} = 0$$

which has solution

$$A^{\mu} = \varepsilon^{\mu}(q)e^{(-iqx)} \qquad (2)$$

where the four-vector ε^{μ} is the polarization vector of the photon.

The Lorentz condition $\delta_{\mu}A^{\mu} = 0$, gives

$$q_{\mu}\varepsilon^{\mu} = 0$$

which reduces the number of independent components of ε^{μ} to three.

If the gauge parameter is chosen such that

$$\alpha = i\,be^{(-iqx)} \qquad (3)$$

where b is a constant, then substituting (3) and (2) into (1) shows that the physics is unchanged by the replacement

$$\varepsilon_{\mu} \rightarrow \varepsilon'_{\mu} = \varepsilon_{\mu} + bq_{\mu}$$

In other words, two polarization vectors $(\varepsilon_{\mu},\varepsilon'_{\mu})$ which differ by a multiple of q_{μ} describe the same photon. This degree of freedom may be used to ensure that the time component of ε vanishes. Then the Lorentz condition reduces to

$$\vec{\varepsilon} \cdot \vec{q} = 0 \qquad (4)$$

This noncovariant choice of gauge is known as the Coulomb gauge. As can be seen from (4) there are only two independent polarization vectors and they are both transverse to the three momentum of the photon. A free photon is thus described by its momentum $\vec{q}$ and a polarization vector $\vec{\varepsilon}$. Since $\vec{\varepsilon}$ transforms as a vector it is associated with a particle of spin 1. If $\vec{\varepsilon}$ were along $\vec{q}$, it would be associated with a helicity $-$ zero photon. This state is missing because of the transversality condition (4). It can only be absent because the photon is massless.

A.2 Non−Abelian gauge invariance and QCD

QCD is based on the extension of the above ideas with the U(1) gauge group replaced by the SU(3) group of phase transformations on the quark colour fields. The free Lagrangian is [108]

$$\mathscr{L} = \bar{q}_j (i \gamma^\mu \delta_\mu - m) q_j \qquad (5)$$

where q_1, q_2, q_3 denote the three colour fields.

Again the Lagrangian is required to be invariant under local phase transformations of the form

$$q(x) \rightarrow Uq(x) = \exp(i\alpha_a(x)T_a)\, q(x)$$

where U is an arbitrary 3×3 unitary matrix and a summation over the repeated suffix a is implied. T_a, with a = 1,....8, are a set of linearly independent traceless 3×3 matrices, and α are the group parameters.

The group is non-Abelian since not all the generators T commute with each other. The commutation relation is

$$[T_a,T_b] = i f_{abc}T_c \qquad (6)$$

where f_{abc} are real constants, called the structure constants of the group.

To impose SU(3) local gauge invariance on the QCD Lagrangian (5) the steps used in the QED example are followed. It is sufficient to consider infinitesimal phase transformations,

$$q(x) \rightarrow [1 + i\, \alpha_a(x)T_a]\, q(x)$$

$$\delta_\mu q \rightarrow (1 + i\, \alpha_a T_a)\, \delta_\mu q + iT_a q \delta_\mu \alpha_a$$

where the last term spoils the invariance of $\mathscr{L}$. If the QED analogue is used eight gauge fields $G_\mu{}^a$ must be introduced each transforming as

$$G_\mu{}^a \rightarrow G_\mu{}^a - (1/g)\delta_\mu \alpha_a$$

and a covariant derivative of the form

$$D_\mu = \delta_\mu + igT_a G_\mu{}^a .$$

However, for a non−Abelian gauge transformation, this is not enough to produce a gauge invariant Lagrangian. The problem is that

$$(\bar{q}\gamma^\mu T_a q) \rightarrow (\bar{q}\gamma^\mu T_a q) + i\alpha\bar{q}\gamma^\mu(T_aT_b - T_bT_a)q \rightarrow (\bar{q}\gamma^\mu T_a q) - f_{abc}\alpha_b(\bar{q}\gamma^\mu T_c q)$$

where the commutation relation (6) has been used.

However, gauge invariance of $\mathscr{L}$ can be achieved provided that

$$G_\mu{}^a \rightarrow G_\mu{}^a - (1/g)\,\delta_\mu\alpha_a - f_{abc}\alpha_b G_\mu{}^c$$

and a gauge invariant kinetic energy term for each of the G fields is introduced. The final gauge invariant QCD Lagrangian is

$$\mathscr{L} = \bar{q}(i\,\gamma^\mu\delta_\mu - m)\,q - g\,(\bar{q}\,\gamma^\mu T_a q)\,G_\mu{}^a - (1/4)G_\mu{}^a{}_\nu G^\mu{}_a{}^\nu$$

This equation is the Lagrangian for interacting coloured quarks q and vector gluons G_μ, with coupling specified by g, which follows from demanding that the Lagrangian be invariant under local colour phase transformations to the quark fields. Since the phase of the three quark colour fields can be arbitrarily varied it is not surprising that eight vector gluon fields ($G_\mu{}^a$ with $a = 1,....,8$) are needed to compensate all possible phase changes. Just as for the photon, local gauge invariance requires the gluons to be massless.

The field strength tensor $G_\mu{}^a{}_\nu$ has a remarkable new property on account of the extra term in the Lagrangian. Imposing the gauge symmetry has required that the kinetic energy term in $\mathscr{L}$ is not purely kinetic but includes an induced self−interaction between the gauge bosons which arises because the gluons themselves carry colour.

APPENDIX B

SPIN AND PARITY OF GLUEBALLS AND HYBRID STATES

B.1 An introduction to the MIT bag model

The following calculations are made using the MIT bag model [109] in which gluonic hadrons are made by populating the modes of the gluon field in a cavity obeying the bag boundary conditions necessary to ensure confinement [22].

To calculate the spin dependent forces between gluons using the bag model, the free wave equation has to be solved:−

$$\Box^2 G_\mu = 0 \quad \text{inside,}$$

$$G_\mu = 0 \quad \text{outside,}$$

where G_μ is the gluon gauge field (see appendix A). The solutions in a spherical cavity turn out to be the TE and TM cavity resonance modes where the E and M refer to the colour electric and colour magnetic fields.

B.2 Tensor method for gluon couplings

The tensor method consists of writing down explicitly the S−matrix element for the process under consideration in terms of the tensors relevant to the problem. In the production of a glueball from two gluons, there are two polarization vectors $\vec{\epsilon}_1$ and $\vec{\epsilon}_2$ of the two gluons, their momentum vectors $\vec{k}_1$ and $\vec{k}_2$ and the momentum $\vec{K}$ and polarization $\vec{\epsilon}$ of the glueball.

In order to calculate the allowed angular momentum states the following steps must be considered.

1. The rest frame of the glueball is chosen as the frame of reference. This means that $\vec{K} = 0$ and $\vec{k_1} = -\vec{k_2} = \vec{k}$

2. The Coulomb gauge is chosen so that,

$$\vec{k_1}.\vec{\varepsilon_1} = \vec{k_2}.\vec{\varepsilon_2} = 0 ,$$

which states that massless vector gluons can only exist in a transverse mode.

3. The glueball produced must be a colour singlet since only colour singlet states are invariant under rotations in colour space.

4. By gauge invariance if $\vec{\varepsilon} \leftrightarrow \vec{k}$ then the expression must vanish. That is, as $k \simeq \delta$, if the transformation $\vec{\varepsilon} \rightarrow \vec{k}$ is made then $\varepsilon G \rightarrow \delta G$ is equal to zero by Lorentz invariance.

5. From the Wigner-Eckart theorem the matrix element of tensor operators with respect to angular momentum eigenstates satisfies

$<\alpha' j' m' | T | \alpha j m> = <jkmq|jkj'm'> . <\alpha' j' \| T_a \| \alpha J> / \sqrt{(2j+1)}$.

Since $<\alpha' j' \| T_a \| \alpha j>$ is a matrix element it is a scalar and therefore its components must produce a scalar. In this case the projection operator is considered, that is when $j = j'$ [110], and this means that for example a vector operator will produce a vector glueball state.

As the gluons are confined by the same mechanism that confines quarks, bag model calculations may be used on the glueball states. The lowest state solutions are given by [111]

$$TE = |k|\vec{\varepsilon} \text{ with } J^P = 1^+$$

and

$$TM = \vec{k} \wedge \vec{\varepsilon} \text{ with } J^P = 1^-$$

and the allowed matrix operators are made up of these two.

B.3 Spin zero case

There are three combinations of the two field operators TE and TM that can be used to produce a scalar under rotations. These are

$$TE_1.TE_2 = |k|^2\ \vec{\varepsilon}_1.\vec{\varepsilon}_2 \quad (1)$$

and

$$TM_1.TM_2 = (\vec{k}\wedge\vec{\varepsilon}_1).(\vec{k}\wedge\vec{\varepsilon}_2) \quad (2)$$

and

$$TE_1.TM_2 = |k|\vec{\varepsilon}_1.(\vec{k}\wedge\vec{\varepsilon}_2) \quad (3)$$

The rules above can now be applied to these states.

B.3.1 $TE_1.TE_2$

This is the dot product between two vectors which satisfies the rules and produces a 0^{++} state.

B.3.2 $TM_1.TM_2$

This is the dot product between two pseudovectors which satisfies the rules and again produces a 0^{++} state.

B.3.3 $TE_1.TM_2$

This is the dot product between a vector and a pseudovector it again satisfies all the rules and produces a 0^{-+} state.

B.4 Spin one case

To produce a spin one glueball from two gluons requires one of the following combinations of field operators

$$TE_1 \wedge TM_2 = |k|\vec{\varepsilon}_1 \wedge (\vec{k} \wedge \vec{\varepsilon}_2) \quad (4)$$

$$TM_1 \wedge TM_2 = (\vec{k} \wedge \vec{\varepsilon}_1) \wedge (\vec{k} \wedge \vec{\varepsilon}_2) \quad (5)$$

$$TE_1 \wedge TE_2 = |k|^2 (\vec{\varepsilon}_1 \wedge \vec{\varepsilon}_2) \quad (6)$$

Again the rules for formation of these states can be applied.

B.4.1 $TE_1 \wedge TM_2$

$$|k|\vec{\varepsilon}_1 \wedge (\vec{k} \wedge \vec{\varepsilon}_2) = (\vec{\varepsilon}_1 . \vec{\varepsilon}_2)\vec{k} - (\vec{k} . \vec{\varepsilon}_1)\vec{\varepsilon}_2 \quad (7)$$

1. Due to the transverse nature of gluons, rule (2), the second term is zero

2. Due to Bose symmetry the wavefunction of two identical bosons must be symmetric under interchange. Now although gluons have a colour degree of freedom, rule (3) requires a physical glueball to be in a colour singlet state which removes this colour degree of freedom. This means that the state must be symmetric under $\vec{\varepsilon}_1 \leftrightarrow \vec{\varepsilon}_2$ and $\vec{k} \rightarrow -\vec{k}$. However the first term in (7) changes sign under interchange and thus is not allowed by Bose symmetry.

Therefore the $TE_1 \wedge TM_2$ state that would represent a 1^{-+} state is not allowed.

B.4.2 $TM_1 \wedge TM_2$

$$(\vec{k} \wedge \vec{\varepsilon}_1) \wedge (\vec{k} \wedge \vec{\varepsilon}_2) = ((\vec{k} \wedge \vec{\varepsilon}_1) . \vec{\varepsilon}_2)\vec{k} - ((\vec{k} \wedge \vec{\varepsilon}_1) . \vec{k})\vec{\varepsilon}_2 \quad (8)$$

1. $\vec{k} \wedge \vec{\varepsilon}_1$ is perpendicular to k therefore the second term in (8) is zero due to the transverse nature of gluons.

2. The first term can be rewritten as

$$(-(\vec{k} \wedge \vec{\varepsilon}_2) . \vec{\varepsilon}_1)\vec{k} \quad (9)$$

Under Bose symmetry the first term is

$$((-\vec{k} \wedge \vec{\varepsilon}_2) . \vec{\varepsilon}_1)(-\vec{k}) = (\vec{k} \wedge \vec{\varepsilon}_2) . \vec{\varepsilon}_1)\vec{k}$$

which is opposite in sign to the rearranged term shown in (9). Therefore the first term is zero by Bose symmetry.

Therefore the $TM_1 \wedge TM_2$ state that would represent a 1^{++} state is not allowed.

B.4.3 $TE_1 \wedge TE_2$

This state is again ruled out by Bose symmetry. Therefore the $TE_1 \wedge TE_2$ state that would represent a 1^{++} state is not allowed.

B.4.4 Conclusion

Therefore it appears that it is not possible to produce a spin one glueball from two gluons. This is not surprising since Yang's theorem [34] states that a $J = 1$ state can not be produced from two transversely polarised massless vector particles.

B.5 Spin two case

To produce a spin two glueball from two gluons requires using the outer or tensor product between the individual gluon modes denoted by $\otimes$.

$$TE_1 \otimes TM_2 = |k|\vec{\varepsilon_1} \otimes (\vec{k} \wedge \vec{\varepsilon_2}) \quad (10)$$

$$TM_1 \otimes TM_2 = (\vec{k} \wedge \vec{\varepsilon_1}) \otimes (\vec{k} \wedge \vec{\varepsilon_2}) \quad (11)$$

$$TE_1 \otimes TE_2 = |k|^2 (\vec{\varepsilon_1} \otimes \vec{\varepsilon_2}) \quad (12)$$

None of these states are excluded and they produce glueballs states as follows:-

$TE_1 \otimes TM_2$ $\quad 2^{-+}$

$TM_1 \otimes TM_2$ $\quad 2^{++}$

$TE_1 \otimes TM_2$ $\quad 2^{++}$

APPENDIX C

KINEMATIC VARIABLES AND REGGE THEORY

C.1 Feynman x (x_F)

The Feynman x (x_F) of a particle is a dimensionless variable defined as

$$x_F = P_L/P$$

which measures, in the centre-of-mass, the fraction of the beam's momentum (P) which is contained in the longitudinal momentum (P_L) of the detected particle. P is defined as

$$P = \frac{\sqrt{(\Lambda(s, M^2_c, M^2_{min})}}{2\sqrt{s}}$$

where M_c is the mass of the particle, M_{min} is the mass of the lightest system which can recoil against particle c, $\sqrt{s}$ is the centre-of-mass energy and

$$\Lambda(a, b, c) = a^2 + b^2 + c^2 - 2ab - 2ac - 2bc.$$

C.2 Rapidity (y)

Another variable that is used to display the P_L dependence of a reaction is rapidity (y) [112], defined by

$$y = 0.5 \text{ Log } ((E + P_L)/(E - P_L))$$

where E is the energy of the particle.

y depends on the choice of frame, but it has the advantage of being additive under Lorentz boosts along the z axis. If a frame is boosted by a velocity u such that

$$E \rightarrow \gamma(E + uP_L)$$

$$P_L \rightarrow \gamma(P_L + uE)$$

where $\gamma \doteq \sqrt{(1-u^2)}$ then

$$y \rightarrow y + 0.5\,\mathrm{Log}((1+u)/(1-u)) = y + y_{boost}$$

C.3 The Mandelstam variables and WA76

For the reaction

$$p_b p_t \rightarrow p_f (X^0)\, p_s,$$

where b, t, f, s refer to the beam, target, fast and slow protons respectively, the total centre-of-mass energy squared

$$s = (P^{\mu}_b + P^{\mu}_t)^2$$

and the four-momentum transfer squared at the slow and fast vertex respectively is given by

$$t_{fast} = t_1 = (P^{\mu}_f - P^{\mu}_b)^2$$

$$t_{slow} = t_2 = (P^{\mu}_s - P^{\mu}_t)^2.$$

C.4 Double exchange processes

The expression for the observed cross section for Double Pomeron Exchange (DPE) [83] in the reaction

$$AB \rightarrow AB + X\,,$$

is given by

$$\frac{d\sigma DPE}{dt_1 dt_2 d(M_1^2/s) d(M_2^2/s)} = \gamma_P(t_1)\gamma_P(t_2) \left(\frac{(M_1^2)}{(s)}\right)^{1-2\alpha(t_1)} \left(\frac{(M_2^2)}{(s)}\right)^{1-2\alpha(t_2)} \sigma_{PP}(M^2,t_1,t_2)$$

while the single diffractive background (BGND) is given by

$$\frac{d\sigma BGND}{dt_1 dt_2 d(M_1^2/s) d(M_2^2/s)} = \gamma_P(t_1)\gamma_R(t_2) \left(\frac{(M_1^2)}{(s)}\right)^{1-2\alpha(t_1)} \left(\frac{(M_2^2)}{(s)}\right)^{1-2\beta(t_2)} \sigma_{RP}(M^2,t_1,t_2)$$

where the subscript R stands for all the leading Regge trajectories, $\alpha(t) = \alpha p(t)$ and $\beta(t) = \alpha_R(t)$.

A standard practice is to approximate the Pomeron-Pomeron cross section by the leading Regge behaviour, so that it is related to the Triple Regge couplings calculated in inclusive channels. That is assume that the Pomeron-Pomeron vertex couples to form a single trajectory as shown in fig. 63.

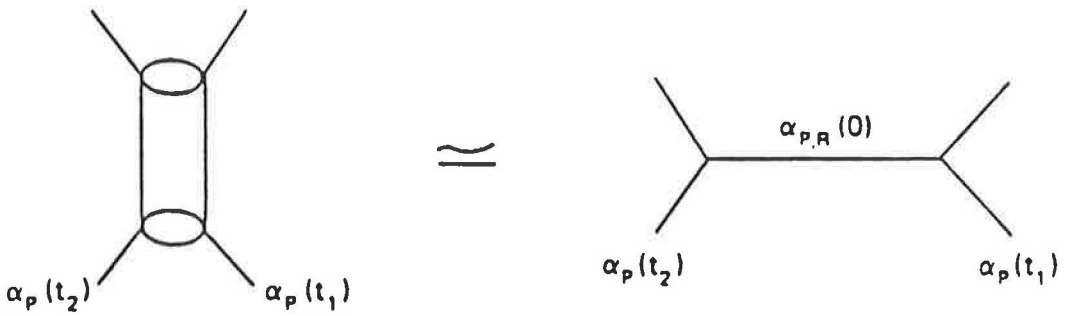

Figure 63: An example of a Triple Regge coupling.

Then

$$\frac{d\sigma DPE}{dt_1 dt_2 d(M_1^2/s) d(M_2^2/s)} = Gppp(t_1)Gppp(t_2) \frac{(M_1^2)^{1-2\alpha(t_1)}}{(s)} \frac{(M_2^2)^{1-2\alpha(t_2)}}{(s)} (1/\sigma^P{}_{pp})$$

where G_{ppp} is the triple Pomeron coupling and $\sigma^P{}_{pp}$ is the Pomeron contribution to the proton proton total cross section ($\approx$ 40mb). The PPR term has been neglected since it is much smaller than the PPP term.

Using the same formalism for the background events gives

$$\frac{d\sigma^{BGND}}{dt_1 dt_2 d(M_1^2/s) d(M_2^2/s)} = G_{ppp}(t_1) G_{RRP}(t_2) \frac{(M_1^2)^{1-2\alpha(t_1)}}{(s)} \frac{(M_2^2)^{1-2\beta(t_2)}}{(s)} (1/\sigma^{P}_{pp})$$

where the coupling factors (G) and the Regge trajectories (α) come from measurements of exclusive data where they are found to be :-

$$G_{ppp}(t) = A_p \exp(B_p t) = 6.2\exp(7.9t)$$

$$\alpha_P(t) = 1 + 0.25t$$

$$G_{RRP}(t) = A_R \exp(B_R t) = 200\exp(4.6t)$$

$$\alpha_R(t) = 0.2 + 0.5t$$

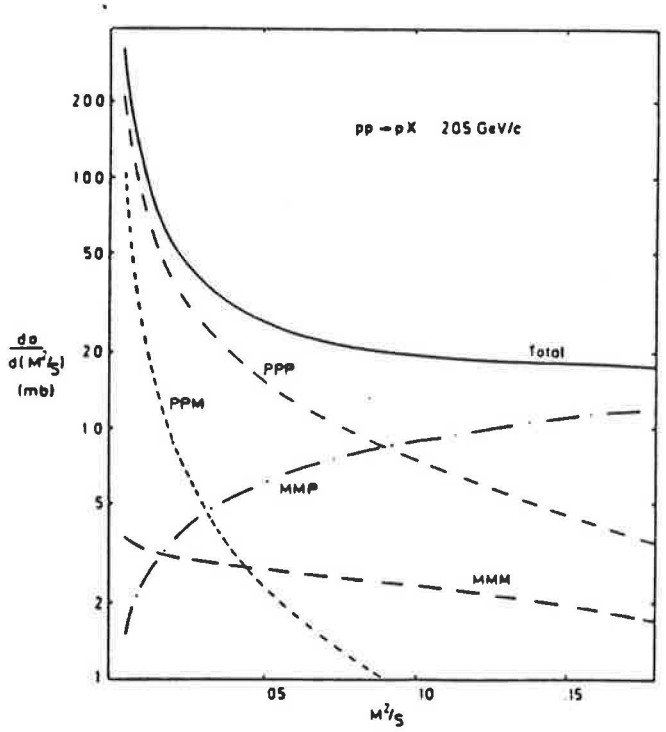

Figure 64: The coupling coefficients G integrated over t for P = 205 GeV/c.

Fig. 64 shows the coupling coefficients G integrated over t for P = 205 GeV/c. For $(M^2/s) < 0.05$ the G_{ppp} coupling is dominant over G_{RRP} and hence the DPE signal is dominant over the background. For P = 300 GeV/c, $(M^2/s) < 0.1$ is required for DPE to be dominant.

It can be shown that [113],

$$|x_A| \approx 1 - M^2_{XA}/s,$$

where M_{XA} is the missing mass with respect to the proton "A" and s is the total c.m. energy squared. Also in reference [114] it is shown that

$$M^2 = s(1-|x_B|)(1-|x_A|)$$

where M is the effective mass of the centrally produced system. From the coupling factors (G) a preliminary definition of a "double Pomeron event" is one where $M^2/s < 0.1$. Therefore for a reaction of the type $AB \rightarrow AXB$ in terms of the Feynman x of the outgoing particles A and B, a definition of a DPE event is one for which $1-|x_A| \leq 0.1$ and $1-|x_B| \leq 0.1$

The variables Z_1 and Z_2 where

$$Z = \log(1-|x|)$$

are such that

$$Z_1 + Z_2 = \log(s) - \log(M^2).$$

and hence Z_1 and Z_2 span a triangular region of phase space which expands with increasing total energy. Now for the "double Pomeron events" which have been defined to have $x \geq 0.9$ corresponding to $Z \geq 2.3$, this means that as s increases the region of possible DPE events expands and thus the conditions for observing DPE become more favourable.

For a constant value of x_1, x_2

$$\frac{\sigma(\text{DPE})}{\sigma(\text{BGND})} = (1-x)^{-1.6-0.5|t|} e^{-3.3|t|}$$

Hence DPE is dominant at low |t|.

APPENDIX D
ERRORS AND LIKELIHOOD FUNCTIONS

D.1 Calculation of errors on masses, widths and number of events

To calculate the error on a parameter resulting from a fit to a spectrum the EQ method[5] has been used. The original spectrum is fitted and the parameters of the fit are determined. Each bin of the histogram is then changed by a random amount according to Poisson statistics so as to generate a new histogram. This procedure is repeated fifty times to produce fifty histograms. Each histogram is then fitted with the parameters obtained from the original spectrum used as starting values. A histogram of the variation of each parameter is made and the standard deviation of the resulting spectrum is calculated and is used as the error on the parameter.

D.2 Calculation of errors on weighted events

To calculate the error on a histogram bin whose contents have been multiplied by a weighting factor the following method has been used. Consider a bin whose contents before weighting is N events and after weighting the contents is X such that,

$$X = \Sigma W_i = N\langle W \rangle$$

where W_i is the weight on event i and $\langle W \rangle$ is the mean weight on the bin.

The error on X can come from two sources :-

1. fluctuations in the number of entries in the bin (N)

2. fluctuations in the distribution of W_i

---

[5] Named after Emanuele Quercigh who suggested this method to the author.

If these are independent then,

$$(\sigma_X/X)^2 = (\sigma_N/N)^2 + (\sigma_{W'}/<W>)^2$$

where

$$\sigma_N = \sqrt{(N)}$$

and $\sigma_{W'}$ is the error on the mean value of W, which is the standard error on the W distribution itself, i.e.

$$\sigma_{W'} = (\sigma_W)/\sqrt{(N)}$$

where σ_W is the width of the W distribution. Then,

$$(\sigma_X/X)^2 = 1/N + (\sigma_W)^2/N<W>^2$$

so that

$$(\sigma_X)^2 = N<W>^2 + N\sigma_W^2$$

but

$$\sigma_W^2 = <W^2> - <W>^2$$

therefore

$$(\sigma_X)^2 = N<W^2> = \Sigma W_i^2$$

Hence the error on a bin is given by the square root of the sum of the weights squared in that bin.

D.3 Maximum likelihood methods

Often in experiments an observation is made of a quantity "x" which is related to some parameter "a" by a probability distribution P(a,x). That is, the probability of observing an event with x in the range dx is given by

$$P(a,x)\,dx$$

where P(a,x) is normalised such that

$$\int P(a,x)\,dx = 1.$$

The problem is to estimate the parameter a from the observation of x.

One method is to use a least squares fitting procedure. This requires formulating the data into a function of a, which can then be fitted. The simplest way of doing this is to divide the range of x into a definite set of bins, however the choice of bin size is arbitrary.

A method which avoids the question of binning is the method of moments. From the expression P(a,x) the various moments may be calculated from

$$F_n(a) = \int x^n P(a,x)\, dx .$$

If an experiment consists of N observations of x yielding x_i then

$$F_n = \sum_{i=1}^{N} x_i^n / N .$$

Then equating the experimental and "theoretical" moments gives N equations for a. The problem is to decide which one gives the best estimate of a.

To overcome these difficulties Fisher proposed the maximum likelihood method in 1912 [115]. From the distribution P(a,x) the quantity

$$L(a) = \prod_{i=1}^{N} P(a,x_i)$$

is formed, where the x_i's are the events observed in an experiment. Then L(a), called the likelihood function, is the probability that an experiment produces the events x_i assuming "a" to be the correct value for the parameter. The likelihood method consists of choosing as the best estimate of a the value which maximises L(a).

In practice it is often more convenient to deal with log(L(a)) rather than L(a). As they both attain their maximum at the same value of a, either may be used to predict the value corresponding to the maximum likelihood. However,

$$\mathcal{L}(a) = \log(L(a)) = \sum \log(P(a,x_i))$$

is much easier to deal with than the large product which makes up L(a).

In the asymptotic limit, the sum gets replaced by an integral: $\Sigma \rightarrow \int(dx\ N\ P(\alpha,x)$, where α is the true value of a. The log likelihood[6] then becomes

$$\mathcal{L}(a) = N \int dx\ P(\alpha,x) \log(P(a,x))$$

and

$$d\mathcal{L}(a)/da = N \int dx\ P(\alpha,x)/P(a,x)\ \delta P(a,x)/\delta a\ .$$

Evaluating at $a = \alpha$ gives

$$d\mathcal{L}(a)/da|_{a=\alpha} = N \int dx\ \delta P(a,x)/\delta a|_{a=\alpha}$$

and since $\int P(a,x)\ dx = 1$ by normalisation the integral of the derivative with respect to a vanishes. Therefore

$$d\mathcal{L}/da|_{a=\alpha} = 0\ .$$

and the likelihood has a turning point (a maximum) at $a = \alpha$. Hence the location of the maximum is an estimator of the true value of the parameter a.

In the discrete regime it can be shown [94] that the expectation value of the estimate of the parameter obtained at the maximum is equal to the true value of the parameter.

D.3.1 The goodness of the fit

The likelihood function, L(a), is a peculiar function in that it is difficult to interpret its size. The more events there are in an experiment the greater the value of L(a), but there is no relation between the size of L(a) and the goodness of fit as there is with a χ^2 method. However it can be shown [94] that when the likelihood function $\mathcal{L}(a)$ is parabolic (i.e. the likelihood varies as $1/2(a-\alpha)^2$) then the value of $\mathcal{L}$ falls by 1/2 a unit from its maximum one sigma above and below the central estimate. It is also shown in reference [94] that any parameterisation can be transformed so as to obtain a parabolic likelihood and since the likelihood is invariant, the value of $\mathcal{L}$ will fall by 1/2 a unit for any parameterisation one sigma above or below the central estimate.

---

[6] Usually the word log will be omitted.

APPENDIX E

CHARGE CONJUGATION AND G PARITY STATES IN A DALITZ PLOT ANALYSIS

Consider an arbitrary amplitude A describing the state $K\bar{K}\pi$. This can be expanded in terms of the orbital angular momentum of the $K\bar{K}$ subsystem :

$$A = \sum_{\ell} a_\ell \psi_\ell(K\bar{K})$$

where particle K has momentum $+\vec{k}$ and particle $\bar{K}$ has momentum $-\vec{k}$ in the $K\bar{K}$ centre-of-mass system.

If B is the amplitude describing $K \leftrightarrow \bar{K}$ then,

$$B = \sum_{\ell} a_\ell \psi_\ell(\bar{K}K)$$

$$= \sum_{\ell} (-1)^\ell a_\ell \psi_\ell(K\bar{K})$$

where the second line is derived from the property of the spherical harmonics.

Two orthogonal wave functions $\Psi_{\pm}$ can now be formed that describe whether the $K\bar{K}\pi$ state is even or odd under $K \leftrightarrow \bar{K}$ exchange,

$$\Psi_+ = (A+B)/2 = \sum_{\ell = \text{even}} a_\ell \psi_\ell(K\bar{K})$$

$$\Psi_- = (A-B)/2 = \sum_{\ell = \text{odd}} a_\ell \psi_\ell(K\bar{K})$$

A neutral $K\bar{K}\pi$ system can be formed in two ways, either as $(K\bar{K})^0\pi^0$ or $(K\bar{K})^{\pm}\pi^{\mp}$. In this case we are interested in the charged $K\bar{K}$ system which necessarily has I = 1. The G parity is defined as

$$G = (-1)^{\ell + S + I}$$

where S = 0 for a dikaon system and I = 1. The G-parity of a π is negative so that

$$G\Psi_{\pm} = \pm\Psi_{\pm}$$

that is, a neutral $K\bar{K}\pi$ state with a charged π has G-parity $+1$ (-1) if the wavefunction is even (odd) under $K \leftrightarrow \bar{K}$ interchange. Note that this result holds irrespective of whether the $K\bar{K}\pi$ system undergoes a sequential decay.

To construct a complete wavefunction for the $K\bar{K}\pi$ decay via an intermediate $I = 1/2$ K^* the two positive strangeness K^* states are considered first,

$$K^{*+} = \sqrt{(2/3)}\pi^+K^0 - \sqrt{(1/3)}\pi^0K^+$$

$$K^{*0} = \sqrt{(1/3)}\pi^0K^0 - \sqrt{(2/3)}\pi^-K^+$$

the wavefunction of a neutral $K\bar{K}\pi$ system with isospin I (0 or 1) is then,

$$A_I = \sqrt{(1/2)}(K^{*+}K^- - (-1)^I K^{*0}\bar{K}^0)$$

The wavefunction B_I for the negative strangeness K^*'s is formed from A_I by $K \leftrightarrow \bar{K}$ interchange.

Then the total wavefunction for the $K\bar{K}\pi$ system can be defined as

$$\Phi_g = \sqrt{(1/2)}(A_I + gB_I) = \Gamma_g + \Theta_g$$

where $g = \pm 1$ and

$$\Gamma_g = \sqrt{(1/6)}((\pi^+K^0)K^- + g((\pi^+K^-)K^0) + (-1)^I((\pi^-K^+)\bar{K}^0 + g(\pi^-\bar{K}^0)K^+))$$

$$\Theta = -\sqrt{(1/12)}(((\pi^0K^+)K^- + g(\pi^0K^-)K^+) + (-1)^I((\pi^0K^0)\bar{K}^0 + g(\pi^0\bar{K}^0)K^0))$$

In this analysis only charged π's have been used, therefore the important term is Γ_g and

$$G\Gamma_g = g\Gamma_g$$

that is a neutral $K\bar{K}\pi$ system with a charged π has a G-parity g.

In the analysis of the $K^0K^{\pm}\pi^{\mp}$ channel there are two ways of combining the two samples.

$$s_1 = M^2(\pi^+K^0),\ s_2 = M^2(\pi^+K^-)$$

$$s_3 = M^2(\pi^-K^+),\ s_4 = M^2(\pi^-\bar{K}^0)$$

and thus two ways of representing the data on a Dalitz plot:

1. Respecting the strangeness of the states and plotting $s_1(s_3)$ versus $s_2(s_4)$.

2. Or by respecting the net charge of the states, i.e. neutral or charged and plotting $s_1(s_4)$ versus $s_2(s_3)$.

To consider the differences between these two methods a general amplitude for the two data samples separately must be formed. From the expression for Γ_g,

$$\phi^+{}_g = (\pi^+K^0)K^- + g(\pi^+K^-)K^0$$

$$\phi^-{}_g = (\pi^-K^+)\bar{K}^0 + g(\pi^-\bar{K}^0)K^+$$

where the superscripts designate the π^+ and π^- charge states.

Assuming that both charge states produce the same admixture of G-parity eigenstates then,

$$\phi^+ = a\phi^+{}_+ + b\phi^+{}_-$$

$$\phi^- = a\phi^-{}_+ + b\phi^-{}_-$$

where a and b are two arbitrary complex numbers.

Respecting the strangeness of the states is equivalent to equating

$$Y = (\pi^+K^0)K^- = (\pi^-K^+)\bar{K}^0$$

$$X = (\pi^+K^-)K^0 = (\pi^-\bar{K}^0)K^+$$

substituting these gives

$$\phi^+ = a(X+Y) + b(X-Y)$$

$$\phi^- = a(X+Y) + b(X-Y)$$

and hence the wave function for the two charged samples is the same.

If the charge of the $K\pi$ combinations is respected then

$$X = (\pi^+K^0)K^- = (\pi^-\bar{K}^0)K^+$$

$$Y = (\pi^+K^-)K^0 = (\pi^-K^+)\bar{K}^0$$

which leads to

$$\phi^+ = a(X+Y) + b(X-Y)$$

$$\phi^- = a(X+Y) - b(X-Y)$$

In this case the two terms are different.

The difference between the two approaches can now be seen.

1. If the strangeness of the states is respected then the two amplitudes are the same, this has the effect that any background terms e.g. Incoherent K^* production etc are entered equally on the Dalitz plot. This is not the case if the charge is respected, here these events show up as an asymmetry in the Dalitz plot projections.

2. When the two charged samples are combined the observed distribution is,

$$|\phi|^2 = |\phi^+|^2 + |\phi^-|^2$$

this means that if the charge of the states is respected the interference term a^*b cancels which is not the case if the strangeness is respected. The interference term is important if there are two G-parity states present and one of the states is much weaker than the other. However if the amplitudes are correctly normalised although the interference term between two G-parity states will not be seen the individual states themselves will be seen.

REFERENCES

[1] M. Gell-Mann, Phys. Lett. **8** (1964) 214.

[2] G. Zweig, CERN/TH 401 (1964).

[3] P.D.B. Collins and A.D. Martin, Hadron Interactions, Adam Hilger Press, 1984.

[4] M. Benayoun et al., Phys. Lett., **198B** (1987) 281.

[5] L. Kopke and N. Wermes, CERN-EP/88-93 (1988).
Submitted to Physics Reports.

[6] G. Eigen, Proceedings of the Int. School of Physics with low energy antiprotons-2nd course: Spectroscopy of light and heavy quarks, Erice 23-31 May 1987.

[7] T. Akesson et al., Nucl. Phys. **B264** (1986) 154.

[8] A. Breakstone at al., Z. Phys. **C27** (1985) 205.

[9] G. Vassiliadis et al., Proceedings of the International Conference on Hadron Spectroscopy, University of Maryland, 20-22 April, 1985.

[10] F.E. Close, RL-82-041 (1982).

[11] J.F. Donoghue, Univ. of Mass. preprint UMHEP-157 (1981).

[12] J.F. Donoghue et al., Phys. Lett. **99B** (1981) 416.
M. Chanowitz and S. Sharpe, Nucl. Phys. **B222** (1983) 211.

[13] C.E. Carlson, WM 84-10 (1984).

[14] P. de Forcrand et al., Phys. Lett. **152B** (1985) 107.

[15] N. Isgur and J. Paton, Phys. Rev. **D31** (1985) 2910.

[16] G. Schierholz, Proceedings of the Workshop on Glueballs, Hybrids and Exotics, BNL, August 1988.
S. Sharpe, Proceedings of the Workshop on Glueballs, Hybrids and Exotics, BNL, August 1988.

[17] N. Isgur, Proceedings of the Workshop on Glueballs, Hybrids and Exotics, BNL, August 1988.

[18] F.E. Close, Rep. Prog. Phys. **51** (1988) 833.

[19] B.A. Li et al., Phys. Rev. **D35** (1987) 1070.

[20] J.L. Rosner et al., Phys. Rev. **D24** (1981) 1347.

[21] S. Okuba, Phys. Lett. **5** (1963) 165.

G. Zweig, CERN/TH 401,402,412 (1964).

J. Iizuka, Prog. Theor. Phys. Suppl. **37-38** (1966) 21.

[22] R.L. Jaffe and K. Johnson, Phys.Lett **60B** (1976) 201.

[23] S. Cooper, SLAC-PUB-4139, (1986).

B. Diekmann, CERN-EP/86-112, (1986).

S. Meshkov, Proc. Aspen winter particle Phys. Conf. (1986) 247.

A. Palano, CERN-EP/87-92 (1987).

W. Toki, Proceedings of the Workshop on Glueballs, Hybrids and Exotics, BNL, August 1988.

[24] M.S. Chanowitz, Proceedings of the Second Int. Conf. on Hadron Spectroscopy 16-18 April 1987, KEK, Tsukuba, Japan.

[25] A. Ando et al., Phys. Rev. Lett. **57** (1986) 1296.

[26] A. Birman et al., Phys. Rev. Lett. **61** (1988) 1557.

M.G. Rath et al., Phys. Rev. Lett. **61** (1988) 802.

[27] D. Scharre et al., Phys. Lett. **97B** (1980) 329.

[28] C. Edwards et al., Phys. Rev. Lett. **49** (1982) 259.

[29] W.J. Wisniewski et al., CALT-68-1446 (1987).

W. Toki, SLAC-PUB-4360 (1987).

[30] C. Dionisi et al., Nucl. Phys. **B169** (1980) 1.

[31] T. Armstrong et al., Z. Phys. **C34** (1987) 23.

T. Armstrong et al., Phys. Lett. **146B** (1984) 273.

[32] Ph. Gavillet et al., Z.Phys C. **16** (1982) 119.

D. Aston et al., Nucl. Phys. **B301** (1988) 525.

[33] H. Aihara et al., Phys. Rev. Lett. **57** (1986) 2500.

G. Gidal et al., Phys. Rev. Lett. **59** (1987) 2016.

[34] C.N. Yang, Phys. Rev. **77** (1950) 242.

[35] D. Caldwell, Proceedings of the Workshop on Glueballs, Hybrids and Exotics, BNL, August 1988.

[36] F.M. Renard, Nuovo Cimento **80** (1984) 1.

[37] S. Godfrey and N. Isgur, Phys. Rev. **D32** (1985) 189.

[38] S.U. Chung, BNL 40599 (1987).

[39] F.E. Close, Rep. Prog. Phys. **51** (1988) 833.

D. Caldwell, Mod. Phys. Lett. **A2** (1987) 771.

[40] J. Weinstein, Proceedings of the Workshop on Glueballs, Hybrids and Exotics, BNL, August 1988.

[41] R.K. Carnegie et al., Phys. Lett. **68B** (1977) 287.

[42] Particle data group, Phys. Lett. **204B** (1988) 1.

[43] D.H. Perkins, Introduction to high energy physics, Addison-Wesley publ., (1987).

[44] F. Couchot, LAL 87-40 (1987).

[45] C. Edwards et al., Phys. Rev. Lett. **48** (1982) 458.

[46] J.E. Augustin et al., LAL 85-27 (1985).

[47] R.M. Baltrusaitis et al., Phys. Rev. **D35** (1987) 2077.

[48] T. Armstrong et al., CERN-EP/89-70 (1989).

To be published in Phys. Lett.

[49] G. Costa et al., Nucl. Phys. **B175** (1980) 402.

N.M. Cason et al., Phys. Rev. Lett. **48** (1982) 1316.

[50] W. Beusch et al., Phys. Lett. **25B** (1967) 357.

C. Daum et al., Z. Phys. **C23** (1984) 339.

[51] M. Aihara et al., Phys. Rev. Lett. **57** (1986) 404.

[52] D. Aston et al., Nucl. Phys. **B301** (1988) 525.

[53] S.J. Lindenbaum, Comments Nucl. Part. Phys. **13** (1984) 285.

[54] A. Etkin et al., Phys. Rev. Lett. **40** (1978) 422; **41** (1978) 784.

[55] T.A. Armstrong al., Nucl. Phys. **B196** (1982) 176.

P.S. Booth et al., Nucl. Phys. **B273** (1986) 677; **B273** (1986) 687.

[56] S.J. Lindenbaum, Nuovo Cimento **65A** (1981) 222.

[57] A. Etkin et al., Phys. Lett. **201B** (1988) 568.

[58] H.J. Lipkin, Phys. Lett. **124B** (1983) 509.

S.J. Lindenbaum, Phys. Lett. **131B** (1983) 221.

S.J. Lindenbaum and H.J. Lipkin, Phys. Lett. **149B** (1984) 407.

J. Ellis et al., Phys. Lett. **217B** (1989) 173.

[59] D. Bisello et al., Phys. Lett. **179B** (1986) 294.

[60] T.H. Hansson et al., Phys. Rev. **D26** (1982) 2069.

[61] K.L. Au et al., Phys. Lett. **167B** (1986) 229.

K.L. Au et al., Phys. Rev. **D35** (1987) 1633.

[62] F. Binon et al., Nuovo Cimento, **A78** (1983) 313.

[63] F. Binon et al., Nuovo Cimento, **A80** (1984) 363.

D. Alde et al., Phys. Lett. **201B** (1988) 160.

[64] D. Alde et al., Phys. Lett. **198B** (1987) 286.

[65] S. Gershtein et al., Z. Phys. **C24** (1984) 305.

[66] D. Alde et al., Phys. Lett. **205B** (1988) 397.

[67] CERN Proposals SPSC/82-3/P175 (1982) and SPSC/84-62/P204 (1984).

[68] W. Beusch, Omega Prime, CERN/SPSC/77-70 (1977).

[69] D.E. Plane, The West Area Beams, CERN/SPS/83-22 (1983).

[70] E.H.M. Heijne et al., Nucl. Instr. and Meth. **178** (1980) 331;

B. Hyams et al., Nucl. Instr. and Meth. **205** (1983) 99.

[71] L. Bachman et al., Nucl. Instr. and Meth. **206** (1983) 85.

[72] P. Jarron and M. Goyot, Nucl. Instr. and Meth. **226** (1984) 156.

[73] J.C. Lasalle et al., Nucl. Instr. Meth. **176** (1980) 371.

[74] H. Wind, Nucl. Instr. Meth. **115** (1974) 431.

[75] G. Arfken,Mathematical Methods for Physicists, Academic Press, (1970).

[76] H. Yukawa, Proc. Phys. Math. Soc. Japan **17** (1935) 48.

[77] P.D.B. Collins, Regge Theory and High Energy Physics, Camb. Univ. Press,1977.

[78] A. Sommerfeld, Partial Differential equations in Physics, New York Press,1949.

[79] F.E. Low, Phys. Rev. **D12** (1975) 163.

S. Nussimov, Phys. Rev. Lett. **34** (1975) 1286.

[80] L.L. Foldy and R.F. Peierls, Phys. Rev. **130** (1963) 1585.

[81] R. Carlitz and M.B. Green, Phys. Rev. **D4** (1971) 3439.

S. Humble, Introduction to Particle Production in Hadron Physics, Academic Press,1974.

[82] J.C.M. Armitage et al., Phys. Lett. **82B** (1979) 149.

M.G. Albrow et al., Nucl. Phys. **B108** (1976) 1.

[83] S.N. Ganguli and D.P. Roy, Phys. Rep **67** (1980) 203.

[84] T.A. Armstrong et al., Proceedings of the Int. Europhysics Conference on H.E.P., Bari, July 1985.

[85] T.A. Armstrong et al., Proceedings of the Workshop on Glueballs and Hybrids, BNL August 1988.

T.A. Armstrong et al., CERN-EP/88-124 (1988).

[86] R. Ehrlich et al., Phys. Rev. Lett. **20** (1968) 686.

[87] C. Zemach, Phys. Rev. **B140** (1965) 97.

[88] C. Zemach, Phys. Rev. **133B** (1964) 1201.

[89] J.D. Jackson, Nuovo Cimento, **34** (1964) 6692.

[90] S.M. Flatté, Phys. Lett., **63B** (1976) 224.

[91] D. Antreasyan et al., Phys. Rev., **D33** (1986) 1847.

[93] F. James, FOWL, CERN Computer Centre W505 (1977).

[94] W.T. Eadie et al., Statistical methods in experimental physics, North-Holland, 1971.

[95] F. James and M. Roos, MINUIT Computer Physics Communications **10** (1975) 343.

[96] T.A. Armstrong et al., Phys. Lett. **166B** (1986) 245.

[97] N.P. Chang and C.T. Nelson, Phys. Rev. Lett. **40** (1978) 1617.

[98] T.L. Trueman, Phys. Rev. **D18** (1978) 3423.

[99] G. Eigen, CALT 68-1483 (1987).

[100] H. Albrecht et al., DESY 88-150 (1988).

[101] N.N. Achasov et al., Z. Phys. **C27** (1985) 99.

[102] R.M. Baltrusaitis et al., Phys. Rev. **D33** (1986) 1222.

[103] D. Bisello et al., Phys. Rev. **D39** (1989) 701.

[104] P.E. Condon and P.Cowell, Phys. Rev. **D9** (1974) 2268.

[105] Ph. Gavillet and J.C. Marin, CHAFIT, CERN/D.Ph.II/PROG 75-2,1975.

[106] T. Armstrong et al., Z. Phys. **C43** (1989) 55.

[107] F. Halzen and A.D.Martin,Quarks and Leptons, Wiley (1984).

[108] T. Barnes, Invited Lectures at the School of Physics of Exotic Atoms, Erice, Sicily 31/3/-6/4/84.

[109] A. Chodos et al., Phys. Rev. **D9** (1974) 3471.

[110] J.J. Sakurai, Modern Quantum Mechanics,Benjamin Cummings Publ.Company,1985.

[111] T. Barnes, F.E. Close and S. Monaghan, Nucl.Phys **B198** (1982) 380.

[112] C.E. de Tar, Phys. Rev. **D3** (1971) 128.

[113] A. Breakstone et al., CERN-EP/86-124 (1986).

[114] J. Timmer, Thesis, University of Utrecht, 1978.

[115] R.A. Fisher, Mess. of Math. **41** (1912) 155.